ISSN 1000-9620

Marine Science Bulletin

Volume 7 • Number 1 2005

ISSN 1000-9620
0 1>
9 771000 962001

NATIONAL MARINE DATA AND
INFORMATION SERVICE OF CHINA

LIBRARY
JAN 31 2006
National Oceanic & Atmospheric Administration
U.S. Dept. of Commerce

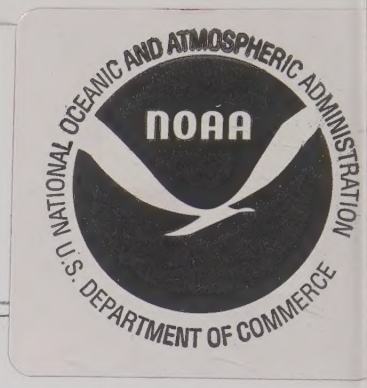

MARINE SCIENCE BULLETIN

Vol.7 No.1 May, 2005

CONTENTS

Analytical Study on Wave Diffraction from a Vertical Circular Cylinder in Front of Orthogonal Vertical Walls ····· *NING Dezhi* (宁德志) *et al.* (1)

Investigation on Touching Sea Bottom by a FPSO in Bohai Oilfield with Shallow Water ····· *LI Xin* (李 欣) *et al.* (10)

Hydrocarbon Potential of Pre-cenozoic Strata in the North Yellow Sea Basin ····· *CAI Feng* (蔡 峰) *et al.* (21)

A New Method of Profiling Remote-Sensing Reflectance of Coastal Waters ····· *Li Tongji* (李铜基) *et al.* (37)

A Preliminary Study on the Calculating Method for the Evolution of Siltation and Erosion of Tidal Flat Based on GIS····· *DU Jinglong* (杜景龙) *et al.* (45)

Temperature Tolerance of Large Yellow Croaker, *Pseudosciaena Crocea* (Richardson) Associated with Summer Season ····· *CHEN Quanzhen* (陈全震) *et al.* (54)

Backward Calculation Based on the Advection and Diffusion of Oil Spills on the Sea Surface ····· *LIU Hao* (刘 浩) *et al.* (63)

Distribution Characteristics of Heavy Metals and Grain Size of Sediments from Hailing Bay, China ····· *QIU Yaowen* (丘耀文) *et al.* (69)

Screening of Lectins in Crab and Shrimp from Fujian Coast of China ····· *Dai Congjie* (戴聪杰) (77)

Research on Measurable Nonlinear Relationship Between Phytoplankton Biomass and Environmental Factors in Bohai Bay ····· *WANG Hongli* (王洪礼) *et al.* (82)

Heavy Metal Biosorption Sites Studies of *Laminaria japonica* ····· *QIAN Aihong* (钱爱红) *et al.* (87)

Research of Influence of Aniline on the Growth of Ocean Algae ····· *QIU Haiyuan* (邱海源) *et al.* (92)

LIBRARY
Pacific Islands Fisheries Science Center
NOAA Fisheries
Honolulu, Hawai'i

Analytical Study on Wave Diffraction from a Vertical Circular Cylinder in Front of Orthogonal Vertical Walls

NING Dezhi (宁德志), TENG Bin (滕 斌), SONG Xiangqun (宋向群)
State Key Laboratory of Coastal and Offshore Engineering, Dalian University of Technology, Dalian 116024, *Liangning, China*

Abstract In this paper, the principle of mirror image is used to transform the problem of wave diffraction from a circular cylinder in front of orthogonal vertical walls into the problem of diffraction of four symmetric incident waves from four symmetrically arranged circular cylinders, and then the eigenfunction expansion of velocity potential and Grafs addition theorem are used to give the analytical solution to the wave diffraction problem. The relation of the total wave force on cylinder to the distance between the cylinder and orthogonal vertical walls and the incidence angle of wave is also studied by numerical computation.

Keywords Wave diffraction, Wave force, Circular cylinder, Orthogonal vertical walls, Principle of mirror image, Grafs addition theorem

Introduction

Wave diffraction from bodies in unbounded waters has been a subject of considerable research interest. There exist a variety of elaborate analytical and numerical techniques for tackling the case-by-case situation. For example, MacCamy and Fuchs[1] developed an analytic solution for wave diffraction from a uniform cylinder, Linton and Evans[2] studied the interaction of waves with arrays of vertical circular cylinders, Yilmaz and Incecik[3] got an analytic solution for wave diffraction from truncated cylinders, Teng[4] solved the diffraction problem of a vertical cylinder with two columns and open outer wall, and Huang[5] researched wave diffraction from compound cylinder.

With the mushrooming of various near-shore and offshore projects in more recent years, the interaction of waves with coastal structures in front of wharf has become much popular. Due to the existence of wharf, the hydrodynamic calculation becomes much more complex and difficult, and the results will be indefinite and inaccurate in a great extent if the wharf is overlooked in calculation. For the problem of wave acting on the body in front of orthogonal and fully reflective vertical walls, the principle of mirror image can be applied such as Nings analytical study on the oscillation of a vertical circular cylinder in front of orthogonal vertical walls[6]. Meanwhile, some scholars founded BEM programs for such problems (such as Van Oortmerssen[7] and Han[8]). Based on the image theory, this paper transforms the wave diffraction from a circular cylinder in front of orthogonal vertical walls into the corresponding problem of four symmetric incident wave diffraction from four symmetrically

Received on April 5, 2004

arranged cylinders in unbounded waters. Then, the eigenfunction expansion is carried out to develop the analytical solution for this problem. The analytic solution can be used to testify the accuracy of other numerical methods. By comparison with the results from a boundary element method, the validity of the present analytical solution is proved. Numerical studies have been conducted to illustrate the effects of the distances between the cylinder and the orghogonal vertical walls, and wave incident direction on the wave loads on the cylinder. Calculated results show that the wave loads on the cylinder in front of orthogonal vertical walls are evidently different from those in unbounded waters, and oscillate with the wave number.

1 Governing Equation and Boundary Conditions

We consider diffraction of wave with incident angle β($0<\beta<\pi/2$) from a uniform cylinder in front of two vertical walls, which intersect normally to each other in horizontal plane (Fig. 1). If we assume that the vertical walls are fully reflective and semi-infinite long, then the problem discussed can be transformed into the problem of the diffraction of four symmetrically incident waves, whose incident angles are $\beta_1=\beta$, $\beta_2=\pi-\beta$, $\beta_3=\pi+\beta$ and $\beta_4=2\pi-\beta$ respectively, from an array of four cylinders arranged at the corners of a rectangular in the whole fluid domain based on the image theory (Fig. 2). The length and the width of the rectangular are twice as long as the distances between the center of the cylinder and the corresponding walls. A general coordinate system ($Oxyz$) is defined with the origin at the center of the array of the four cylinders at the still water level. Similarly, four polar coordinates ($O_j r_j \theta_j z_j$, $j = 1, 2, 3, 4$) are defined with their origins located at the centers of the cylinders respectively. Here, both the z-axis and the z_j-axis are positive upwards.

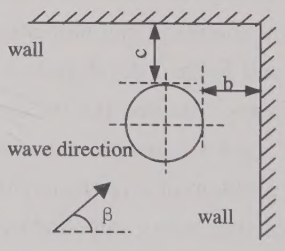

Fig. 1 Definition sketch 1

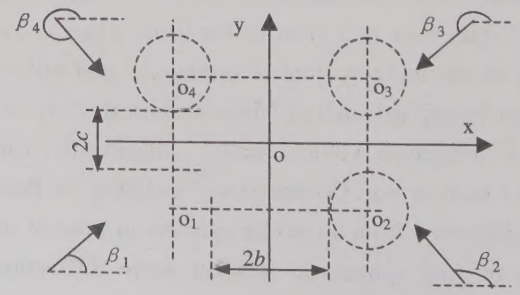

Fig. 2 Definition sketch 2

In the present analysis, the fluid is assumed to be inviscid, incompressible and irrotational. For harmonic incident waves, the fluid motion is simple harmonic in time with angular frequency ω. Thus, we can single out the time factor and write the velocity potential $\Phi(x, y, z, t)$ as follows:

$$\Phi(x, y, z, t) = \mathrm{Re}[f(z)\phi(x, y)e^{-i\omega t}] \tag{1}$$

where ϕ is the complex potential. The vertical distribution function:

$$f(z) = -\frac{igA}{\omega}\frac{\cosh k(z+d)}{\cosh kd} \tag{2}$$

in which A is the amplitude of the incident waves, d the water depth, k the wave number which satisfies the dispersion equation

$$\omega^2 = gk\tanh kd \tag{3}$$

The horizontal complex velocity potential (x, y) satisfies the Helmholtz equation:

$$\frac{\partial^2\phi(x, y)}{\partial x^2} + \frac{\partial^2\phi(x, y)}{\partial y^2} + k^2\phi(x, y) = 0 \tag{4}$$

On the surface of each cylinder, the velocity potential satisfies the body surface condition

$$\frac{\partial\phi}{\partial r_j}\Big|_{r_j=a} = 0 \qquad (j = 1, 2, 3, 4) \tag{5}$$

where a is the radius of each cylinder, and the Sommerfeld condition

$$\sqrt{kr}\left(\frac{\partial\phi}{\partial r} - \mathrm{i}k\phi\right) = 0, \quad (j=1, 2, 3, 4)\ \mathrm{r}\to\infty \tag{6}$$

at infinity.

2 Mathematical analyses

In the whole fluid domain as Fig. 2, the complex velocity potential ϕ can be divided into four incident waves with different incident angles of β_1, β_2, β_3 and β_4 and four diffraction waves from the 4 cylinders as

$$\phi = \sum_{l=1}^{4}\psi_I^l + \sum_{j=1}^{4}\psi_D^j \tag{7}$$

In the jth polar coordinate system (with the origin at the center of the cylinder j ($j = 1, 2, 3, 4$)), the lth incident potential ψ_I^l can be written as

$$\psi_I^l = I_j^l\,\mathrm{e}^{\mathrm{i}kr_j\cos(\theta_j-\beta_l)} \tag{8}$$

where $I_j^l = \mathrm{e}^{\mathrm{i}k(x_j\cos\beta_l + y_j\sin\beta_l)}$ represents the phase difference due to the position of the cylinder, (x_j, y_j) is the coordinates of the center of the jth cylinder in the global coordinate system.

Applying the formula of Bessel functions, the velocity potential (Eq. 8) can be written into a

Fourier series

$$\psi_I^l = I_j^l \sum_{n=-\infty}^{\infty} \mathrm{J}_n(kr_j)\,\mathrm{e}^{\mathrm{i}n(\pi/2-\theta_j+\beta_l)} \tag{9}$$

where $J_n(x)$ is the first kind of Bessel function of order n.

The diffraction potential ψ_D^j from the jth cylinder is represented by

$$\psi_D^j = \sum_{n=-\infty}^{\infty} A_n^j C_n \mathrm{H}_n(kr_j)\,\mathrm{e}^{\mathrm{i}n\theta_j} \tag{10}$$

in the coordinate system with the origin at the center of the cylinder itself, where A_n^j is the unknown to be determined, $C_n = \mathrm{J}_n'(ka)/\mathrm{H}_n'(ka)$, and $H_n(x)$ is the first kind Hankel function of order n.

Applying the Grafs addition theorem[9], we have the following expression,

$$\mathrm{H}_n(kr_j)\,\mathrm{e}^{\mathrm{i}n\theta_j} = \sum_{m=-\infty}^{\infty} \mathrm{H}_{n+m}(kR_{jk})\,\mathrm{J}_m(kr_k)\,\mathrm{e}^{\mathrm{i}(m\alpha_{kj}+n\alpha_{jk}))}, \quad (r_k < R_{jk}) \tag{11}$$

then we can write the diffraction potential from the jth cylinder in the kth coordinate system as

$$\psi_D^j = \sum_{n=-\infty}^{\infty} A_n^j C_n \sum_{m=-\infty}^{\infty} \mathrm{J}_m(kr_k)\,\mathrm{H}_{n+m}(kR_{jk})\,\mathrm{e}^{\mathrm{i}m(\pi-\theta_k)}\,\mathrm{e}^{\mathrm{i}(n+m)\alpha_{jk}} \tag{12}$$

where R_{jk} is the distance between the centers of the jth and kth cylinders, and α_{kj} the directional angle of the jth cylinder relative to the kth cylinder.

By substituting Eqs. (9), (10) and (12) into Eq. (7), we can represent the total complex potential in the kth coordinate system as

$$\begin{aligned}\phi(r_k,\theta_k) = &\sum_{n=-\infty}^{\infty}\Big[\sum_{l=1}^{4} I_k^l \mathrm{J}_n(kr_k)e^{\mathrm{i}n(\pi/2-\beta_l)} + A_n^k C_n \mathrm{H}_n(kr_k)\Big]\mathrm{e}^{\mathrm{i}n\theta_k} \\ &+ \sum_{\substack{j=1\\ j\neq k}}^{4} \sum_{m=-\infty}^{\infty}\Big(\sum_{n=-\infty}^{\infty} A_n^j C_n \mathrm{H}_{n-m}(kR_{jk})e^{\mathrm{i}(n-m)\alpha_{jk}}\Big)\mathrm{J}_m(kr_k)\,\mathrm{e}^{\mathrm{i}m\theta_k}\end{aligned} \tag{13}$$

in the domain close to the kth cylinder.

By applying the body surface condition (5), the equation can be obtained as follows:

$$\begin{aligned}0 = \sum_{n=-\infty}^{\infty} e^{\mathrm{i}n\theta_k}\Big[\sum_{l=1}^{4} I_k^l \mathrm{J}_n'(ka)e^{\mathrm{i}n(\pi/2-\beta_l)} + A_n^k C_n \mathrm{H}_n'(ka) + \\ \sum_{\substack{j=1\\ j\neq k}}^{4} \sum_{m=-\infty}^{\infty} A_m^j C_m \mathrm{J}_n'(ka)\,\mathrm{H}_{m-n}(kR_{jk})\,\mathrm{e}^{\mathrm{i}(m-n)\alpha_{jk}}\Big]\end{aligned} \tag{14}$$

Applying the normalizing condition of $\mathrm{e}^{\mathrm{i}n\theta_k}$, we can obtain

$$A_n^k + \sum_{\substack{j=1\\ j\neq k}}^{4} \sum_{m=-\infty}^{\infty} A_m^j C_m \mathrm{H}_{m-n}(kR_{jk})\,\mathrm{e}^{\mathrm{i}(m-n)\alpha_{jk}} = -\sum_{l=1}^{4} I_k^l\,\mathrm{e}^{\mathrm{i}n(\pi/2-\beta_l)} \quad (k=1,2,3,4) \tag{15}$$

If we take $2M+1$ (M, M-1, ···, 0, 1, ···, M) terms to approximate the diffraction potentials, there

are $4\times(2M+1)$ linear equations for $4\times(2M+1)$ unknowns A_m^k. Then the unknowns A_m^k can be determined.

Multiplying the above equation with $J_n(ka)$ and substituting it into Eq. (13), we can write the total velocity potential simply as

$$\phi(r_k,\theta_k)=\sum_{n=-\infty}^{\infty}A_n^k(C_n\,H_n(kr_k)-J_n(kr_k))\,e^{in\theta_k} \tag{16}$$

in the domain close to the kth cylinder. This equation is the velocity potential in front of orthogonal vertical walls.

3 Wave Force

Wave pressure can be obtained by Bernoulli equation

$$P=i\omega\rho\,\phi(r,\theta)\,f(z) \tag{17}$$

where ρ is the density of fluid. The wave force on the kth cylinder can be obtained by integration of the wave pressure over the cylinder surface

$$F=\iint_{S_B}P\,n\,ds=-i\omega\rho a\int_{-d}^{0}f(z)dz\int_{0}^{2\pi}\phi(a,\theta_k)\begin{Bmatrix}\cos\theta_k\\ \sin\theta_k\end{Bmatrix}d\theta_k \tag{18}$$

where n is the unit normal vector of the cylinder surface directing out of the fluid. Substituting Eq. (16) into Eq. (18) and applying the normalization relation of cosine and sine functions, we can obtain the amplitudes of wave forces in the x and y directions as

$$F_x=i\frac{2\rho gA}{k^2H_1'(ka)}\tanh kd\,(A_1^k-A_{-1}^k) \tag{19}$$

$$F_y=-\frac{2\rho gA}{k^2H_1'(ka)}\tanh kd\,(A_1^k+A_{-1}^k) \tag{20}$$

where the Wronskian relation for Bessel functions[9]

$$J_n'(ka)H_n(ka)-H_n'(ka)J_n(ka)=-\frac{2i}{\pi ka} \tag{21}$$

has been used.

4 Numerical Results and Verification

As an example, we consider a cylinder of radius a in a water depth $d/a=1$. The cylinder oscillates harmonically with the unit amplitude. The distances between the cylinder and the horizontal and vertical walls are c and $b$respectively (Fig.1).

4.1 Verification

Figs. 3 and 4 are the comparisons of the wave force components in the x and y directions obtained from the present analytic solution and a boundary element method from Han[8] when waves

income with an angle of $\beta = \pi/6$ and the distances between the cylinder and the walls are $b/a = 0.5$ and $c/a = 0.5$. From the comparison, we can see that the two methods agree very well, and it testifies the correctness of the present theory.

4.2 Numerical results and analysis

Figs. 5 and 6 are the distributions of non-dimensional wave force components in the x and the y directions versus wave number at $\beta = \pi/6$, $c/a = 0.2$ and $b/a = 0.2$, 1.0, 5.0 respectively. The wave force components on cylinders in unbounded waters are also plotted for comparison (UW denotes the case in the following figures). From the figures, we can see that the x-directional components of the wave forces on the cylinders with distances $b/a = 0.2$, 0.5 and 1.0 to the vertical wall are as large as 6.36, 5.59 and 4.69 times that on the cylinder in unbounded waters and the wave force increases considerately when the cylinder is close to the orthogonal vertical walls. Special attention must be paid to the situation. In front of the orthogonal vertical walls the distributions of the wave force components oscillate with the increase of the wave frequency. The oscillate frequency increases with the increase of the distance between the cylinder and the wall. When the distance between the cylinder and the horizontal wall is fixed, the wave force component in the y-direction oscillates more seriously with the increase of the distance between the cylinder and the vertical wall. The reason for the oscillation is that the incident and diffraction waves act on the cylinder simultaneously, and minor change in the incident frequency of incident waves will lead to quick alteration of the phase difference between those two waves when the cylinder is farther from the vertical wall.

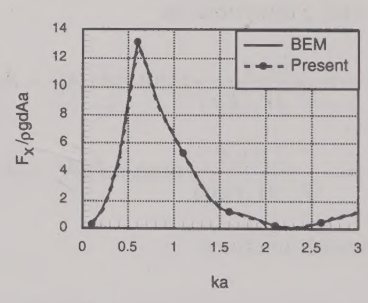

Fig. 3 Distribution of wave force in the x direction versus wave number at $\beta = \pi/6$, $c/a = b/a = 0.5$

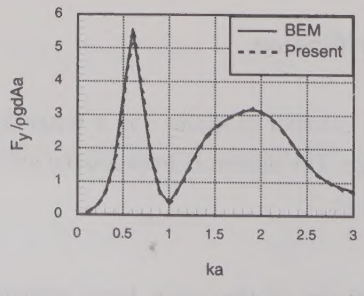

Fig. 4 Distribution of wave force in the y direction versus wave number at $\beta = \pi/6$, $c/a = b/a = 0.5$

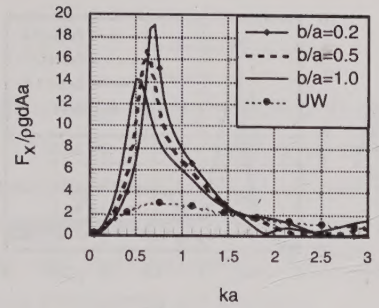

Fig. 5 Distribution of wave force in the *x* direction versus wave number at $\beta = \pi/6$, $c/a = 0.2$

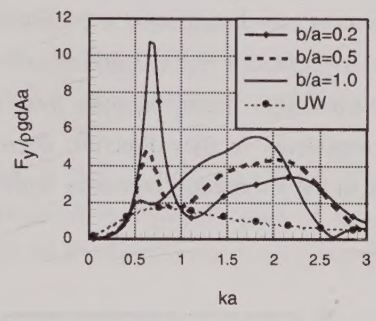

Fig. 6 Distribution of wave force in the *y* direction versus wave number at $\beta = \pi/6$, $c/a = 0.2$

Figs. 7 and 8 are the similar distributions of non-dimensional wave force components when the wave incident angle is $\beta = \pi/4$. It can be seen from the figures that the wave force components in the x and the y directions are the same when $b/a = c/a$, which again validates the present model. With the increase of b/a the wave force components in the x and the y directions decrease. The decrease rate of the wave force component in the y direction is larger than that in the x direction.

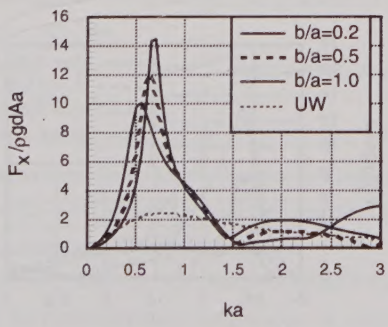

Fig. 7 Distribution of wave force in the *x* direction versus wave number at $\beta = \pi/4$, $c/a = 0.2$

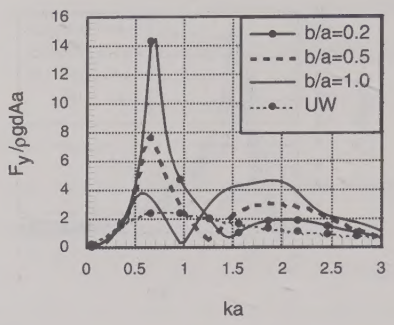

Fig. 8 Distribution of wave force in the *y* direction versus wave number at $\beta = \pi/4$, c/a=0.2

Figs. 9 and 10 are the distributions of non-dimensional wave force components with wave frequency at different wave incident angles $\beta = \pi/9$, $2\pi/9$, $\pi/3$ and $4\pi/9$ when the distances between the cylinder and the walls are $b/a = c/a = 0.5$. It can be seen from the figures that the peaks of the distribution of the wave force components in the *x*-direction decreases with the increase of wave incident angle, and the component in the *y* direction increases with the increase of the incident wave angle.

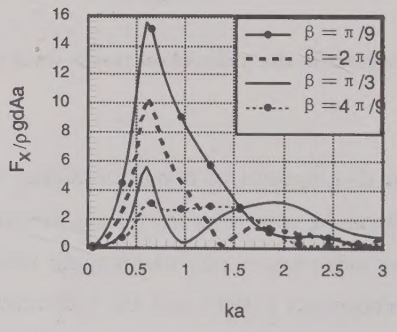

Fig. 9 Distribution of wave force in the *y* direction versus wave number at $b/a = 0.5$, $c/a = 0.5$

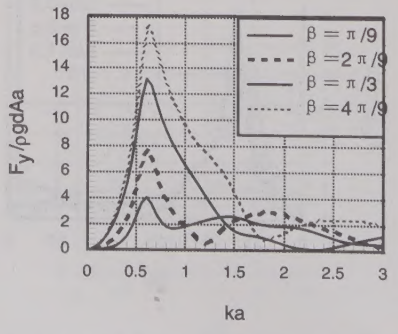

Fig. 10 Distribution of wave force in the *y* direction versus wave number at $b/a = 0.5$, $c/a = 0.5$

5 Conclusion

Based on the principal of mirror image and eigenfunction expansion, a convenient analytic solution is developed for wave diffraction from a cylinder in front of orthogonal vertical walls. The present method can be used to testify the accuracy of other numerical methods and provide some foundation for engineering designs. Numerical computations are carried out for different cases to examine the effect of the distances between the cylinder and walls and wave incident angles on wave loads on the cylinder. From the examination the following conclusions can be drawn.

(1) Wave force on a cylinder close to orthogonal vertical walls is evidently different from the force on the corresponding cylinder in unbounded waters. And the distribution of wave force on a cylinder close to walls oscillates with the increase of wave number. The farther the cylinder is away from the walls, the faster the distribution of wave force oscillates.

(2) The distance between the cylinder and the walls is a key factor for wave force on a cylinder in front of walls. The peak of the wave force decreases with the increase of the distances between the cylinder and the walls.

(3) The wave incident angle is also an important factor for the x and y components of wave forces. With the increase of wave incident angle, the peak of the distribution of the x component of wave force decreases, and the peak of the distribution of the y-component of wave force increases.

Acknowledgements

The present work is financially supported by the National Natural Science Foundation of China (Grant No.50025924).

References

[1] MacCamy R C and Fuchs R A. *Wave forces on piles: A diffraction theory.* Tech Mem, 69, US Army Coastal Engineering Research Center, 1954.

[2] Linton C M, Evans D V. The interaction of waves with arrays of vertical circular cylinders. *Fliud Mech.*, 1990, 215: 549-569.

[3] Yilmaz O, Incecik A. Analytical solution of the diffraction problem of a group of truncated vertical cylinders. *Ocean Engineering*, 1998, 25(6): 385-394.

[4] Teng Bin, Han Ling, Li Yucheng. Wave diffraction from a vertical cylinder with two columns and porous outer wall. *Ocean Engineering*, 2001, 19(1): 32-37.

[5] Huang Hua, Zhang Diming, Sun Mingguang. A practical method of the evaluation of the finite amplitude wave forces on vertical compound circular cylinder. *Journal of Zhongshan University*, 1996, 05: 33-38.

[6] Ning Dezhi, Teng Bin. Study on the oscillation of a uniform cylinder in front of two vertical walls intersecting normally. *Chinese Engineering Science*, 2003, 5(5): 84-91.

[7] Van Oortmerssen G. *The motions of a moored ship in waves.* NSMB Pub-510, 1979.

[8] Han L, Teng B, and Dong G H. Hydrodynamic coefficients of ships in front of a vertical wall. *Proc. of Second Int. Workshop on Ship Hydrodynamics*, 2001, 24-29.

[9] Abramovitz M, Stegun I A. Handbook of mathematical functions. Government Printing Office, Washington, 1964.

where A stands for wave amplitude, g the acceleration of gravity, h the water depth; k the wave number, β denotes wave heading which is defined as the angle between the direction of wave propagations and the positive x-axis.

Then added-mass matrix μ_{ij} and damping matrix λ_{ij} can be determined by the following equation[3, 4]:

$$\mu_{ij} + i\lambda_{ij}/\omega = -\rho \int_{S_B} \phi_{Rj} n_i ds \tag{10}$$

And the wave loads in frequency domain f_{wi} for $i = 1,2,\cdots,6$ is evaluated by

$$f_{wi} = -i\rho\omega \int_{S_B} (\phi_I + \phi_d) n_i ds \tag{11}$$

(f_{w1}, f_{w2}, f_{w3}) stand for wave forces and (f_{w4}, f_{w5}, f_{w6}) are the wave moments.

1.2 Simulation method in time domain

FPSOs' motion[4] is determined by the following motion equation[5, 6]:

$$\sum_{j=1}^{6} \left[(M_{ij} + \mu_{ij}) \ddot{x}_j(t) + \int_0^t K_{ij}(t-\tau) \dot{x}_j(\tau) d\tau + C_{ij} x_j(t) \right] = F_{wi}(t) \quad i = 1,2,\cdots,6 \tag{12}$$

where $x_j(t)$ is the wave frequency motion, C_{ij} the restoring matrix, M_{ij} the inertia matrix, $K_{ij}(t)$ is the retardation function, which means the influence of the memory effect in the free surface can be obtained by

$$K_{ij}(t) = \frac{2}{\pi} \int_0^\infty \lambda_{ij}(\omega) \cos(\omega t) d\omega \tag{13}$$

$F_{wi}(t)$ is the first-order wave force. According to the Cummins impulse technique[7], $F_{wi}(t)$ can be derived from $f_{wi}(\omega)$ in frequency domain as follows

$$F_{wi}(t) = \int_{-\infty} h_i(t-\tau) \eta(\tau) d\tau \tag{14}$$

Here $\eta(\tau)$ is the wave elevation at time τ which can be considered as some of impulse function $\delta(\tau)$. If $\eta(\tau)$ equals $\delta(\tau)$, $F_{wi}(t)$ equals $h_i(t)$ which represents the impulse response. $h_i(t)$ and $f_{wi}(\omega)$ are a couple of Fourier transformations as follows,

$$\begin{cases} f_{wi}(\omega) = \int_{-\infty}^{\infty} h_i(t) e^{-i\omega t} dt \\ h_i(t) = \dfrac{1}{2\pi} \int_{-\infty}^{\infty} f_{wi}(\omega) e^{-i\omega t} dt \end{cases} \tag{15}$$

By solving Eq. (12), the time series of the wave frequency motion will be acquired.

2 Research subject

Based on the 3-D linear potential flow theory and the time-domain numerical simulation method, a 160 kDWT FPSO with Yoke single point mooring system in Bohai oilfield is investigated in this paper. Numerical calculations in time domain and the model test are carried out for the SPM FPSO system in survival storm once in 100 years with various drafts, 14.5 m, 14.2 m, 14.0 m, 13.7 m and 12.34 m. The

main particulars of the FPSO vessel are listed in Table 1 and the SPM system is shown in Fig.1, environmental condition see Table 2.

Tab. 1 Main particulars of the 160 kDWT FPSO vessel

Designation	Symbol	Unit	Full load
Length over all	L_{OA}	m	287.4
Length between perpendiculars	L_{PP}	m	282.0
Breadth	B	m	51.0
Depth	D	m	20.6
Mean draft	T	m	14.5
Displacement	Δ	t	201287.0
Centre of gravity above base	KG	m	13.002
Centre of gravity forward from midship	LCG	m	-4.32
Longitudinal radius of gyration	K_{XX}	m	16.53
Longitudinal radius of gyration	K_{YY}	m	70.5

Tab.2 Environmental conditions in 100-years

	Water depth / m	significant wave height / m	Wave direction / °	Wind speed / m • s^{-1}	Wind direction / °	Current speed / m • s^{-1}	Current direction / °
1	16.7	5.0	180	33.9	180	1.73	135
2	16.7	5.0	180	33.9	180	1.73	90

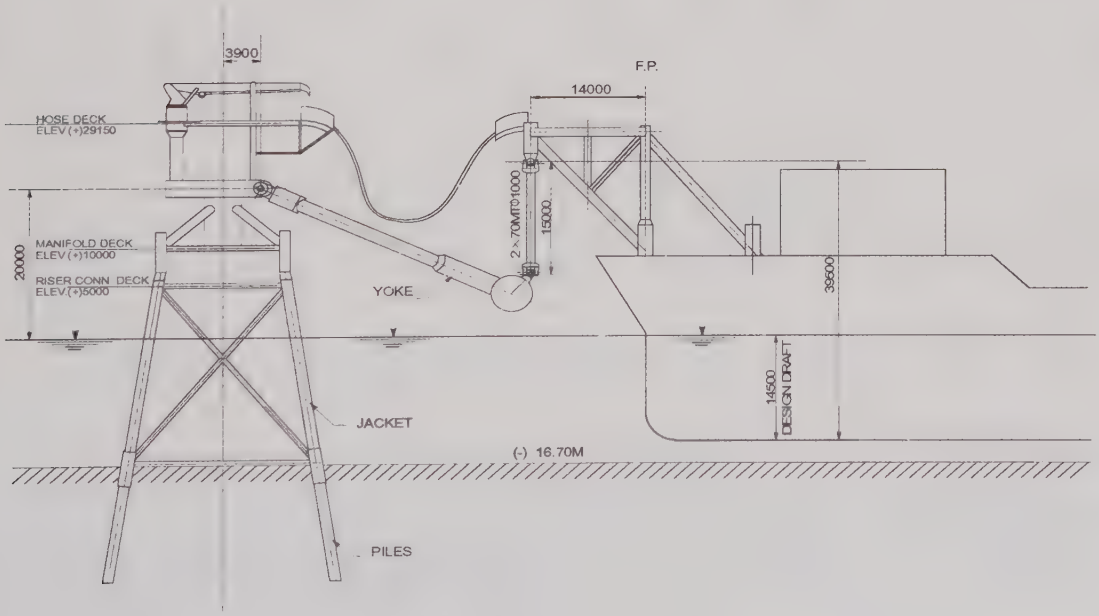

Fig.1 The mooring system

3 Calculation and experiment

3.1 Mesh

The wetted surface of FPSO is meshed as shown in Fig.2. Owing to the symmetry, only the portside is necessary to be meshed. The whole meshing comprises 432×2 panels.

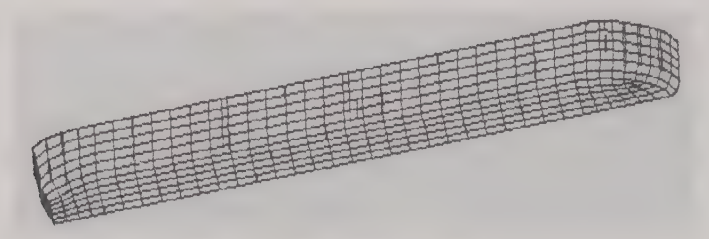

Fig.2 Meshing of the FPSO

3.2 Simulation of the mooring system

The yoke single point mooring system is simulated by one chain so that the static restoring force curve agrees well with the curve measured in the model test. The result is shown in Figure 3.

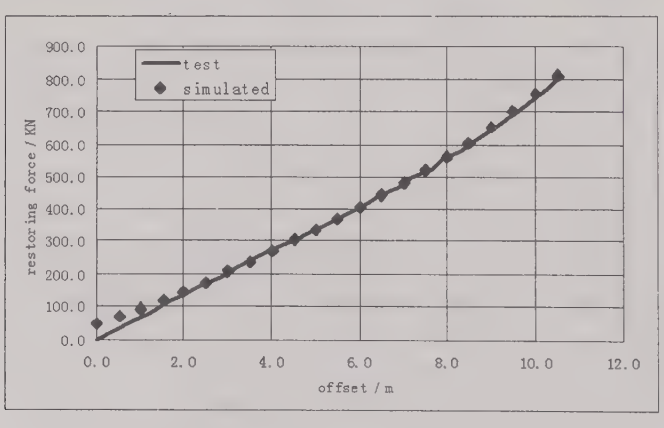

Fig.3 Static restoring force curve

3.3 Time-domain simulation of the motion

The time trace of the clearance between hull and sea bed can be acquired in five different drafts. The clearance between hull and seabed is calculated at various points, which are on the baseline vertically port side and starboard side and transversely the two ends of the parallel middle body longitudinally respectively. In this paper the reference points located at 14 m from bow and 39.5 m from bottom are predicted. The sketch map of the reference point is showed in Fig.4. The calculation results are compared with the experimental data.

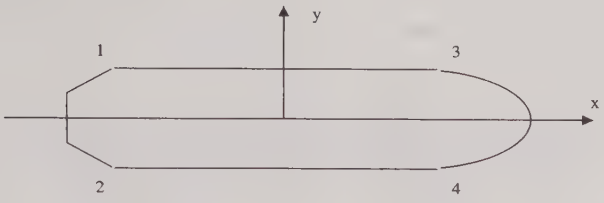

Fig.4 The gauging points on the parallel middle body

3.4 Model test

Model test for motions and clearance of the FPSO is carried out in the wave basin of the State Key Laboratory of Ocean Engineering, Shanghai Jiaotong University. The linear scale ratio between the prototype and model is chosen as 64. Four draft conditions of FPSO, 14.5 m, 14.2 m, 13.7 m and 12.34 m, the motion and clearance are studied. Four displacement sensors are set on the four points (see Fig. 4). And we can observe the entire course through the video camera which is set under water.

3.5 Simulation of the environmental conditions

3.5.1 Water depth

The practical water depth is 16.7 m, and the simulative water depth is 0.261 m in model test. Simulation of water depth can be carried out by adjusting the position of the large area false bottom up or down.

3.5.2 Current

In the environmental condition occurring once in 100 years the surface current speed is 1.73 m/s, the middle current speed is 1.63 m/s and the bottom current speed is1.29 m/s. Uniform current can be generated by high pressure water jet type current generating system. For the surface current speed, the simulated result is 0.216 m/s.

3.5.3 Wind

Stable wind and wind spectrum can be generated by the wind generating system with axial fans. This system is equipped in the low part of front bridge of towing carriage. The steady wind speed is 33.9 m/s in the environmental condition occurring once in 100 years, and that in the model test is 4.24 m/s.

3.5.4 Wave

The PM spectrum is selected for the wave. The significant wave height is 5.0 m and the peak period is 10.3 s. The PM spectrum is given as follows:

$$S(f) = \alpha H_s^2 T_p^{-4} f^{-5} \exp\left[-1.25\left(T_p f\right)^{-4}\right] \gamma^{\exp\left[-\left(T_p f-1\right)^2/2\sigma^2\right]} \tag{16}$$

where, $S(f)$ — Spectral density ($m^2 \cdot s$); f — Wave frequency (Hz); g — Acceleration of gravity (m^2/s); Hs — Significant wave height (m); fp — Spectral peak frequency (Hz) = $1 / T_P$; T_P — Spectral peak period (s); $\gamma = 1$ Shape parameter;

$$\sigma \begin{cases} = 0.09 & f > f_p \\ = 0.07 & f < f_p \end{cases}$$

3 Calculation and experiment

3.1 Mesh

The wetted surface of FPSO is meshed as shown in Fig.2. Owing to the symmetry, only the portside is necessary to be meshed. The whole meshing comprises 432×2 panels.

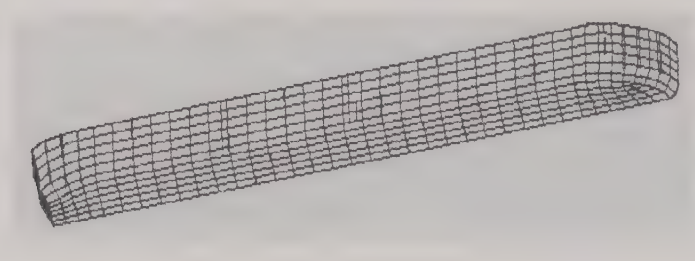

Fig.2 Meshing of the FPSO

3.2 Simulation of the mooring system

The yoke single point mooring system is simulated by one chain so that the static restoring force curve agrees well with the curve measured in the model test. The result is shown in Figure 3.

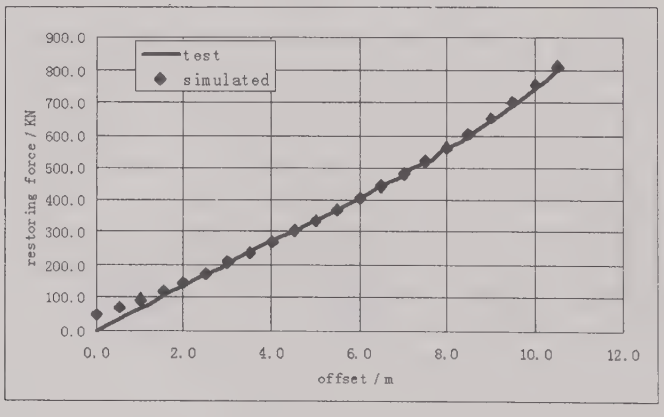

Fig.3 Static restoring force curve

3.3 Time-domain simulation of the motion

The time trace of the clearance between hull and sea bed can be acquired in five different drafts. The clearance between hull and seabed is calculated at various points, which are on the baseline vertically port side and starboard side and transversely the two ends of the parallel middle body longitudinally respectively. In this paper the reference points located at 14 m from bow and 39.5 m from bottom are predicted. The sketch map of the reference point is showed in Fig.4. The calculation results are compared with the experimental data.

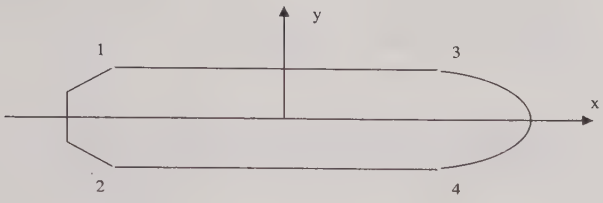

Fig.4 The gauging points on the parallel middle body

3.4 Model test

Model test for motions and clearance of the FPSO is carried out in the wave basin of the State Key Laboratory of Ocean Engineering, Shanghai Jiaotong University. The linear scale ratio between the prototype and model is chosen as 64. Four draft conditions of FPSO, 14.5 m, 14.2 m, 13.7 m and 12.34 m, the motion and clearance are studied. Four displacement sensors are set on the four points (see Fig. 4). And we can observe the entire course through the video camera which is set under water.

3.5 Simulation of the environmental conditions

3.5.1 Water depth

The practical water depth is 16.7 m, and the simulative water depth is 0.261 m in model test. Simulation of water depth can be carried out by adjusting the position of the large area false bottom up or down.

3.5.2 Current

In the environmental condition occurring once in 100 years the surface current speed is 1.73 m/s, the middle current speed is 1.63 m/s and the bottom current speed is1.29 m/s. Uniform current can be generated by high pressure water jet type current generating system. For the surface current speed, the simulated result is 0.216 m/s.

3.5.3 Wind

Stable wind and wind spectrum can be generated by the wind generating system with axial fans. This system is equipped in the low part of front bridge of towing carriage. The steady wind speed is 33.9 m/s in the environmental condition occurring once in 100 years, and that in the model test is 4.24 m/s.

3.5.4 Wave

The PM spectrum is selected for the wave. The significant wave height is 5.0 m and the peak period is 10.3 s. The PM spectrum is given as follows:

$$S(f) = \alpha H_s^2 T_p^{-4} f^{-5} \exp\left[-1.25\left(T_p f\right)^{-4}\right] \gamma^{\exp\left[-\left(T_p f-1\right)^2/2\sigma^2\right]} \tag{16}$$

where, $S(f)$ — Spectral density ($m^2 \cdot s$); f — Wave frequency (Hz); g — Acceleration of gravity (m^2/s); Hs — Significant wave height (m); fp — Spectral peak frequency (Hz) = $1 / T_P$; T_P — Spectral peak period (s); $\gamma = 1$ Shape parameter;

$$\sigma \begin{cases} = 0.09 & f > f_p \\ = 0.07 & f < f_p \end{cases}$$

The wave spectrum in the present test is the same as the PM spectrum in the calculation. Comparison between the target wave spectrum and measured wave spectrum is shown in Fig.5.

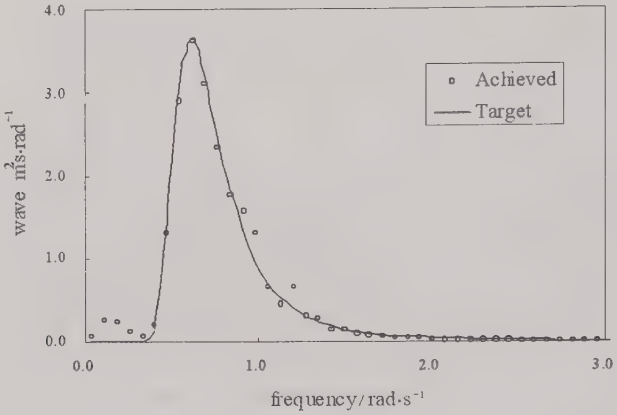

Fig.5 Target and measured wave spectrums

4 Results of calculation and experiment

4.1 The calculated and experimental time series of the result of touching sea bottom

The calculated time series of touching sea bottom of FPSO with 14.5 m draft are compared with the experimental data. Figs. 6 and 7 are the results of the left bow (point 3 in Fig.4) and right stern (point 2 in Fig.4) when the FPSO is exposed in 180 degree wave and 135 degree current once in 100 years.

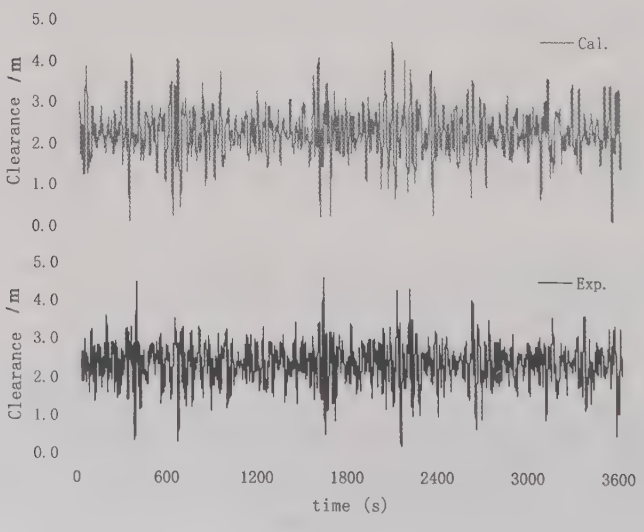

Fig.6 Time series of the clearance of point 3 in 180 degree wave with 135 degree current

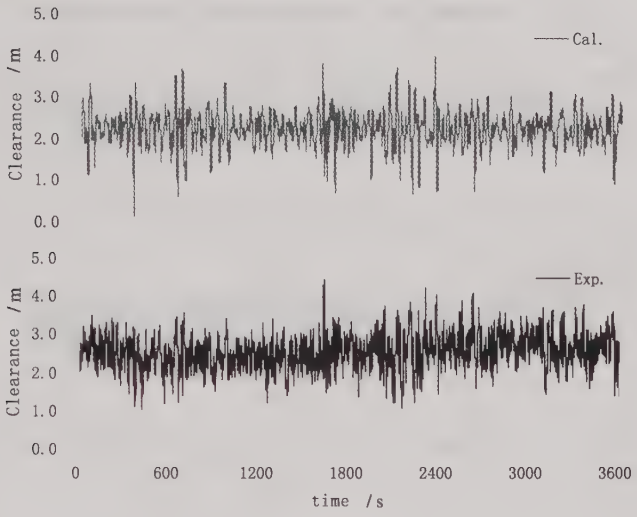

Fig.7 Time series of the clearance of point 2 in 180 degree wave with 135 degree current

The results agree well and under this condition, the FPSO does not touch the sea bottom. Figs. 8 and 9 are the results of the right bow (point 4 in Fig.4) and left stern (point 1 in Fig.4) in 90 degree current and 100 degree wave. As for the 90 degree current condition, there is some difference between the calculation and experiment. But the trend is the same and the FPSO does not touch the sea bottom either at the two points.

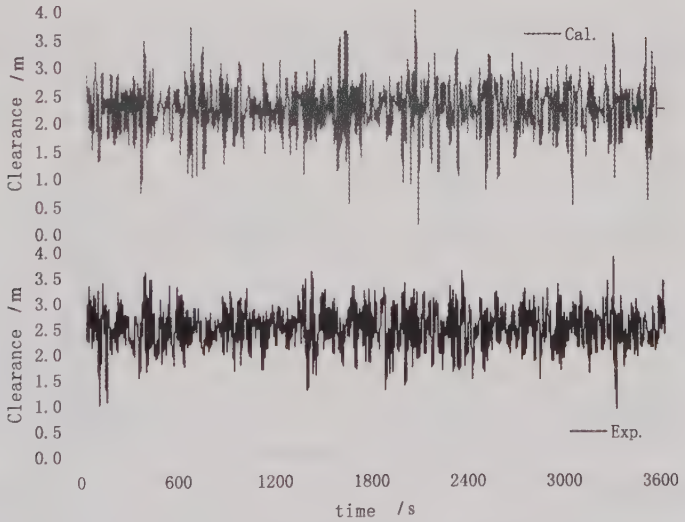

Fig.8 Time series of the clearance of point 4 in 180 degree wave with 90 degree current

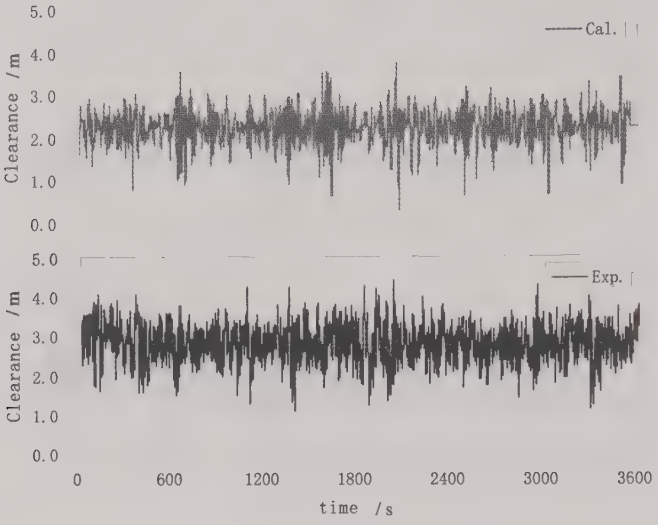

Fig. 9 Time series of the clearance of point 1 in 180 degree wave with 90 degree current

4.2 Comparisons of the statistic values

The statistic result of touching sea bottom in 135 degree current condition is shown in Table 3 and there is good agreement between the calculated result and the experimental value. The result in 90 degree current condition is in Table 4 and the FPSO touching the sea bottom at the left bow point 3 and right stern point 2 in the calculation result. There are some errors because it is not accurate to use the single mooring leg to simulate the yoke mooring system.

Tab.3 The clearance between the FPSO and seabed in 180 degree wave with 135 degree current

Position		Max.	Min.	Mean	Std.
Right bow	Cal. / m	3.989	0.460	2.201	0.472
	Exp. / m	3.798	0.499	2.134	0.398
Left bow	Cal. / m	4.408	0.063	2.200	0.558
	Exp. / m	4.550	0.142	2.298	0.496
Right sterm	Cal. / m	4.258	0.155	2.203	0.512
	Exp. / m	5.189	0.179	2.335	0.492
Right sterm	Cal. / m	3.952	0.107	2.202	0.428
	Exp. / m	4.410	0.901	2.499	0.439

4.3 Result of various drafts

The comparison between the numerical statistic minimum and test values for the clearance between hull and seabed with the draft 14.5 m, 14.2 m, 14.0 m, 13.7 m and 12.34 m is listed in Table 5. The calculated results show that there are two negative minimum values in the 14.5 m draft and one negative

minimum value in the 14.2 m draft. It means that the hull has touched sea bottom in the two drafts. In the model test the minimum values in 14.5 m and 14.2 m drafts are so small that it can be considered that the FPSO almost touches the seabed. In other drafts, there are no phenomena of touching sea bottom in both calculation and experiment. The results of the calculation and experiment indicate that the FPSO under the fully loaded condition will touch sea bottom.

Tab.4 The clearance between the FPSO and seabed in 180 degree wave with 90 degree current

Position		Max.	Min.	Mean	Std.
Right bow	Cal. / m	3.970	0.116	2.203	0.427
	Exp. / m	3.259	0.184	1.781	0.373
Left bow	Cal. / m	4.015	-0.755	2.203	0.556
	Exp. / m	4.310	0.099	2.339	0.512
Right sterm	Cal. / m	4.386	-0.421	2.203	0.556
	Exp. / m	4.518	0.024	1.699	0.546
Right sterm	Cal. / m	3.712	0.262	2.203	0.390
	Exp. / m	3.819	0.542	2.258	0.427

Tab.5 The minimum values of clearance in various drafts (90 degree current) / m

	Experiment				Calculation				
Draft	12.34	13.70	14.20	14.50	12.34	13.70	14.00	14.20	14.50
Right bow	1.84	1.30	0.64	0.18	2.29	0.89	0.71	0.33	0.12
Left bow	1.06	0.43	0.31	0.10	1.53	0.14	0.13	-0.27	-0.76
Right stern	1.72	1.01	0.99	0.02	0.08	0.49	0.45	0.08	-0.42
Left stern	2.20	0.97	0.83	0.54	2.49	0.99	0.82	0.43	0.26

5 Conclusions

(1) For heave and pitch motions of the FPSO, the time series and statistical results of calculations agree well with those of the test results. It means that time domain simulations can be used to predict the touch of sea bottom by large FPSO in shallow water.

(2)For the BZ25-1 FPSO, the hull will touch sea bottom when the FPSO is fully loaded (draft is 14.5 m) for the survival storm condition once in 100 years with 16.7m water depth.

(3) The FPSO studied in this paper should be less loaded than that under the fully loaded condition when the survival storm is coming.

Acknowledgements

This work was supported by the Development Program of China (863 Program, No. 2002AA602011). This support is gratefully acknowledged.

References

[1] Mao Yongjun and Mao Jiugang. Fast Growing FPSO Industry and the Countermeasures. *China Offshore Platform,* 1998, 13(4): 4-8.

[2] Yang Jianmin, Xiao Longfei and Pen Tao. Investigation of motions of an oil tanker model in shallow water with Irregular Waves. *Ocean Engineering*, 2000, 18(3): 25-29. (in Chinese)

[3] Blandeau F, Francois M, Malenica S, et al. Linear and Non-Linear Wave Loads on FPSOs.*Proceedings of the Ninth (1999) International Offshore and Polar Engineering Conference Brest*, France, 1999, May 30-June 4.

[4] Liu Yingzhong and Miao Guoping. *Theory of motion of ships on waves.* Shanghai Jiao Tong University Press, Shanghai, 1987. (in Chinese)

[5] Wang xianfu, *Computational Fluid Dynamics of Ship.* Shanghai Jiao Tong University Press, Shanghai, 1992. (in Chinese)。

[6] Li Xin, Yang Jianmin and Xiao Longfei. Motion Analysis on a Large FPSO in Shallow Water.*Proceedings of the Thirteenth (2003) International Offshore and Polar Engineering Conference*, 2003, 235-239.

[7] Cummins W E. The impulse response function and ship motions. Schiffstechnik, 1962, 47 (9).

Hydrocarbon Potential of Pre-cenozoic Strata in the North Yellow Sea Basin

CAI Feng (蔡 峰)[1,2], DAI Chunshan (戴春山)[2], CHEN Jianwen (陈建文)[2], LI Gang (李 刚)[2], SUN Ping (孙 萍)[2]

1 *China University of Geosciences, Wuhan* 430074, *Hubei, China*

2 *Qingdao Institute of Marine Geology, CGS, Qingdao* 266071, *Shandong, China*

Abstract The North Yellow Sea Basin (NYSB), which was developed on the basement of North China (Huabei) continental block, is a typical continental Mesozoic-Cenozoic sedimentary basin in the sea area. Its Mesozoic basin is a residual basin, below which there is probably a larger Paleozoic sedimentary basin. The North Yellow Sea Basin comprises four sags and three uplifts. Of them, the eastern sag is a Mesozoic-Cenozoic sedimentary sag in NYSB and has the biggest sediment thickness; the current Korean drilling wells are concentrated in the eastern sag. This sag is comparatively rich in oil and gas resources and thus has a relatively good petroleum prospect in the sea. The central sag has also accommodated thick Mesozoic-Cenozoic sediments. The latest research results show that there are three series of hydrocarbon source rocks in the North Yellow Sea Basin, namely, black shales of the Paleogene, Jurassic and Cretaceous. The principal hydrocarbon source rocks in NYSB are the Mesozoic black shale. According to the drilling data of Korea, the black shales of the Paleogene, Jurassic and Cretaceous have all come up to the standards of good and mature source rocks. The NYSB owns an intact system of oil generation, reservoir and capping rocks that can help hydrocarbon to form in the basin and thus it has the great potential of oil and gas. The vertical distribution of the hydrocarbon resources is mainly considered to be in the Cretaceous and then in the Jurassic.

Keywords seismic sequence, stratigraphic comparison, Pre-Cenozoic basin, North China (Huabei) continental block, the North Yellow Sea Basin (NYSB)

The North Yellow Sea lies to the north of the tie line between the Chengshan cape of the Shandong Peninsula and Paekryong Island of Korean Peninsula and covers a total sea area of about 8×10^4 km^2. It has a smooth seafloor. Most of the sea area is less than 50 m below the sea level and the largest water depth is 78 m[1]. The North Yellow Sea Basin is ellipse-shaped; its east boundary links to the West Korea Bay Basin and the onshore Anju Basin of Korea. The NYSB has an area of about 1.5×10^4 km^2, and the area of the West Korea Bay Basin is 3.6×10^4 km^2.

1 Survey of exploration

Received on November 8, 2004

The NYSB is the only basin without drilling among Chinas offshore petroliferous sea basins, and has only seen comprehensive geophysical reconnaissance surveys in it. Geophysical survey in the NYSB started in 1966. One of the most significant investigations was the seismic reconnaissance survey in the 121° 30′ -124° 00′ E, 37° 15′ -39° 20′ N sea area, which was carried out by the headquarters for marine petroleum explorations, Ministry of Petroleum Industry in 1977. During this survey, a 24-channel, 12-coverage digital seismic line as long as 3 884.75 km was completed. In the survey network, the main survey lines were at the intervals of 9 - 21 km, and the contact lines 15 - 30 km, covering an area of 30 000 km^2. One of the survey lines extended westwards out of the survey area to connect with those in the Bohai Sea so that comparison could be made between the two seas. By 1978, China had completed 5 082. 15-km-long seismic lines, 1 289.4-km-long marine magnetic lines, and 935-km-long gravitational lines in the North Yellow Sea [1]. However, because the seismic coverage was not enough, the seismic arrangement was short, and the data are of poor quality, there were no reflection records within 2 s. Recently, a new round of resource investigations using new technology and methods have developed in the NYSB. This also can be considered as regional supplementary investigations[2].

Since the 1970s, Korea, through open tender, carried out petroleum explorations in cooperation with foreign oil companies in the east of NYSB (called the West Korea Bay Basin by Korea) and completed 9 130-km-long digital seismic investigations. Fifteen exploring wells were drilled. Oil was hit in the Cretaceous and Tertiary strata. Well 405 could produce crude oil 60 t /d, and well 610 gave 57 t /d[2].

2 Regional geological background

The Yellow Sea area is located in the east of China. Geotectonically, it lies on the internal side of the west circum-Pacific active zone. During long geologic processes, this region was seriously reworked by orogenic movements, and as a result, great and complex tectonic changes took place. Therefore, there has been much controversy over its tectonic attribute, especially over the spread of the Qinling-Dabie orogenic belt that ran through the central China, and under the striking-slip action of the Tanlu fault zone, extended eastwards through the sea and landed at the Korean Peninsula.

Through overall integration of previous data and adding much new information to them, the authors believe that the Yellow Sea region is characterized by a wedge-like spread, and in detail, by "two platforms with a belt in between". These "two platforms" means the North China (Huabei) platform in the north and the Yangtze platform in the south; the "belt" is the large Sino-Korean orogenic belt crossing the central Yellow Sea in the range of 36° - 38° N. The belt was wedged between the two platforms, striking in the northeast direction and becoming narrower gradually. It is the huge conjoining belt between the North China and Yangtze platforms (Fig. 1).

There have been enough documents to describe the two platforms, but the Sino-Korean orogenic belt is a new concept. The belt is divided into three parts from west to east, namely, Sujiao orogenic belt, Qianliyan Rise and Imjingang orogenic belt. The Sujiao orogenic belt is mainly located in the east of Shandong and Jiangsu Provinces, and made up of Jiaobei orogenic belt, Jiashan-Xiangshui fracture zone and Shandong-Jiangsu UHP metamorphic belt.

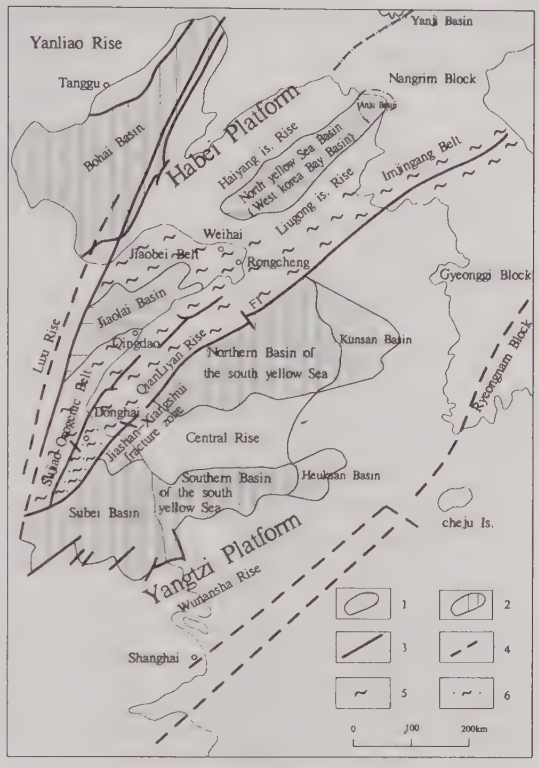

1: Mesozoic basin; 2: Mesozoic-Cenozoic basin; 3: principal fault;

4: inferred principal fault; 5: Sino-Korean orogenic belt; 6: Shandong-Jiangsu UHP belt

Fig. 1 Regional geologic tectonic units in the Yellow Sea and the adjacent regions (after CAI, 2003)

Regional geological researches indicate that the Huabei continental block corresponds with the Rangrim block of Korea (including the North Yellow Sea), and the Yangtze block with the Kyonggi block (including Jiaodong and Subei blocks and the South Yellow Sea) and that Ryonnam-Zhemin uplift and Huanan (South China) continental block lie to the south of the Okchen orogenic belt.

The studies on regional geological background of the Yellow Sea can help us understand the formation mechanisms, basin evolutions and basin types of the North and South Yellow Sea basins. The South Yellow Sea basin had its Mesozoic-Cenozoic sediments deposited on the Yangtze platform, and just in the shrinking regional geologic background due to the platform extending eastwards, in which the north and south boundaries of the platform were only < 600 km apart. The basement of the North Yellow Sea basin was the Huabei platform and denudation surface of uplifted metamorphic rocks. Therefore, these two basins differ much in genesis[3].

3 Stratigraphic features of NYSB

China has no drilling yet in NYSB, and Korea has drilled 15 wells in the east of NYSB, all reaching Mesozoic. The knowledge of the strata mainly comes from the Korean drilling data and the

nearby basin information. According to the recent and previous researches, the regional stratigraphic correlation is showed as follows (Fig. 2).

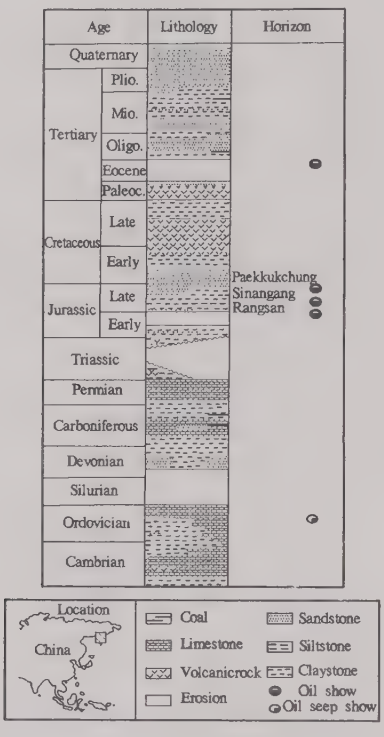

Fig. 2 Comprehensive stratigraphic column of the North Yellow Sea basin (after Lai, 1994)

3.1 Basement

In this study area, the basement is composed of the Proterozoic and Archaeozoic strata. Well 401 drilled by Korea in the east of NYSB encountered the Proterozoic at the core depth of 1 872 - 2 803 m, mainly made up of phyllite, gneiss, dolomite and limestone.

3.2 Paleozoic

The Paleozoic of the NYSB belongs to the type of Huabei platform. Well 401 encountered the Cambrian overlain by the Jurassic at the depth of 1 400 m. The Cambrian interval was 472 m thick and consisted of calcareous shale and brown limestone. The Paleozoic penetrated by Korean drilling in the east of NYSB had no Silurian-lower Devonian. The Carboniferous was coal-bearing sediment in alternations of oceanic and continental facies. The Permian was marine carbonate rock. All these differ greatly from strata of the South Yellow Sea[4].

3.3 Mesozoic

Drilling in the east of the NYSB did not give a complete Triassic-lower Jurassic section. The Permian carbonate rock directly underlaid the upper Jurassic sandstone in discordant contact. The upper

Jurassic strata were named Ryong Song subgroup, which was divided into early late Jurassic Ryong Sung Formation and the latest Jurassic Sinuiju Formation. The thickness varied. The red layer of Bak Chung Formation in the lower part of the lower Cretaceous disconformably overlaid the Ryong Song subgroup (Fig. 3).

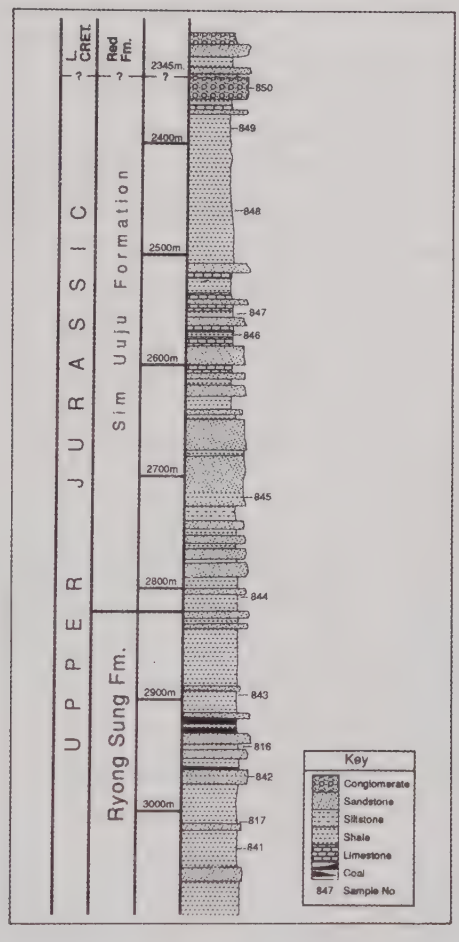

Fig. 3 Lithologic log of Jurassic strata penetrated by well 606 in the West Korea Bay basin (after Massoud et al., 1991)

The upper Cretaceous mainly consists of clay rock with minor coals in the upper that change into volcanic materials and a little sandstone downward. The lower Cretaceous is comprised by clay rock and older sandstone. Bak Chung Formation mainly consists of sandstone, which also exists in the upper Jurassic, and therefore there are more clay rocks intercalated with sandstone or some thin sandstone beds close to the upper Jurassic. The upper Jurassic also outcrops in the Yalu River drainage area in Korea and has a thickness of 2 000 m. All wells in the sea area that have encountered this set of strata do not reach its bottom, so the revealed strata are incomplete. Upper Jurassic strata can be divided on the

basis of the well 606 into two lithologic units with a total thickness of 750 m. The lower unit (Ryong Sung Formation) consists of fluvial facie siltstone, shale and alternations of sandstone and thin coal seam with a thickness of 200 m; the upper unit (Sinuiju Formation) is about 550 m thick, composed of fluvial, organic-matter-rich black shale and sandstone intercalated with thin limestone and with conglomeratic sandstone at the bottom. This core interval is the good hydrocarbon source rock of the Mesozoic basin. No completed upper Cretaceous is revealed in the well 606[5].

3.4 Cenozoic

Drills in the east of NYSB gave a Tertiary clastic rock section with the Oligocene as the bottom. This section showed alternations of thick sandstone and thin clay rock. The Miocene and Oligocene strata contained thin coal seams. We can see from the section that the clay content is low, and the sandstone acts as a good reservoir. The drilling-revealed Oligocene sandstone often gives oil and gas shows, but they are not of commercial value. Eocene strata were not discovered in the wells, and Oligocene discordantly overlaid the Paleocene volcanic rock. This lack of Paleocene-Eocene strata is similar to the Bohai Bay basin. It is inferred that with the spread of drilling, scattered Paleocene-Eocene strata will be discovered.

4 Stratigraphic correlations of the NYSB and its adjacent areas

Because the NYSB has few stratigraphic data, it is hard to establish accurate stratigraphic frame for it, and correlating it with the adjacent areas is mainly based on the neighboring Anju basin, whose stratigraphic data are used to do regional correlation with the nearby onshore Liaodong area and Jiaolai basin. The NYSB stratigraphic frame is founded on the correlations of biostratigraphy, lithostratigraphy, cyclic stratigraphy and chronostratigraphy, and also according to the seismic sequences, changes in seismic interval velocities and some drilling data.

4.1 Stratigraphic sequence and cyclic character of the Anju Basin

Results of investigations made for three times by the Qingdao Institute of Marine Geology in the Anju Basin of Korea indicated that the basin rifted apart in the Mesozoic-Cenozoic, and its basement was made up of the Archaeozoic garnet biotite granite, and the capping strata can be divided into three large sedimentary cycles, namely, fluvial-lacustrine Pongsu Formation of the upper Jurassic, fluvial-lacustrine Pakchon and Ryongban Formations of the lower Cretaceous, and fluvial-lacustrine sediments of the Paleogene. Among them, the Ryongban Formation (K_1) showed the largest lake coverage of the Anju basin, and its dark lacustrine mudstone with a thickness of 1 150 - 2 050 m has formed a very favorable assemblage of oil generation, reservoir and capping.

4.2 Stratigraphic sequence and cyclic character of the Liaodong area

Liaodong (eastern Liaoning Province) area, adjacent to the Anju basin, saw the earliest studies of Mesozoic strata in the north of China. Now, it has had a classic biostratigraphic, lithostratigraphic and chronostratigraphic section represented by the Rehe biota.

Liaodong area means the area to the east of Yingkou-Tongerpu and Yilan-Yitong faults, and has nineteen residual Mesozoic sags (such as Xinbin and Fushun sags) distributed in it. The basement of the area is Anshan and Liaodong Groups of lower Proterozoic-Archaeozoic and epimetamorphic rock of

middle-upper Proterozoic. The overlying is the Caledonian sedimentary cycle consisting of strata from Jianchang Formation of the Cambrian to Majiagou Formation of the middle Ordovician, and overlain by Hercynian cycle made up of strata from Benxi Formation of the upper Carboniferous to Shiganfeng Formation of the upper Permian. The upper Ordovician-lower Carboniferous is absent. Such cycles are typical of the North China block.

Different from the Yangtze continental block, the Zhengjia and Linjia Formations of respectively middle and lower Triassic in this area belong to the fluvial-lacustrine facies. The overlying Mesozoic-Cenozoic strata can be divided into three sedimentary cycles: the Jurassic Changliangzi and Xiaodonggou Formations of fluvial-lacustrine marsh facies, the early Cretaceous Xiaoling, Lishugou, Nieerku and Dayu Formations of fluvial-lacustrine facies (of them, the Lishugou and Nieerku Formations are lacustrine shale rich in typical Rehe fossils such as *Lycoptera*, *Eosestheria* and *Cypridea*, which can be compared with Ryongban and Pakchon Formations of the Anju basin), and the Paleogene fluvial-lacustrine sediments with thick coal seams.

4.3 Stratigraphic sequence and cyclic character of the Jiaolai Basin

This area is a Mesozoic rift basin that was developed in the background of Jiaodong (eastern Shandong) uplifting. Its basement is made up of Proterozoic gneiss, granulite, amphibolite and pyroxene diorite of Jingshan Group, and the capping rock is thick Cretaceous.

Field surveys and drilling have revealed the following stratigraphic sequence and cyclic characteristics; Laiyang Formation of lower Cretaceous is a set of fluvial-lacustrine facies, of which the Longwangzhuang and Shuinan intervals are lacustrine deposits with a thickness of 770 m and containing *Sinolycoptera* and *Estheria Yanjigensis* of Rehe biota, and can be contrasted with Anju basin and Liaodong area. The overlying strata are early Cretaceous volcanic rock series of Qingshan Formation with an isotopic age of 90 - 101.5 Ma, which is overlain by the late Cretaceous fluvial sediments of Wangshi Formation. Cretaceous in this area directly outcrops on the surface. Coal measures strata of the Paleogene Huangxian Formation are seen in the Pingdu sag, and can be correlated with those of Anju and Liaodong areas.

4.4 The North Yellow Sea Basin

According to the interpretations of drilling and seismic data together with the correlation with the Anju basin and its adjacent areas, it is known that the NYSB also has sedimentary cycles, in which the upper Jurassic is composed of fluvial-lacustrine marsh sediments with a thickness of 1 000 - 2 500 m, corresponding with the seismic structural layer T_9 - T_g, the lower Cretaceous is fluvial-lacustrine facies whose thickness is generally 1 000 - 3 000 m and corresponds to the seismic structural layer T_8 - T_9, and the Paleogene is also fluvial-lacustrine marsh sediments with a thickness of 1 000 - 3 000 m, corresponding to the seismic structural layer T_2 - T_8. These three structural layers are in discordant contact, and can be correlated with the adjacent areas.

4.5 Stratigraphic correlations between the NYSB and its adjacent areas

As mentioned above, the regional correlations are based on lithostratigraphy, cyclic stratigraphy and biostratigraphy.

4.5.1 Jurassic

The Jurassic (unpenetrated) from 2 794 to 3 091 m core depth in the well 606 of the NYSB corresponds to Pongsu Formation of Anju Basin and Xiaodonggou Formation of Liaodong area, but it is absent in the Jiaolai Basin. The typical Jurassic *Darwinula* and *Cypridea* biological assemblage was discovered in Pongsu Formation of Anju Basin, and can be compared with the *Darwinula* assemblage in Xiaodonggou Formation of Liaodong area.

4.5.2 Cretaceous

The interval from 2 070 to 2 794 m core depth in the well 606 of the NYSB can be correlated with the early Cretaceous Ryongban and Pakchon Formations of Anju basin, and also corresponding with Lishugou and Xiaoling Formations of Liaodong area and with Longwangzhuang and Shuinan intervals and the underlying strata of Laiyang Formation in the Jiaolai Basin. However, the corresponding strata with the late Cretaceous Wangshi Formation in the Jiaolai Basin and with the Dayu Formation (K_1d) in Liaodong area are absent in the North Yellow Sea and Anju basins.

4.5.3 Paleogene

Paleogene of the NYSB is a set of coal measures strata, the same as in the adjacent areas.

Correlations of regional strata and cyclic characteristics indicate that the North Yellow Sea and Anju basins and Liaodong area formed in the Jurassic, older than the Jiaolai Basin that came into being in the Cretaceous. The Paleogene rifting was mainly developed in the first three areas, forming good regional capping rocks in them, while the Paleogene strata are absent or very thin in the Jiaolai Basin, and from the viewpoint of regional evaluation, they are not so good as those in the North Yellow Sea and Anju basins. Vertically, the study area has Jurassic, early Cretaceous and Paleogene sedimentary cycles and regional assemblages of oil source, reservoir and capping rocks, which are the fundamental conditions for hydrocarbon accumulations and explorations.

5 The division of seismic sequences

5.1 Changes of seismic velocities

Interval velocity of T_2 (seafloor) in the NYSB is 1 680 - 2 200 m/s, a slow velocity, as the seafloor strata are young and have a shallow buried depth; interval velocity of T_2 - T_8 varies greatly, from 2 250 to 3 500 m/s, and is mainly related with the compaction state of the Paleogene strata, and the larger the buried depth, the greater the velocity changes; interval velocity of T_8 - T_9 is 3 600 - 4 700 m/s; that of T_9 - T_g is 4 500 - 5 200 m/s (Table 1).

The plane features show that interval velocities are higher in the northeast and west than in the central and south, indicating that the uplift positions have lower interval velocities because of shallower buried depth and less intensive compaction than the depressions. So the compaction is the major controlling factor of the regional changes in interval velocities.

The NYSB has the following characteristics of interval velocity: (1) With the increase of buried depth, interval velocity generally increases accordingly, indicating an increasing compaction state. (2) A discordant plane is a sudden velocity change surface. All interfaces in the NYSB show sudden velocity changes. (3) Buried depth has great influence on interval velocity. The younger the strata, the larger the influences the buried depth has on the interval velocity.

Tab. 1 Changes in interval velocities in the Yellow Sea

Horizon	T_5 - T_g	T_0 - T_2	T_2 - T_8	T_8 - T_9	T_9 - T_g
Geologic age	J	Q + N_2	E	K	J
Interval velocity / m • s^{-1}	5 000 - 6 500	1 780 - 2 200	2 250 - 3 500	3 600 - 4 700	4 500 - 5 200

5.2 Corresponding relations of seismic velocity with the seismic wave group and strata

Since the NYSB does not have drilling so far, there are no drilling and logging data used to mark seismic layers, and thus the features of seismic wave group and velocity are used to do the work.

Totally four characteristic waves T_2, T_8, T_9 and T_g in the North Yellow Sea basin are interpreted. Of them, T_2, T_8 and T_g waves have reflected three regional unconformity interfaces. T_2 and T_8 have relatively strong wave energy and good continuity and can show obvious regional unconformity interfaces, and therefore are considered to be standard waves of the area (Fig. 4).

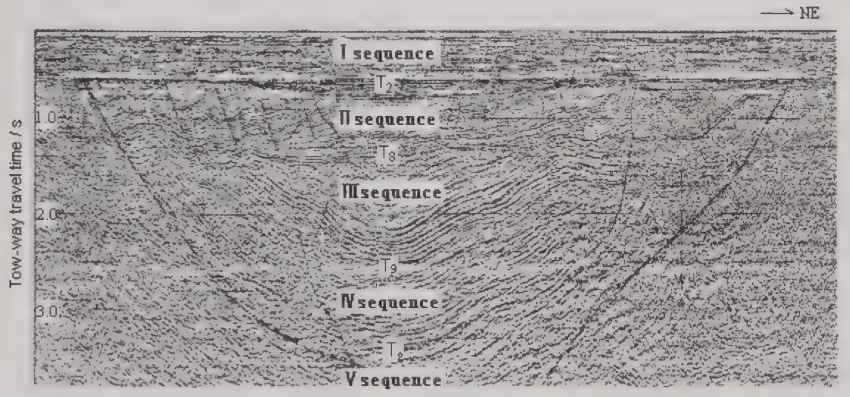

Fig. 4 Seismic profile showing the seismic sequence of the NYSB

5.2.1 T_2 Wave

T_2 wave usually has two phases, strong wave energy, steady waveform and good continuity, and can be traced in the whole area. We can see from the seismic profile that the events of the overlying reflection wave groups lap on the T_2 wave one by one, and those of the underlying terminate at the T_2 wave, indicating that the T_2 wave is respectively in discordant onlap and truncation contact with the overlying and underlying reflection wave groups.

T_2 wave is distributed in the whole area, and its two-way travel time is 0.5 - 1.9 s.

5.2.2 T_8 Wave

T_8 wave has strong-medium wave energy, good continuity, two phases and unsteady waveforms. Its apparent cycle is 25 - 35 ms, and apparent frequency 30 - 38 cycles. Though the waveforms are not stable enough, they have obvious characteristics, and can be traced through the area.

T_8 wave has different reflection characteristics from the overlying and underlying wave groups, and are in clear discordant contact with them. As showed in Fig. 4, the overlying wave group obviously laps

on T_8, and the underlying wave group truncates T_8, which can be seen in all the depressions. It is inferred from this that T_8 wave has reflected in the seismic profile a strong tectonic movement that occurred in the late time of the Mesozoic.

From the seismic profile we can see that the overlying and underlying seismic waves of T_8 have different geologic parameters such as reflection configuration, abundance, frequency and continuity, suggesting a superimposition of two separate basins of different origins and formation periods. T_8 wave in the area merged into the overlying T_2 wave and disappeared in the high position of the depression edge. The two-way travel time of T_8 wave ranges from 0.58 to 2.33 s, and generally the range is larger from west to east and from south to north.

5.2.3 T_9 Wave

T_9 wave has relatively unsteady phase, energy, waveform and continuity. According to the changes, they can be divided into two types: the "east type" (the eastern and first central sags) and the west type (the western, second central and southern sags).

(1) East type

T_9 wave has strong-medium energy (weaker in a few profiles), good-medium continuity, two phases and relatively steady waveforms in most of the seismic profiles. Its apparent cycle is about 30 ms, and apparent frequency 33 cycles. Generally, it can be traced for a long distance. T_9 wave acts as the base boundary of a dense reflection zone and the top of a weak reflection zone (Fig. 4).

(2) West type

T_9 wave shows poor stability and continuity, and the energy becomes weaker as well. Thus, it is difficult to trace it for distances. In this case, the correlation is mainly based on: ① for profiles with obvious characteristics, using the method of profiles intersection closure to extrapolate T_9; ② using the differences in reflection configurations between the upper and lower stratigraphic sequences; ③ using faults to partition the seismic profile into different blocks, and then using the relatively stable time interval in one of the blocks to deduce and interpret.

We can see from the seismic profiles that the overlying wave group (or overlying strata) of T_9 wave is obviously controlled by faults along sag boundaries, but the underlying wave group (or underlying strata) is generally not controlled by fault. T_9 wave is in unconformity contact with the overlying and underlying wave groups, and it merges into the overlying T_2 wave and disappears at the high positions of the sags. The two-way travel time of T_9 wave is 0.67 - 3.3 s.

5.2.4 T_g Wave

T_g wave is the base reflection wave. Because the seismic profiles are not of good enough quality and the subsurface geologic structures are very complicated, the wave does not have very stable characteristics. For instance, T_g wave in the east of survey line E_3 shows two strong phases with medium continuity, and have 2 s dense reflections in the upper part and blank and chaotic reflections in the lower. T_g wave in this section can be continuously traced. However, the wave is hard to trace in most of the profile sections.

The two-way travel time of T_g wave is 0.84 - 4.35 s, generally similar to the overlying strata. The maximum reflection time is located in the eastern and northern sags, and the minimum in the west and south of the basin.

5.3 Division of seismic sequences

It is one of the basic tasks of seismic interpretation to use reflection configurations and wave group reflections in seismic profiles to divide seismic sequences and then interpret the geologic attributes. From the above-mentioned reflection wave configurations and contacts between the wave groups, we know that in the time section of the NYSB, there are three reflection waves from three large unconformable planes and one wave from a secondary unconformable plane, which are T_2, T_8, T_g and T_9 respectively. According to this and together with the drilling data of Korea and our understanding of the regional strata in the North Yellow Sea, five seismic sequences can be given in the time section, that is, I, II, III, IV, and V from top to bottom (Fig. 4; Table 2). These five seismic sequences have also given clues that the North Yellow Sea basin underwent a tectonic evolution from early depression development to depression-fault transformation and then to fault depression. The characteristics of the five seismic sequences are given below.

Tab. 2 The division of seismic sequences of the NYSB

Geologic boundary		Contact	Seismic sequence	Contact	
System	Series			Top	Bottom
Neogene		T_2	I		Onlap
Paleogene		T_8	II	Truncation	Onlap
Cretaceous	Lower	T_9	III	Truncation	Onlap - conformity
Jurassic		T_g	IV	Truncation - conformity	Onlap
Pre-Mesozoic			V	Truncation	

5.3.1 Seismic sequence I

Seismic sequence I is distributed in the whole basin area, and its first reflector overlies T_2. It has a sheet-like drape, and the reflections are parallel and dense. The internal structures of the sequence are parallel-subparallel, and the interval velocity ranges from 1 780 to 2 200 m/s. In general, this seismic sequence can be divided into two parts: the upper consists of a set of dense reflections with certain reflection energy, and the waveform is steady, well continuous and strong in amplitude; the lower part has generally weak energy and not good enough continuity. It is inferred from the reflection characteristics that lithologically, this seismic sequence is composed of sandstone and mudstone formations in stable sedimentary environments, and geologically considered to be Neogene and Quaternary sediments.

5.3.2 Seismic sequence II

The reflection waves between T_2 and T_8 are grouped under the seismic sequence II. It consists of multiple parallel, dense and wedge-like reflections with strong amplitude and good continuity. The internal reflections are subparallel and have strong energy, high frequency and good continuity. The interval velocity is 2 250 - 3 500 m/s. It is inferred from the reflections that this seismic sequence is alternations of littoral, shallow lake-fluvial sandstone and mudstone, and belongs to the Paleogene.

Seismic sequence II is respectively in truncation and onlap contact with the overlying and underlying strata.

5.3.3 Seismic sequence III

The reflection waves between T_8 and T_9 are grouped under the seismic sequence III. The external shape of the sequence is roughly sheet-like. It has a subparallel reflection structure and an interval velocity of 3 600 - 4 700 m/s. This seismic sequence can be divided into two parts: the upper consists of a set of sparse reflections with weak amplitude, low frequency and medium-low continuity, indicating relatively homogeneous lithologic characters. Together with the regional stratigraphic correlations, the sequence is believed to be semi-deep lacustrine sediments dominated by mudstone, which is one of the most important source rocks in this area. The lower part consists of a set of dense reflection sections with strong amplitude, low frequency and good continuity, suggesting that this set of strata is fluvial-deltaic sandstone and mudstone.

Taking it as a whole, this seismic sequence shows a stable sedimentary environment and deep water at that time, but the water area may have slightly shrunk compared with that in the Jurassic. This indicates that the early Cretaceous marked the change from depression to fault, and the sequence suggests the end of the depression stage and the beginning of the fault age.

Seismic sequence III is in truncation contact with the overlying strata and in onlap contact with most of the underlying. Conformity or disconformity occurs in the deep depression position.

5.3.4 Seismic sequence IV

The reflection waves between T_9 and T_g are grouped under the seismic sequence IV.

This seismic sequence consists of a set of nearly parallel reflections with a sheet-like external form. The parallel-subparallel internal reflections show strong amplitude, low frequency and medium continuity. The interval velocity is 4 500 - 5 200 m/s. It can be seen from seismic profiles that the deposition of this sequence was not controlled by faults along sag boundaries. The dominant alternations of lacustrine-fluvial sandstone and mudstone suggest the depression development stage of the basin. The sediments are considered by seismic interpretations to be Jurassic in geologic attribute. The seismic sequence is respectively in truncation and baselap contact with the overlying and underlying strata.

5.3.5 Seismic sequence V

The reflections below T_g wave belong to the seismic sequence V.

The internal reflection shows chaotic or blank structures, and the amplitude varies. The continuity is generally poor, but well continuous homophase axes in the deep can be seen in some profiles.

6 Tectonic divsion

6.1 Characteristics of gravity field

According to the characteristics of gravity field in the Yellow Sea area, the Bouguer anomaly is generally higher in the north and east than in the south and west. The anomaly unusually strikes in the northeast and near east-west directions. The following anomalous zones can be given.

6.1.1 High anomalous value zone in the north

This anomalous zone trends roughly parallel to the coastline to the north of it, and regionally belongs to the Haiyang Island Rise. The maximum anomalous value is +39 mGal, consisting of a series of NE normal anomalies or nose normal anomalies.

6.1.2 Low anomalous value zone in the center

This zone is located in the center of the North Yellow Sea, near 38N. It is about 220 km long, 80 km wide and covers an area of 15 000 km^2. Regionally, this anomalous zone, in the shape of an inverted triangle, belongs to the North Yellow Sea basin and spreads in the northeast direction. It consists of a series of negative and normal anomalies. Its east part comprises six negative anomalies and one nose negative anomaly. The minimum value of negative anomalies in the east part is -10 mGal. Its west part is composed of an obvious beaded negative anomaly and a nose negative anomaly. The minimum value of the negative anomalies is -6 mGal. The normal anomaly in the middle wedges apart the negative anomalies in the west and east parts, forming a saddle structure in the middle. This normal anomaly zone in the middle is 40 km long, 35 km wide and covers an area of 1 400 km^2. The maximum value of the normal anomaly is +26 mGal.

6.1.3 High anomalous value zone in the south

This zone is located in the south of the North Yellow Sea, and belongs to the Liugongdao Rise. It is 200 km long, about 30 km wide and consists of three anomalous belts, namely, the high anomalous belt in the east, the low anomalous belt in the middle and the high anomalous belt in the west.

6.2 Characteristics of magnetic field

The magnetic field of the North Yellow Sea can be divided into four zones.

6.2.1 The normal magnetic anomaly zone in the central north

This magnetic anomaly zone is located in the extent of 122° - 123° 30′ E and 38° 10′ - 39° N. The anomaly changes gently, and mainly strikes in northwest and northeast directions. There is a normal magnetic anomaly associated with two negative anomalies to the south of 39° N. The value of the normal magnetic anomaly is +60 nT, and the two negative anomalies are -140 nT and -180 nT respectively.

6.2.2 The normal magnetic anomaly zone in the center and south

This zone (122° -123° E, 36° - 38° 10′ N) is located in the south of the North Yellow Sea and extends straight to the northern basin of the South Yellow Sea. Magnetic anomaly varies acutely. Its strike changes from the northeast direction in the south to the south-north direction in the middle and then to the northeast in the north. A single normal magnetic anomaly often shows a northeast trend or isometric form. Negative magnetic anomalies, usually small in range, scatter here and there in the normal ones. The maximum anomalous value is +280 nT and the minimum -220 nT in the area.

6.2.3 The magnetic field zone in the west

It is located in the west of the North Yellow Sea and dominated by negative magnetic anomalies. Normal magnetic anomalies are usually very small in range and scatter in the negative ones. The maximum anomalous value is +160 nT, and the minimum - 260 nT.

6.2.4 The magnetic field zone in the east

This zone is located in the east of the North Yellow Sea and mainly in the background of negative magnetic anomaly. The anomalies in the north trends towards northwest, and those in the south spread in northeast and east-west directions.

6.3 Tectonic division

According to characteristics of gravity field, magnetic field, basement and capping rocks, the

NYSB can be divided into seven secondary structural units of which there are four negative units (sag) and three positive units (swell). They are the western sag, western swell, first and second central sags, central swell, southern sag, eastern swell, and eastern sag from west to east (Fig. 5).

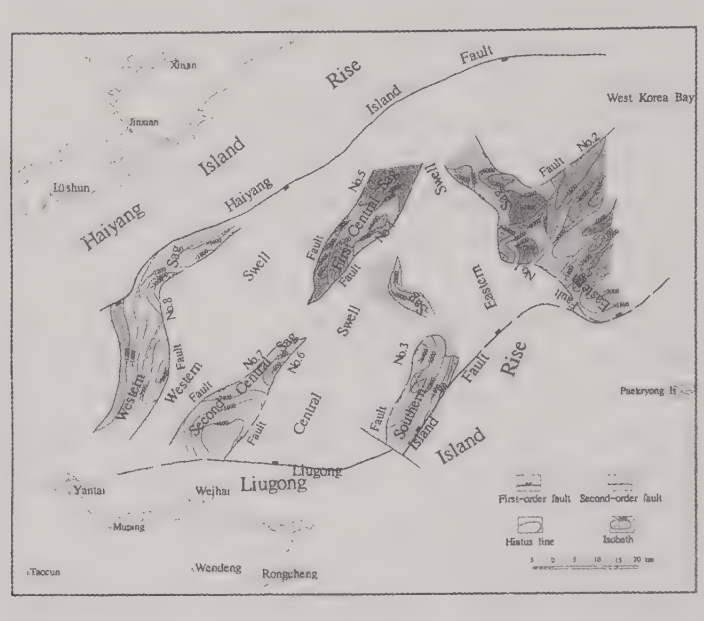

Fig. 5 Tectonic division of the North Yellow Sea basin

6.3.1 Eastern sag

The eastern sag is located in the northeast of the North Yellow Sea basin and covers an area of 3 950 km^2. Now all the drillings of Korea are in this sag. It is bounded on the north by the fault No.2 and on the south by the fault No.1, showing an asymmetrical double-fault structure, steep in the west and gentle in the east. The pre-Mesozoic basement of the sag is made of the Paleozoic, and the biggest Cenozoic-Mesozoic thickness comes to 8 200 m. It is the biggest sag of the NYSB considering the area and sediment thickness.

According to the strata revealed by Korean wells 604 and 602 and the seismic profiles, strata are completely developed within the sag. The thickness of the Quaternary and Neogene is 500 - 600 m; the maximum residual thickness of the Paleogene is 3 000 m; the lower Cretaceous is 3 000 m thick; the Jurassic is 2 500 m thick. The depocenters regularly move from old to young and from west to southwest.

In the eastern sag, from south to north are in turn arranged fault terrace belt, horst-anticline belt and reversed anticline-graben belt. The fault terrace belt, with an area of 500 km^2, is located in the southeast of the sag and consists of two parts: fault horst and fault step, which go in the northeast direction and whose major structural types are faulted anticline and fault nose; the horst-anticline belt, trending towards northeast, lies in the central part of the sag and covers an area of 1 250 km^2. The major structural types are faulted anticline and half-anticline. Its south and north parts are deep depression areas of the eastern sag and have sufficient hydrocarbon supply, so it is the best petroliferous belt in the

sag. The reversed anticline-graben belt is located in the north of the sag, has an area of 460 km^2 and trends towards northwest. Its major structural types are reversed anticline and graben. The southeast of the belt is close to the hydrocarbon-generating depression area, and therefore it can be regarded as a favorable structural belt.

6.3.2 Central sag

The central sag can be divided into the first central sag in the south and the second central sag in the north.

The first central sag covers an area of 1 125.0 km^2 and is bounded by faults No.4 and No.5. These two faults go towards south and merge into one, and the sag disappears there. The basement is Proterozoic metamorphic rock. It is an asymmetric graben or fault-depression trending to NNE and generally deeper in the south and west than in the north and east. According to the interpretation of seismic profiles, the well-developed Quaternary, Neogene, Paleogene, lower Cretaceous and Jurassic in the sag have their maximum residual sediments as thick as 500 m, 2 500 m, 3 000 m and 3 000 m respectively.

The second central sag, spreading in the NNE direction, covers an area of 1 175.0 km^2 and is bounded by faults No.6 and No.7. It is an asymmetric graben or fault-depression, deeper in the east than in the west. The depocenter is located in the center of the fault-depression. According to the seismic interpretation, the sags Q + N is 500 - 800 m thick, E 0 - 1 500 m thick, the residual thickness of K_1 is about 0 - 1 000 m, and the maximum residual thickness of J is 1 200 m.

6.3.3 Southern sag

The southern sag is located to the south of the eastern and central swells and has an area of 1 062.0 km^2. It is sandwiched between the fault No.3 and the Liugong Island fault, showing an asymmetric graben or fault-depression and trending towards NNE. The basement is Proterozoic metamorphic rock. The depocenter lies in the northwest of the fault-depression.

According to the interpretation of seismic profiles, the thickness of Quaternary and Neogene is 500 - 600 m; the residual thickness of the Paleogene is 2 000 m; the thickness of lower Cretaceous is 1 000 m; the thickness of Jurassic is 1 000 m.

6.3.4 Western sag

The western sag is located in the westernmost part of the basin and covers an area of 2 475.0 km^2. It is bounded by the fault No.8, and is a long-narrow, asymmetric graben. The sag is S-shaped, going to the northeast in the north, turning to near south-north in the middle and then to the southwest in the south. The basement is Proterozoic metamorphic rock.

According to seismic profiles, the thickness of Quaternary and Neogene is 300 - 650 m; the residual thickness of Paleogene is about 500 m; the biggest residual thickness of lower Cretaceous is 1 000 m; and the thickness of Jurassic is 500 - 900 m.

7 Petroleum geological conditions

The geochemical data mainly come from the Korean drilling data, as China has no drilling in the NYSB yet.

There are three sets of hydrocarbon source rocks in the North Yellow Sea: respectively (1) black

shale of Paleogene; (2) black shale of Jurassic; (3) black shale of Cretaceous. Among them, the black shale of Mesozoic acts as the major hydrocarbon source rock in the basin. TOC of the Paleogene, Cretaceous and Jurassic black shale is 0.5 - 0.7, 1.6 and 0.9 - 1.66 respectively, the content of chloroform asphalt A is 0.01 - 0.001, 0.203 and 0.102 respectively, and the content of total hydrocarbon is < 1 000, 1 000 - 1 800 and 800 - 1 000 respectively. The kerogen type of hydrocarbon source rock is III, I and II_1 respectively. All these have reached the standard of good source rocks. Ro is 0.60 - 0.40, 0.73 - 0.80 and 0.71 - 1.32 respectively, also coming up to the standard of mature source rocks[6].

The reservoirs of the NYSB are Mesozoic-Cenozoic high porosity sandstone and pre-Mesozoic fissured carbonate rock. The Paleogene reservoirs are rich in pores, the porosity is 20 % - 35 %, and permeability 1 000 md; the lower Cretaceous reservoirs are both pore and fissured types, the porosity is 17 %, and permeability 200 md; the upper Jurassic reservoirs are also pore and fissured types, the porosity is 13 %, and permeability 25 md; the Paleozoic reservoirs are of the fissured type, and the porosity is 10 %[6].

8 Conclusion

The NYSB has undergone two great tectonic evolutions: rifting and strike-slip-extension. It has three sets of hydrocarbon source rocks dominated by lower Cretaceous and forms multiple petroliferous systems of pre-Mesozoic basement, Mesozoic and Paleogene. The oil-bearing system of Mesozoic is the major exploration play in the basin. Its source rock is lower Cretaceous and upper Jurassic, and regarded as a closed pool-forming dynamic system as the oil and gas are considered to migrate for short distances. Commercial oil has been discovered in the eastern Mesozoic sag of the NYSB by Korea, indicating that the NYSB is a real Mesozoic-Cenozoic petroliferous basin.

References

[1] Editorial Board of Petroleum Geology of the Coastal Continental Shelf and the Adjacent Sea Areas. *Hydrocarbon Areas in the Coastal Continental Shelf and Adjacent Sea Areas (Volume I)*. Petroleum Industry Press, Beijing, 1990, 263-277.

[2] FENG Zhiqiang, et al. New understanding of Mesozoic-Paleozoic geologic structures and oil prospects in the Yellow Sea. *China Offshore Petroleum (Geology)*, 2002, 16 (6): 367-373.

[3] CAI Qianzhong. Application of geotectonic study to the explorations for oil and gas in the east of China. *Marine Geology and Quaternary Geology*, 1991, 11 (4): 4-5.

[4] LAI Wan-zhong (translation). Lithology and Hydrocarbon Distribution in the West Gulf. *Foreign Offshore Petroleum*, 1994, 9 (3): 30-31.

[5] Massoud M S, Kinops S D, Scott A C, et al. Oil source rock potential of the lacustrine Jurassic Sinuiju Formation, West Korea Bay Basin; Part I: Oil-source rock correlation and environment of deposition. *Journ. Petrol. Geol.*, 1991, 14 (4): 365-385.

[6] Massoud M S, Scott A C, Mattey D, et al. Oil source rock potential of the lacustrine Jurassic Sinuiju Formation, West Korea Bay Basin; Part II: Nature of the organic and hydrocarbon-generation history. *Journ. Petrol. Geol.*, 1993, 16 (3): 265-284.

A New Method of Profiling Remote-Sensing Reflectance of Coastal Waters

LI Tongji (李铜基), CHEN Qing lian (陈清莲), WANG Xiao yong (汪小勇), YANG An'an (杨安安)
National Ocean Technology Center, Tianjin 300111, *China*

Abstract The profiling method is the first method to select in measuring the remote-sensing reflectance. In the light of the characteristics of China's coastal waters, we develop a new method to compensate the environment's effects with the downwelling irradiance's profile and to estimate the underwater remote-sensing reflectance $r_{rs}(\lambda)$. The result indicates that the relative deviation of repetitious $r_{rs}(\lambda)$ in one station is around 10 %.

Keywords profiling method, remote-sensing reflectance, method

1 Introduction

Remote-sensing reflectance $R_{rs}(\lambda)$ is a basic physical quantity of ocean colour remote-sensing, and is defined as[1, 2, 3]:

$$R_{rs}(\lambda) = \frac{L_w(\lambda)}{E_s(\lambda)} \tag{1}$$

Where, $L_w(\lambda)$ is the off-water irradiance and $E_s(\lambda)$ the total incident irradiance from sea surface. $E_s(\lambda)$ may be directly measured by the irradiance sensor while there are two methods available for the *in situ* measurement of off-water radiation luminance[4]: the profiling method (also called the under-water method) and the above-water method .The profiling method is less influenced by environmental factors (such as straight sunlight reflection, sky diffusion reflection, *etc.*) and can obtain the internal information of the water body, which may be used for detailed analysis and treatment of such problems as stratification effect of the water body in the later stage of treatment, so this method is the first to select internationally[1, 2].

Based on the principles of profiling[1, 2, 3], supposing the optical properties of the water body with the water area at the observed depth are uniform, the diffuse attenuation coefficient $K_L(\lambda)$ of the upwelling spectral radiation luminance of the water body may be obtained by using the upwelling radiation luminance of the water body at different depths of Z_1 and Z_2, $L_u(\lambda, Z_1)$ and $L_u(\lambda, Z_2)$.

$$K_L(\lambda) = \frac{1}{Z_2 - Z_1} \ln \frac{L_u(\lambda, Z_1) / E_S(\lambda, t_{Z1})}{L_u(\lambda, Z_2) / E_S(\lambda, t_{Z2})} \tag{2}$$

Received on October 8, 2004

Where, t_Z represents the measuring time of surface unit when the profile unit measures the optical parameters at the water body at the depth of Z. The role of $E_S(\lambda, t_Z)$ in the formula is to compensate for the variations of light conditions in the course of measurement.

Having obtained $K_L(\lambda)$, the off-water radiation luminance may be got by extrapolating the upwelling radiation luminance data at a given depth:

$$L_w(\lambda) = \frac{1-\rho(\lambda)}{n_w^2(\lambda)} L_u(\lambda, Z_1) e^{K_L(\lambda) Z_1} \tag{3}$$

Where, $\rho(\lambda)$ is the Fresnel's reflectivity of seawater, and $n_w(\lambda)$ the refraction index.

It can be seen from above that the key to the accurate measurement of $R_{rs}(\lambda)$ by the profiling method is to calculate precisely the diffuse attenuation coefficient $K_L(\lambda)$ of the upwelling spectral radiation luminance. For the class Ⅰ oceanic waters[5], as $K_L(\lambda)$ is smaller, *i.e.*, the equivalent optical depth Z_{90} is larger, sufficient effective data may be obtained at greater depths to calculate the optical properties of the water body at shallower depths. But, in the class Ⅱ waters, such as the Yellow Sea and East China Sea areas, although the water may also be supposed to be horizontally stratified and the optical properties within the upper water body are more uniform, the incident irradiance attenuates quickly with depth due to the increase in the concentration of water colour components in the water and Z_{90} is smaller so that there are few effective data available for estimation of the optical properties of the near-surface water body. Besides, due to the sea surface wave action, there exist greater random errors in the near-surface $L_u(\lambda, Z)$, thus increasing uncertainty of the off-water radiation luminance obtained from calculation.

Based on the technical characteristics of *in situ* measurements by optical profilers and in the light of the near-shore class Ⅱ waters, this paper introduces the downwelling irradiance $E_d(\lambda, Z)$ at various depths of the water body in extrapolating the optical field measurement data of the water body to the sea surface and proposes a new technical method of computing $R_{rs}(\lambda)$. Through analysis of the cruise No. 200304 data, the relative deviation of repetitions $R_{rs}(\lambda)$ may be controlled within 10 %.

2 Methods and principles

Usually, in the course of measuring with the optical profiler, another auxiliary device-optical surface meter is used for measuring $E_s(\lambda)$ synchronously. The $E_s(\lambda)$ data are used for normalizing the upwelling radiation luminance $L_u(\lambda, Z)$ profile of the water body apart from being used for the calculation of the final, $R_{rs}(\lambda)$, *i.e.*, to remove the variations of the total incident radiation luminance on the sea surface in the course of measurement. But the $E_s(\lambda)$ sensor is generally over 30 m away from the $L_u(\lambda, Z)$ sensor, which is mainly because the measurement of $L_u(\lambda, Z)$ needs to avoid the shallow effect of ships. For the sea areas dominated by the ferruginous aerosols in China's offshore

waters, such a distance is enough for the normalized $L_u(\lambda,Z)$ to retain much of the effect of light variations, especially for the measurement under nonideal weather conditions. Furthermore, the $E_s(\lambda)$ measurement is conducted above sea surface, the correction of its data for $L_u(\lambda,Z)$ cannot reduce the effect of sea surface waves.

However, in the normal optical profiling, while $L_u(\lambda,Z)$ is being measured, the downwelling irradiance $E_d(\lambda,Z)$ is measured on the same apparatus. As $E_d(\lambda,Z)$ and $L_u(\lambda,Z)$ are measured at the same location, depth and time, $E_d(\lambda,Z)$ carries all the information concerning the effect of various factors (such as wave, atmosphere, *etc.*) above this depth on the incident irradiance .Thus the $L_u(\lambda,Z)/E_d(\lambda,Z)$ parameter will largely remove the influences from the outside environment. As this parameter has the similar physical implications as $R_{rs}(\lambda)$, it may be defied as [6]:

$$r_{rs}(\lambda,z)=\frac{L_u(\lambda,Z)}{E_d(\lambda,Z)} \tag{4}$$

$r_{rs}(\lambda,Z)$ reflects the equivalent optical reflection properties of the water below the depth Z, and may be referred to as the remote-sensing reflectance under water. When supposing the optical properties of the water body at the 0 - Z depth are uniform and $r_{rs}(\lambda,Z)$ does not vary with depth, it may be expressed as $r_{rs}(\lambda)$.

As there is the following relationship between $E_s(\lambda)$ and $E_d(\lambda,0^-)$ [1,2]:

$$E_s(\lambda)=\frac{1-\bar{r}(\lambda)R(\lambda)}{1-\bar{\rho}(\lambda)}E_d(\lambda,0^{-1}) \tag{5}$$

Where $\bar{r}(\lambda)$ is the Frenel's reflectivity at the air-sea interface, and the numerical value is 0.48, $\bar{\rho}(\lambda)$ is the intrinsic Frenel's reflectivity of the air-sea interface and the numerical value is within 4 - 6 %. $R(\lambda)$ is the irradiance ratio. We have [1,2]:

$$R(\lambda)=\frac{E_u(\lambda,0^{-1})}{E_d(\lambda,0^{-1})}=Q\frac{L_u(\lambda,0^{-1})}{E_d(\lambda,0^{-1})} \tag{6}$$

Where Q is the relational factor between the upwelling radiation alluminance and irradiance.

According to (5) and (6) as well as (3), the relationship between $r_{rs}(\lambda)$ and $R_{rs}(\lambda)$ can be expressed as:

$$R_{rs}(\lambda)=\frac{1-\rho(\lambda)}{n_w^2(\lambda)}\frac{1-\bar{\rho}(\lambda)}{1-\bar{r}(\lambda)\cdot Q\cdot r_{rs}(\lambda)}r_{rs}(\lambda) \tag{7}$$

Lee (2002) gave the above relationship as[7]:

$$R_{rs}(\lambda)=\frac{0.52}{1-1.7r_{rs}(\lambda)}r_{rs}(\lambda) \tag{8}$$

3 Results of Application

To analyse the application results of the above-mentioned method, we made a test by using the data obtained for China's Yellow Sea waters in April, 2004. In this test, we used the 9-channel optical profiler (SPMR/SMSR) to conduct the measurement of the optical depth profiles and there were a total of 72 stations for the *in situ* effective measurement of optical depth profiles, as shown in Fig.1. In the measurement of each station, 2-3 individual profilings were made. This paper uses the relative deviations of the individually measured results of each station (See formula (9)) to evaluate the application results of the method.

$$\delta(\lambda) = \frac{\frac{1}{N}\sum_{i=1}^{N} | r_{rs}(\lambda, i) - \overline{r_{rs}(\lambda)} |}{\overline{r_{rs}(\lambda)}} \tag{9}$$

Where, $r_{rs}(\lambda, i)$ is the $r_{rs}(\lambda)$ of the ith measurement; N, the total number of measurements; $\overline{r_{rs}(\lambda)}$ is the mean value of $r_{rs}(\lambda)$ of the N th measurement.

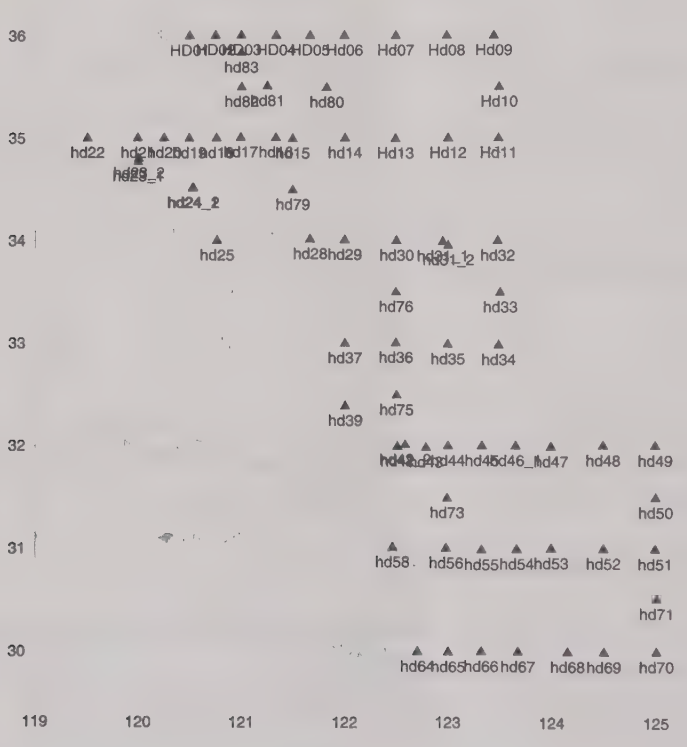

Fig. 1 The effective observation stations of SPMR/SMSR for the cruise No. 200304

Here, the first profiling data of the station HD01 (hdo1-a) are taken for example to elaborate the calculation process for $r_{rs}(\lambda)$. Fig. 2 gives the $r_{rs}(\lambda, Z)$ obtained from this measurement.

It can be seen from Fig. 2 that the variation of $r_{rs}(\lambda, Z)$ in different wave lengths is smaller within a given depth and this variation is attributed to the non-uniform water body, or the effect of residual

waves and the measurement fluctuation of apparatus. The $r_{rs}(\lambda, Z)$ at 412 nm and 443 nm increases suddenly at the water depth of around 7 m, which is mainly due to the increase in the turbidity of the lower water body, or possibly the action of submarine effect (The water depth of this station is about 18.5 m).

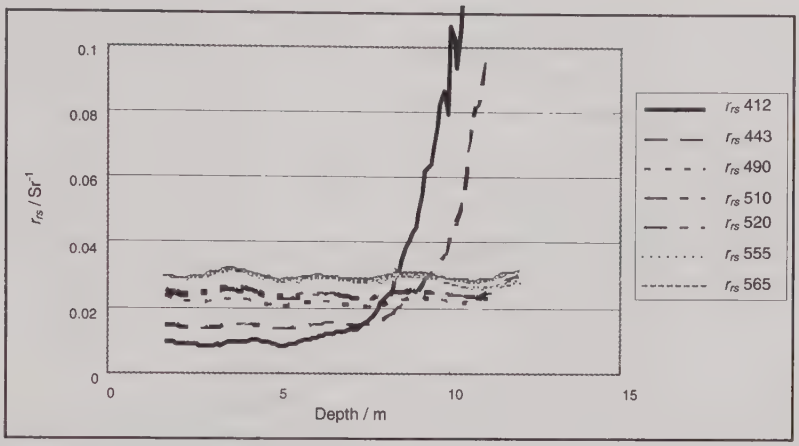

Fig. 2 $r_{rs}(\lambda, Z)$ obtained from HD01-a profiling

For various wave bands, more stable depth ranges of $r_{rs}(\lambda, Z)$ are chosen, and the "representative" $r_{rs}(\lambda)$ can be got through the modal means. Table 1 gives the analytical results of $r_{rs}(\lambda, Z)$ at the wave band of 565 nm in this profiling.

Tab. 1 Analytical results of $r_{rs}(\lambda, Z)$ at the 565 nm of the HD01-a profiling

Numerical range	Number of data	Modal means	Mean-square deviation
0.027 - 0.028	2		
0.028 - 0.029	30		
0.029 - 0.030	42	0.029 6	0.01
0.030 - 0.031	16		
0.031 - 0.032	14		

Based on the above-mentioned method, Fig. 3 gives the $r_{rs}(\lambda)$ obtained from the measurement of all the 72 stations. To test the effects of this method for data processing, the relative deviation of repetitions $r_{rs}(\lambda)$ is calculated according to (9). Fig. 4 gives the distribution of the relative deviations from repetitions measurement of 72 stations in the cruise No. 200304.

It can be seen from the diagram of relative deviation analysis that the relative deviation of $r_{rs}(\lambda)$ obtained from the repetitions measurement can basically be controlled within 10 %, which reflects the

repetitivity of optical profiling and good data treatment.

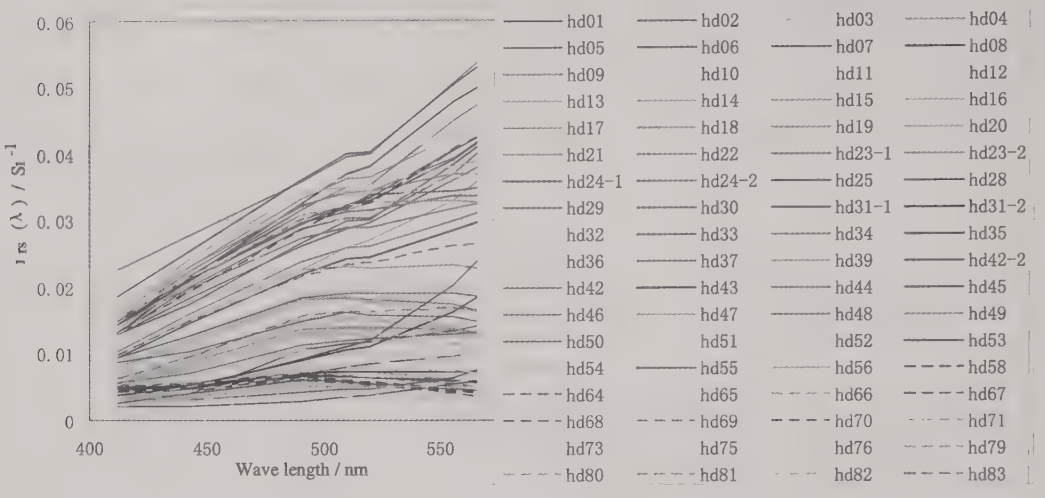

Fig. 3 $r_{rs}(\lambda)$ obtained from the measurement of 72 stations in the cruise No. 200304

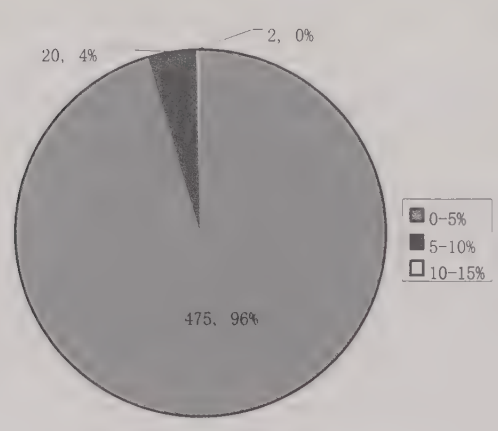

Fig. 4 Distribution of relative deviations $r_{rs}(\lambda)$ in the 72 stations during the cruise No. 200304

According to (8), $R_{rs}(\lambda)$ may be calculated from $r_{rs}(\lambda)$. Fig. 5 gives the $R_{rs}(\lambda)$ calculated from the above-mentioned 72 stations.

This paper only gives the calculated relative deviation analysis of $r_{rs}(\lambda)$, but does not analyse directly the relative deviations of repetitions measurement of $R_{rs}(\lambda)$, for which the main considerations are as follows:

(1) In the calculation of $R_{rs}(\lambda)$, the calculation of $r_{rs}(\lambda)$ is an important kernel parameter while for the development of such algorithms as the *in situ* pigment model research, to use $r_{rs}(\lambda)$ is a

commonly adopted method. As $r_{rs}(\lambda)$ evades from the uncertainty of light transmission in the air-sea interface, the research on various algorithms may be made simpler and the target may become more concentrated.

(2) Although the relationship between $R_{rs}(\lambda)$ and $r_{rs}(\lambda)$ (Formula (8)) proposed by Lee (2002) is of some universality, its applicability to the China's coastal waters has not been well tested. It can be seen from (7) that the various parameters involved in the relationship between $R_{rs}(\lambda)$ and $r_{rs}(\lambda)$ still need to be further studied.

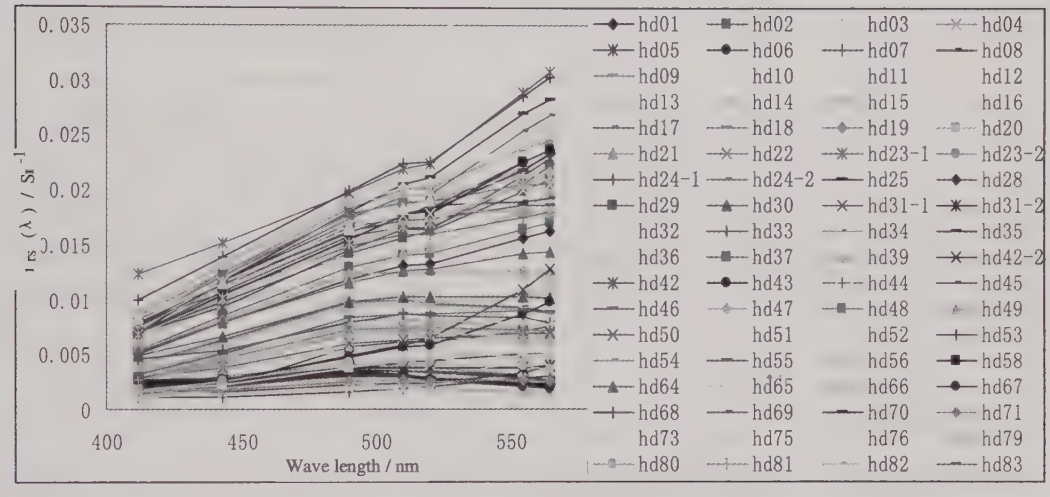

Fig. 5 Measured $R_{rs}(\lambda)$ from 72 stations during the cruise No. 200304

4 Discussion and conclusions

In the Chinas coastal waters, such as the Yellow Sea and East China Sea areas, the water depth is smaller, the concentration of water colour components is large and the composition is complex, which increases the uncertainty in using the conventional methods of processing the optical profile data to inverse $R_{rs}(\lambda)$. This paper proposes the method of inversing $r_{rs}(\lambda)$ by using the synchronously measured $E_d(\lambda, Z)$ and then estimating the remote-sensing reflectivity, which may, to a certain extent, remove the uncertainty resulted from environmental changes.

Furthermore, there exists the following simple relationship between $r_{rs}(\lambda)$ and the natural optical parameters:

$$r_{rs}(\lambda) = C\frac{b_b(\lambda)}{a(\lambda)+b_b(\lambda)} \tag{10}$$

Where, $b_b(\lambda)$ is the back scattering coefficient of the water body; $a(\lambda)$ is the absorption coefficient; C can be approximated to be an empirical constant. It can thus be seen that $r_{rs}(\lambda)$ has some natural

optical characteristics of the water body.

It can be seen from the application results of optical profile data processing in the test during the cruise No. 200304 in the Yellow Sea and the East China Sea that the relative deviation of repetitions $r_{rs}(\lambda)$ in one station can be controlled within 10 %, which reflects the good application results of this method.

This method still supposes that the upper water body is optically uniform. It can be seen from the analysis of the *in situ* test data in the China's coastal waters that, although the upper water body at each test station varies in the extent of optical uniformity and depth, this supposition is basically valid. The uncertainties in the optical uniformity of the water body, the wave effect and the synchronous measurement of $E_d(\lambda,Z)$ and $L_u(\lambda,Z)$ may all increase the uncertainty in using this method to estimate $r_{rs}(\lambda)$.

Another uncertainty in using this method to estimate $R_{rs}(\lambda)$ is the relationship between $r_{rs}(\lambda)$ and $R_{rs}(\lambda)$. It can be seen from (7) that when passing through the air-see interface, $r_{rs}(\lambda)$ is subject to the effect of a number of factors and these parameters are of a regional character in the China's coastal waters, for which further research is needed. Therefore, the application of the research findings of Lee (2002) to the calculations of $R_{rs}(\lambda)$ may have some uncertainty for the experimental sea area concerned.

Acknowledgements

We hereby thank the field scientific and technological researchers of the cruise No. 200304, especially the *in situ* testing personnel of the optical profiler for their hard work and the good data they provided.

References

[1] Fargion G S and Mueller J L. Ocean Optics Protocols for Satellite Ocean Color Sensor Validation . Revision 2, NASA/TM-2000-209966, 2000.

[2] Mueller J L and Fargion G S. Ocean Optics Protocols for Satellite Ocean Color Sensor Validation , Revision 3, NASA/TM-2002-210004, 2002.

[3] Mueller J L, Fargion G S and McClain C R. Ocean Optics Protocols for Satellite Ocean Color Sensor Validation , Revision 4, NASA/TM-2003-211621, 2003.

[4] Chen Qinglian,Tang Junwu, Li Tongji et al. Plan Research on the Plausibility Test of Space Remote-Sensing Data. *Technical Documents of the General Department of Equipment* (Restricted materials), 1999.

[5] Morel A Y and L Prieur. Analysis of variations in ocean color,*Limnol. Oceanogr.*, 1997, 22, 709B722.

[6] Lee Z P , Carder K L and Mobley C D , et al. Hyperspectral remote sensing for shallow waters. I. A semianalytical model. *APPLIED OPTICS*, 1998, 37(27): 6 329-6 338.

[7] Lee Z P, Carder K L, and Arnone R A. Deriving inherent optical properties from water color:a multiband quasi-analytical algorithm for optically deep waters. *APPLIED OPTICS*, 2002: 41(27): 5 755-5 772.

A Preliminary Study on the Calculating Method for the Evolution of Siltation and Erosion of Tidal Flat Based on GIS

DU Jinglong (杜景龙)[1,2], GAO Ang (郜 昂)[2], YANG Shilun (杨世伦)[2],
ZHANG Wenxiang (张文祥)[2], ZHAO Huayun (赵华云)[2], LI Peng (李 鹏)[2]

1 *Department of Urban and Environment, University of Technology and Science of Suzhou, Suzhou* 215011, *Jiangsu, China*

2 *State Key Lab of Estuarine & Coastal Research, East China Normal University, Shanghai* 200062, *China*

Abstract The estuary and coast is an area where the land and the sea interact and a place in which human beings frequently move about so that understanding and controlling the change and development modes of the coastal landform plays a vital part in exploiting and protecting coastal resources. A model is the generalization and abstraction of objective things. This paper summarizes four methods for the landform development of the tidal shore and underwater delta, mainly discusses the model's structural elements, and presents their specific application on the basis of the authors' case study. With the application of the profile model, the dynamic change of coastal landform can be clearly seen by contrasting the different profiles of different years. Through the shrinking, expanding and transformation of the isobath, plane model is used to study the macro-change of the shoal and the coastal landform. Speed model is an efficient means to analyze the trend of erosion and deposition and the local change in a great area of the sea. Statistical survey model is a static analysis, which can be used to establish the relationship between the erosion and deposition of the shoal and the altitude and slope of survey spot.

Keywords profile model, plane model, speed model, statistical survey model, Yangtze Estuary

1 Profile model

1.1 The process of building the model

Analysis of some representative profiles is an important technique to investigate the evolution of tidal flat. The dynamic change of the shoal can be understood by comparing and analyzing the profiles in different years. How to select the profile is very important because it influences the study greatly. Therefore, we should analyze and evaluate the study area seriously while assimilating others results of the scientific research to sort out the typical and representative profiles. The process of building a profile model is as follows:

Received on December 2, 2004

Superpose the representative profile line with the grid map of altitude, which is derived from the original topographic map, but the latter requires a special technique — interpolation. We can capture the altitude of the points along the profile line again by re-sampling the profile line. At the same time, we can also get the distance from any sample points to a baseline (such as bank) or the longitude and latitude of the sample points. The distance and the amount of the sample points can be selected freely because these have been done on the grid map of altitude. Finally, we export these data (altitude and the distance or longitude and latitude) to the statistical software such as Microsoft Excel and draw the profile map [1].

1.2 Application of the model

Fig. 1 shows a profile chart of three years east to Jiuduansha Tidal Island of the Yangtze River estuary. This chart shows the change of landform of the tidal shore and underwater delta as well as the difference of siltation and erosion in space-time. As shown in Fig. 1, the profile had accumulated strongly from 1958 to 1978, but the rate of accretion had lowered during the following two decades. The difference is to answer the decrease of sediment supply and SSC of Yangtze River. Both sediment supply and SSC of the Yangtze River significantly decreased from 1978 to 1998, compared with the 1958—1978 period. During the earlier 20 years (1958—1978), the mean annual sediment supply was 492 million tons and the mean SSC was 0.543 g/L; the mean accretion rate over the entire study area was 55 mm/a. From 1978 to 1998, however, the mean annual sediment supply declined to 409 million tons and the mean SSC decreased to 0.450 g/L. As a result, the mean accretion rate had decreased to only 11 mm/a. Fig.1 is a typical example showing large changes in the development of the cross-shore profile between the two periods. In the latter period, accretion was greatly reduced and erosion occurred in the lower reaches of the profile [2].

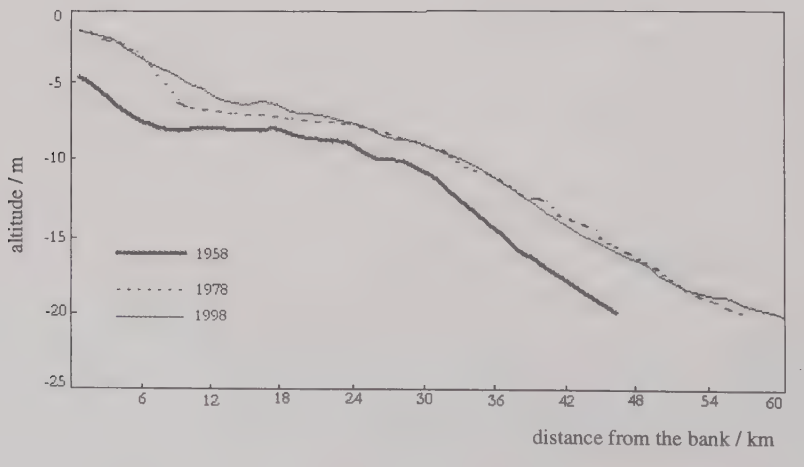

Fig. 1 Change in a representative cross-shore profile, showing uniform rapid accretion in the former 20 years and much less net accretion in the latter period

2 Plane model

2.1 The logical structure of models

The profile model is the typical imitation of the underwater bank and slope and illustrates the vertical change of the coastal landform, while the plane model investigates the horizontal change of the tidal shore and underwater delta and its dynamic siltation and erosion by shrinking, expanding and shape change of isobath. The key to building a plane model is to draw the isoline map, which can be created from the original topographic map by using two techniques: interpolation and classification. The former converts the discrete points to the grid map; the latter classifies the grid maps into different grades and the boundary between the two grades can be seen as isobath[3]. Fig.2 shows the process of building the plane model.

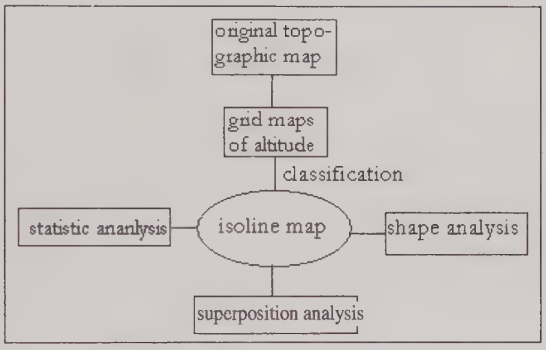

Fig. 2 Data flow chart of plane model

Information related to the change of physiognomy can be found from isobath. The area of the sea in different depths can be calculated and the intensity and scope of siltation and erosion can be ascertained. For example, the advance and retreat of 0 m and -6 m isobaths mean the accretion and erosion of tidal shoal and wetland; we can simulate the evolvement of the tidal shore and underwater delta by superposing their isobaths of different years; the shape change of isobaths often means the change of momentum of the sea and the change of riverine sediment. GIS software is the best technique to create an isobath and study it. On the other hand, the method of interpolation and classification influences the result greatly.

2.2 Application of the model

Jiuduansha tidal island took form in the 1950s. The area above 0 m is about 150 km^2 in 2004. We can investigate its development and growth by plane model. As shown in Fig. 3 to Fig. 6, we select four typical data in different years to study the change of *Jiuduansha* tidal island.

At the beginning of its birth, the shape of *Jiuduansha* tidal island was very irregular with an acuate head and two flood tide channels like fingers at its tail (-5 m isobath). In these years, *Jiuduans*

ha has been composed of three shoals above 0 m isobath, which are *Shangsha, Zhongsha and Xiasha. Shangsha* is close to *Zhongsha* and W-E alignment. *Xiasha* lies in the southeast[4].. The -2 m isobath of *Jiuduansha* tidal island is a close and continuous arc (Fig. 3).

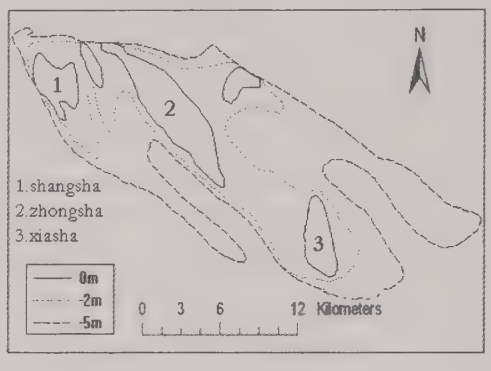

Fig.3 *Jiuduansha* tidal island in 1961

In the 1970s, the shape and position of *Jiuduansha* tidal island leveled off. But the area of the shoal above the 0 m isobath increased rapidly. The area doubled from 36.32 km^2 in 1961 to 75.6 km^2 in 1978. *Zhongsha* and *Xiasha* had joined together and there was only a cabined tidal channel beween *Shangsha* and *Zhongxiasha* (Fig. 4). At the same time, the -5 m isobath grew up with additional 2.2 km length, 0.5 km width and 50 km^2 area. The two flood tide channels like fingers disappeared too.

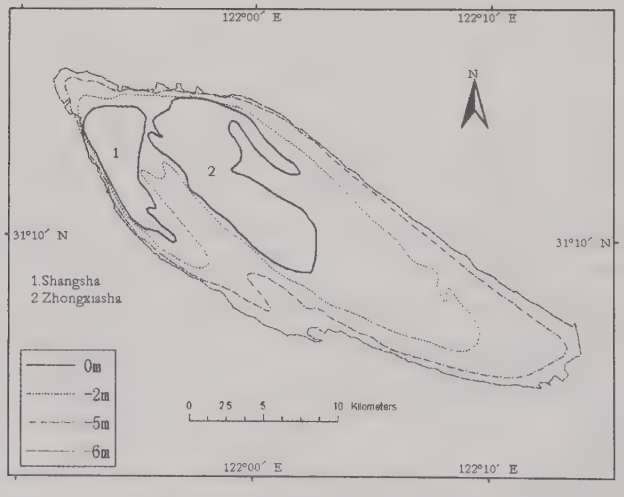

Fig. 4 *Jiuduansha* tidal island in 1978

From 1986 to 1992, *Jiangyanansha* shoal was incised from nanhuidong shore and immerged into head of *Jiuduansha* tidal island, which made the length and shape of *Jiuduansha* tidal island transform sharply: the length of 5 m isobath increased 14 km (36.2 km in 1989, 50.2 km in 1992) and

the shunt jaws of the south passage and north passage moved up about 10 km. The bottom of the *Jiuduansha* tidal island transformed little except the width expanding a little (about 200 m). (Fig.5)

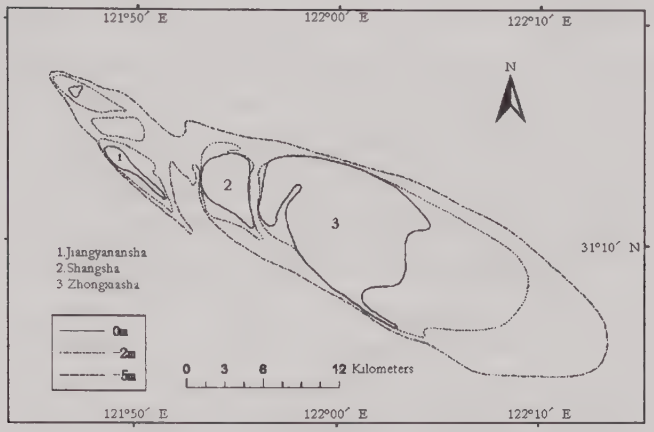

Fig. 5 *Jiuduansha* tidal island in 1995

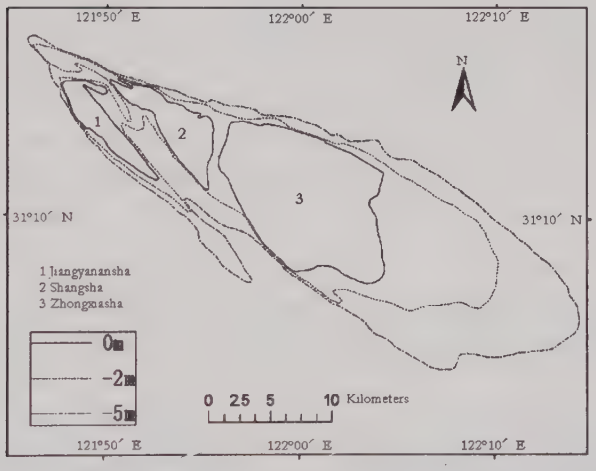

Fig. 6 *Jiuduansha* tidal island in 2004

Compared with that of 1995, the outline of the top part of *Jiuduansha* tidal island changed greatly in 2004: the expanding of *Jiangyanansha* shoal and the advancing to the west of *Shangsha* narrowed the tidal channel between them. The -5m isobath moved back to the south and the -2m isobaths had joined together. The S-N channel lying between *Shangsha* and *Zhongxiasha*, which had ever been the main passage of water and sediment between South Passage and North Passage, has accumulated greatly since 1995: the mean depth was 3.89 m in 1995, and 1.68 m in 2004 (Fig. 6). As Fig.6 shows, the shape of *Zhongxiasha* has transformed a little. Due to the Deep-Water Channel Project at North Passage of the Yangtse River, great change has occurred on the top part of *Jiuduansha* tidal island.

3 Speed model

3.1 The process of building the model

Speed model grades the study area into some patches according to the speed of siltation and erosion and then displays them in different colors or symbols. The magnitude of the speed reflects the vertical change of landform / siltation and erosion. The spatial distribution of different speeds reflects the horizontal change of landform / siltation and erosion. The contrast of speed models in different years reflects the change in intensity and modes of siltation and erosion.

Surfer software is a tool commonly used to create a speed model. The following illustrates how to build the model:

(1) Process the original topographic map and extract the longitude and latitude of the points in the Mapinfo software;

(2) Export the data in format of 'text' from the Mapinfo software, and then import these data into the Surfer software to create a 'grid file';

(3) Algebra operation. This operation is done in the Microsoft Excel software: Import the grid file of two different years into the Microsoft Excel software, arrange these data in the Microsoft Excel software, such as field 'A' and 'B' for longitude and latitude, field 'C' and 'D' for the altitude of same point in two years, field E the value of speed (E = (D-C) / t , 't' for the time interval of two years).

(4) Import the data composed of fields 'A', 'B', 'E' into Surfer and create a new 'grid file'. This file is a graphic file which depicts the distribution of speed of siltation and erosion .

(5) Create an isoline map by grading the graphic file and then displays it in different colors or symbols.

3.2 Application of the model

Fig.7 is two-years speed models of a large sea area at the Yangtze River estuary. Several conclusions could be drawn from the distribution of siltation and erosion in Fig.7[5]:

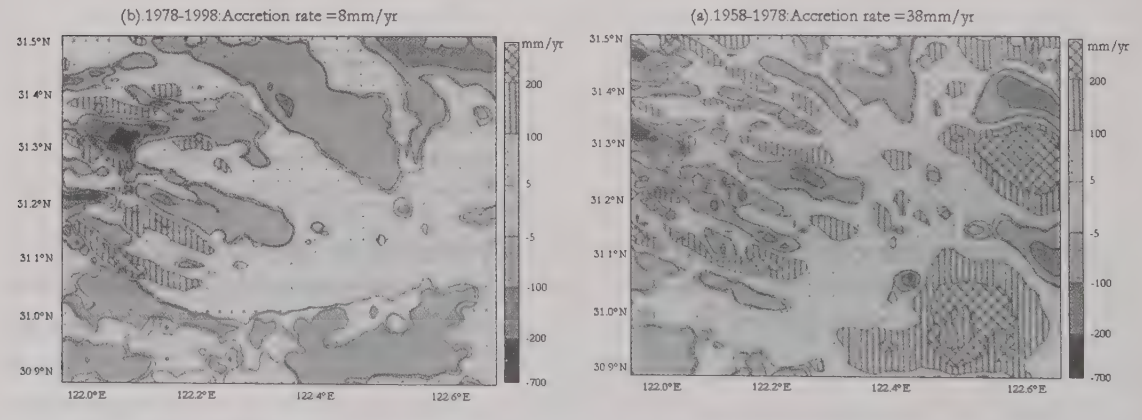

Fig. 7 Comparison of accretion and erosion (negative) between 1958—1978(a) and 1978—1998(b), showing an increase in erosion area and a sharp decrease in net accretion rate during the later period

(1) In the former period, 1958—1978, elongated erosion patches were typical of the northwest part of the study area, the upstream reaches of the subaqueous delta (Fig 7. a). The SE-NW alignment of these patches is similar to the orientation of the river outlets .These eroded troughs formed either due to a lateral shift of the outlets or due to the growth of tidal channels that cut into the shoals. On the bathymetric map surveyed in 1978 several tidal flood channels extended to NW. This orientation was governed by the direction of the flood currents. Another cause of the formation of eroded troughs is the deepening of the outlet beds between 1958 and 1978. It is likely that the patches like erosion in 1958—1978 were caused by water dynamics rather than by changes in sediment supply.

(2) Between 1978 and 1998, the erosion patches grew or merged (Fig.7a versus b), likely owing to the decline in river sediment load that reduced accretion and contributed to the delta erosion.

(3) The increase in erosion area from 1978 to 1998 has occurred mainly in the outer subaqueous delta.

From 1958—1978 to 1978—1998,the erosion area increased from 14 % to 38 % in the outer subaqueous delta of the study region while it increased from 30 % to 36 % in the inner subaqueous delta. Meanwhile, the net accretion rate decreased from 51 mm/a to 2 mm/a in the outer subaqueous delta while it decreased from 25 mm/a to 14 mm/a in the inner subaqueous delta. Thus, the outer subaqueous delta appeared more sensitive to changes in river sediment supply than the inner subaqueous delta. The outer subaqueous delta, therefore, is the vanguard when the delta advances or erodes. It is likely a universal law that the outer subaqueous delta would be the first to respond to a reduction in the river sediment supply.

4 Statistical survey model

4.1 The logical structure of this model

This method is a static model. It is often used to establish the relationship between the siltation and erosion and the altitude and slope of survey spot. As Fig. 8 shows, we can make grid maps of altitude and slope by the interpolation technique of Kriging. The grid map of the distribution of siltation and

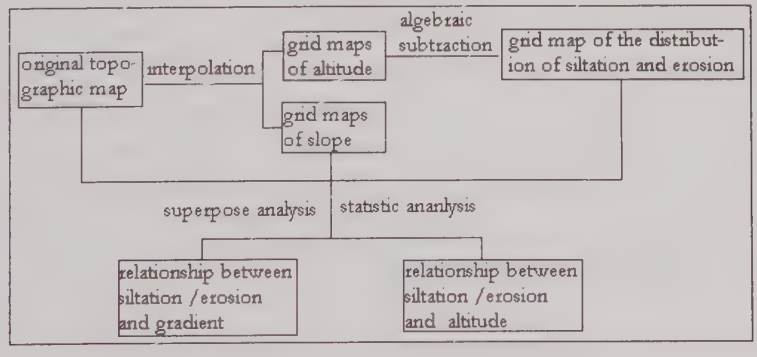

Fig. 8 Data flow chart of statistical survey model

erosion can be acquired by the subtraction operation of the grid maps of altitude in different years. Now, we have three maps: the grid map of the distribution of siltation and erosion, the grid maps of slope and the original topographic map. The quantity of siltation and erosion and the gradient at each survey spot can be obtained by superposing the three maps respectively. The statistical relationship can be established between the quantity of siltation and erosion and the altitude and gradient by importing these data into the statistical software[6].

4.2 Application of the model

Fig. 9 shows the relationship between the quantity of siltation and erosion and the altitude and slope of the survey spots near the Luchao Harbor[7]. As Fig. 9 shows, y-axis denotes the difference of altitude between 1990 and 1998. The positive value is siltation and the negative value is erosion. The horizontal line is the boundary of siltation and erosion. Those survey spots up the line accumulate and those below the line erode. x-axis denotes altitude (left Fig.) and slope (right Fig.).

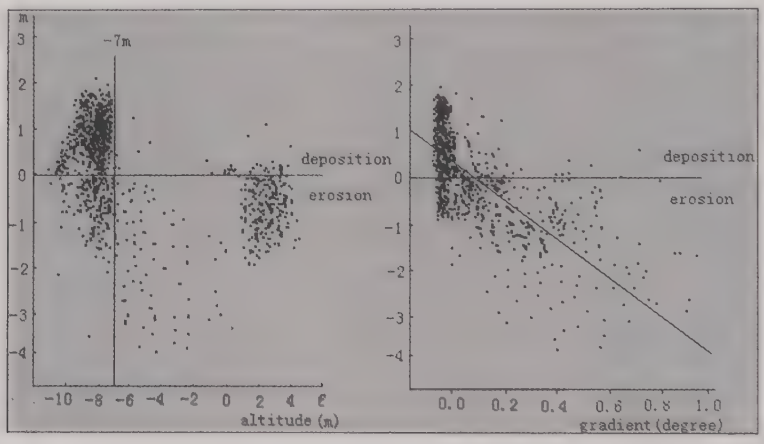

Fig. 9 Relationship between erosion-deposition and elevation-slope

We can see from Fig.9 that the area of accretion was very narrow and was mainly distributed in the deep-water zone (between -7 m and -9.5 m); the maximal accumulative thickness of accretion is about 1.8m. There also exists a small-scale accretion on the high tidal shore above the 0 m isobath, but the thickness of accretion is no more than 0.3m. The area of erosion is very large and the area at about -4 m depth is most intense; the maximal accumulative quantity of erosion reaches 4 m. As Fig. 9 shows, accumulation takes predominance, though erosion exists in the area at the more than -7 m depth. On the other hand, erosion dominates on the high tidal shore though accretion exists. As shown in Fig. 9 (right map), the area of accretion concentrates on the smooth shore whose gradient is no more than 0.1 degree. Erosion strengthens with the increase of the gradient.

5 Conclusion

The change of physiognomy of tidal shore is very complicated. The fixed change is foreseeable,

but the influence of some abrupt incidents such as typhoon, flood etc. may be more serious. The successive supervision and survey is the most important method to capture the data of tidal shore at all times, but the latter method and technique for research is important, too. The four kinds of models advanced in this paper study the change of landform of tidal shore in different aspects: the profile model mainly aims at the representative segments of the shore; the plane model can discover the shape change of shoals; the speed model can calculate the trend of siltation and erosion about large sea area; the statistical survey model is used to study the relationship between the siltation and erosion of the shore and the altitude and slope of survey spots. The model reflects the realities by data, so the validity, precision and effectivrness of the data are very important to the result.

Acknowledgements

This study was supported by the National Great Science Project (2002CB412407) and the National Science Foundation (40076027).

References

[1] WU Hualin, SHEN Huanting, HU Hui, et al. GIS supporting study on calculation of the amount of siltation and erosion in mouth bars of the changjiang Estuary. *Acta Oceanologica sinica*, 2002, 24(2): 126-132.

[2] LI Hengpeng, YANG Guishan. The Spatial Analysis of Erosion and Deposition of Tidal-flat by GIS. *Acta Geographica sinica*, 2001, 56(3).

[3] Li Hengpeng, Yang Guishan. Response of coast to sea-level rise: a review of study methods. *Advance in Earth Scinces*, 2000, 16(5): 598-603.

[4] Fan Shenjun,Yu Zhiying. The dynamic process and erosion-deposition pattern of tidal flat: a case as Lianyungang tidal flat. *Acta Oceanologica sinica*, 1997, 19(3): 67-85.

[5] Yang Shilun, Ding Pingxing, Chen Shenliang. Changes in progradation rate of the tidal flats at mouth of the Changjiang (Yangtze) River, China. *Geomorphology*, 2001, 38: 167-180.

[6] Yang Shilun, Zhao Qingying, Belkin Igor M. Temporal variation in the sediment load of the Yangtze river and the influences of human activities. *Journal of Hydrology*, 263(2002): 56-71.

[7] Yang S L, Belkin I M, Belkina A I, et al. Delta response to decline in sediment supply from the Yangtze River:. evidence of the recent four decades and expectations for the next half-century. *Estuarine, Coastal and Shelf Science*, 2003, 57: 689-699.

Temperature Tolerance of Large Yellow Croaker, *Pseudosciaena Crocea* (Richardson) Associated with Summer Season

CHEN Quanzhen (陈全震)[1,3], ZENG Jiangning (曾江宁)[1,2,3], LIAO Yibo (廖一波)[1,3], GAO Aigen (高爱根)[1,3], YANG Hefu (杨和福)[1]

1 *Second Institute of Oceanography, State Oceanic Adminstration, Hangzhou* 310012, *Zhejiang, China*

2 *College of Environmental and Resource Science, Zhejiang University, Hangzhou* 310029, *Zhejiang, China*

3 *Key Laboratory of Marine and Estuarine Fisheries,Ministry of Agriculture, Shanghai* 200090, *China*

Abstract Lethal temperature tolerance was determined for about 8 cm, age 0 *Pseudosciaena crocea* using both slow heating and rapid transfer protocol. The acclimatization temperature was 28 ℃ with summer season, lethal temperature (LT_{50} value) of slow heating protocol (CTMax) was 35.0 ℃, and the upper and lower incipient lethal temperatures of rapid transfer protocol were 34.2 ℃ and 17.5 ℃ respectively.

Keywords Large yellow croaker, *Pseudosciaena crocea*, Temperature tolerance, Critical thermal maximum, Thermally heated cooling water

Introduction

Temperature is an important environmental factor that determines the limit for life, affects the growth and metabolic rate, and influences the activity of organisms[1]. Assessment of lethal temperatures in fishes has been the subject of considerable research effort[2-8]. Brown[9] reviewed the method used by investigators to study thermal tolerance. Two normal methods were used, namely: (1) transferring suddenly of organisms from acclimation temperature into test temperature and recording the time until death over a designated period of time; (2) heating organisms at a standard rate such as 1 ℃ • h^{-1} until death occurs. Kilgour and McCauley[10] reviewed their two approaches and concluded that both types of data were useful. And McCullough[11] found that the heating rates of CTMax for various salmonids were 0.04℃ - 60 ℃ • h^{-1} in the previous work.

Temperature change of seawater is very common while the wastewater discharges from thermal power plants into estuarine and coastal waters. Discharged effluent waters are some 8 ℃ - 12 ℃ warmer than the intake temperatures at the directly cooled power stations in the temperate zones[1]. Generally, a 2000 M W power station utilizes some 50 m^3 • s^{-1} of seawater as cooling water, and the heat flow to the cooling water represents 50 % - 60 % of the energy produced from the fuel (fossil fuels or a nuclear reactor).

With the rapid development of economy and the successive drought in China, two thirds of the country is experiencing the most serious power shortage in a decade, especially in the eastern and

Received on October, 12, 2004

southern parts of China. To narrow the gap between the demand and supply of electricity, the government and many enterprises will invest an enormous sum of money to build many power plants on the coast of the southeastern China. However, the areas in which the building plants locate are places where the local people do marine breeding. Then their thermal effluents will affect the breeding *P. crocea* (Richardson), which production ranked the first in the year 2000, and was 1.0×10^8 kg. As an important marine economic fish in China, *P. crocea* distributes mainly in the Yellow Sea and the Bohai Sea of China (water temperature 10 ℃ - 28 ℃).

The purpose of this work is to ascertain the lethal incipient temperature and the CTMax by means of studying the thermal tolerance of *P. crocea*. This research for *P. crocea* will be more useful for the culturists and to those responsible for formulating regulations for thermal power plants.

1 Materials and methods

The fish were obtained from aquiculture farming facility in spring 2003, cultured in the locality of Shacheng harbor (Lat. 27° 10′ N; Long. 120° 20′ E) in Fujian Province, China, and maintained in different fishing cages (size 3 m× 3 m× 3 m) at the site temperature (28 ℃ ± 0.1 ℃).

In the laboratory, the fish were held in 1.5 m3 concrete tanks with a continual water flow at the site temperature (28 ℃ ± 0.1 ℃) , and fed with commercial balanced dry pellets. Food was withheld for 72 h before testing.

In slow-heating experiments, 20 individuals were transferred from holding tanks at 28℃ to a clean plastic container (50l capacity), filled with filtered aerated sea water. The tested fish (N = 140) were exposed to seven temperatures [(30, 31, 32, 33, 34, 35, 36℃) × 0.1 ℃] by adjusting temperatures gradually at a constant of 1 ℃ • d^{-1}, which was slow enough not to induce a heat shock response. The control fish (N = 20) remained at 28 ℃ in individual containers. A 300W submersible contact type thermometer thermostat was used to maintain the temperature of the water bath with an accuracy of ± 0.1 ℃ at the desired levels above the ambient temperature.

In each rapid transfer test, 20 fish were transferred (N = 60) from holding tanks at 28 ℃ into a clean plastic container (50 l capacity). Temperatures of UILT tests in each container were adjusted in advance to the desired test temperature [(33, 34, 35 ℃) ± 0.1 ℃] and maintained by a 300 W submersible contact type thermometer thermostat.

While temperatures of LILT tests in each insulated Styrofoam coolers were adjusted in advance to the desired test temperature [(20, 18, 15, 10 ℃) ± 0.5 ℃] by the ice-bag and measured every 2 h, continuous aeration was provided during each test to maintain adequate dissolved oxygen levels and to prevent thermal stratification in all testes. Test containers remained covered and darkness was maintained except for observation of fish response to testing.

The higher incipient lethal temperature (UILT) was rapidly transferred from 28 ℃ to 33 ℃, 34 ℃ and 35 ℃in turn, and the lower incipient lethal temperature (LILT) was rapidly transfered from 28 ℃ to 18 ℃, 15 ℃, 10 ℃ in turn.

The same experiment was repeated two times for each temperature. Altogether 600 fishes were used for the mortality experiments [(2 × (1 control test + 7 slow-heating tests +3 high-temperature rapid transfer tests + 4 low-temperature rapid transfer tests) × (20 fishes in each experiment) = 600 fishes].

The CTMax and CTMin were introduced by Cowles and Boggert[2], modified by Lowe and Vance [12] and standardized by Hutchison[13]. Cox[14] defined these tolerance measurements as the arithmetic mean of the thermal points in which the locomotive activity becomes disorganized and the organism loses its ability to escape the conditions that would result in death. In this trial, time to death was recorded for each individual, and again mortality was defined as the cessation of opercular movement [15]. Total length of each individual fish was measured to the nearest mm and the weight of each fish was measured to the nearest 0.01 g.

In order to determine the incipient lethal temperature, the fish previously acclimated were transferred abruptly to a high or low constant temperature. The upper incipient lethal temperature (UILT) was studied according to the procedure of Wedemeyer and McLeay[16].

The differences of repeating groups were compared by Students*t*-tests. All statistical significance tests were at the $P < 0.05$ level. LT_{50} for CTMax, UILT and LILT of the fish was calculated by the one-dimensional linear regression method. The significance of regression curves was examined by *F*-test.

2 Results

2.1 Slow heating (Critical Thermal Maximum)

Slow-heating tests were conducted at eight different temperatures of 28, 30, 31, 32, 33, 34, 35, 36 ℃ (Table 1). In the test, mortalities occurred over a narrow range of 33 ℃ - 36 ℃ , and the

Tab.1 Tests of critical thermal maxima for *P. crocea*

Exposure temperature / ℃	28			30			31			32			33			34			35			36		
No.of fish in treatment	20			20			20			20			20			20			20			20		
Average weight / (g±S.D)	5.8±1.7			6.0±2.1			5.8±1.5			5.7±1.4			5.9±2.2			5.5±1.3			5.5±1.5			5.7±2.1		
Average length / (cm±S.D)	8.1±0.9			8.1±1.2			8.1±0.8			8.1±0.8			8.1±1.2			8.0±0.7			7.9±0.9			8.3±1.3		
Group	I	II	*m*	I	II	*m*	I	II	*m*	I	II	*m*	I	II	*m*	I	II	*m*	I	II	*m*	I	II	*m*
No.of mortality fish during 0.8 h	0	0	0	0	0	0	0	0	0	0	0	0	0	0	0	0	0	0	0	0	0	1	1	1
No.of mortality fish during 1 h	0	0	0	0	0	0	0	0	0	0	0	0	0	0	0	0	0	0	0	0	0	2	3	3
No.of mortality fish during 2 h	0	0	0	0	0	0	0	0	0	0	0	0	0	0	0	0	0	0	0	0	0	17	17	17
No.of mortality fish during 3 h	0	0	0	0	0	0	0	0	0	0	0	0	0	0	0	0	0	0	0	0	0	18	19	19
No.of mortality fish during 4 h	0	0	0	0	0	0	0	0	0	0	0	0	0	0	0	0	0	0	0	0	0	20	20	20
No.of mortality fish during 5 h	0	0	0	0	0	0	0	0	0	0	0	0	0	0	0	0	0	0	2	2	2	—	—	—
No.of mortality fish during 7 h	0	0	0	0	0	0	0	0	0	0	0	0	0	0	0	0	0	0	3	3	3	—	—	—
No.of mortality fish during 12 h	0	0	0	0	0	0	0	0	0	0	0	0	0	0	0	0	0	0	4	4	4	—	—	—
No.of mortality fish during 24 h	0	0	0	0	0	0	0	0	0	0	0	0	0	0	0	0	0	0	10	10	10	—	—	—
No.of mortality fish during 48 h	0	0	0	0	0	0	0	0	0	0	0	0	1	1	1	1	2	2	13	14	14	—	—	—
No.of mortality fish during 72 h	0	0	0	0	0	0	0	0	0	0	0	0	1	1	1	2	2	2	14	14	14	—	—	—

Note: *m*: means.

If means of two groups experiments have decimal fraction, round off to integer.

temperatures resulted in 100 % mortality occurring at higher temperature (35, 36 ℃). 50 % of mortality occurred in 35 ℃ during 24 h (Fig.1).

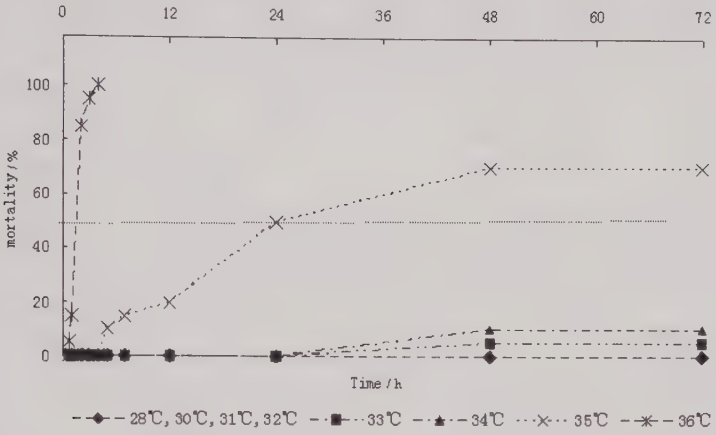

Fig.1 Mortality of *P. crocea* in different groups during 72 h

2.2 Rapid transfer test

2.2.1 Test of the upper incipient lethal temperature (UILT)

The UILT of *P. crocea* was obtained from the lethal temperature in which 50 % mortality occurred. Tests of UILT were conducted at three different temperatures of 33, 34, 35 ℃ (Table 2). In the test, mortalities occurred over a narrow range of 34 ℃ - 35 ℃, whereas the temperature resulted in 100 % mortality occurring at the higher one (35℃).

Tab.2 Results of rapid-transfer upper temperature thermal tolerance tests on *P. crocea* acclimated at 28 ℃

	28 ℃→33 ℃			28 ℃→34 ℃			28 ℃→35 ℃		
No.of fish in treatment	20			20			20		
Average weight (g)	4.3±1.4			4.8±1.6			6.2±2.6		
Average length (cm)	7.6±1.2			7.6±0.9			8.3±1.3		
Group	I	II	*m*	I	II	*m*	I	II	*m*
No.of mortality during 1 h	0	0	0	0	0	0	16	15	16
No.of mortality during 2 h	0	0	0	0	0	0	20	20	20
No.of mortality during 6 h	0	0	0	0	0	0	—	—	—
No.of mortality during 12 h	0	0	0	4	4	4	—	—	—
No.of mortality during 24 h	0	0	0	4	4	4	—	—	—

2.2.2 Test of the lower incipient lethal temperature (LILT)

The LILT of *P. crocea* was obtained from the lethal temperature in which 50 % mortality occurred. Tests of LILT were conducted at four different temperatures of 20, 18, 15, 10 ℃ (Table 3).

In the test, 100 % mortality in 24 h occurred over a narrow range of 15 ℃ - 10 ℃.

Tab.3 Results of rapid-transfer lower temperature thermal tolerance tests on *P. crocea* acclimated at 28 ℃

	28 ℃→20 ℃			28 ℃→18 ℃			28 ℃→15 ℃			28 ℃→10 ℃		
No.of fish in treatment	20			20			20			20		
Average weight(g)	7.1±2.4			6.7±2.5			6.3±1.3			7.1±2.0		
Average length(cm)	8.6±1.1			8.4±1.1			8.4±0.8			8.7±0.8		
Group	I	II	*m*	I	II	*m*	I	II	*m*	I	II	*m*
No.of mortality during 0.2 h	0	0	0	0	0	0	0	0	0	20	20	20
No.of mortality during 2 h	0	0	0	0	0	0	2	2	2	—	—	—
No.of mortality during 6 h	0	0	0	0	0	0	14	14	14	—	—	—
No.of mortality during 12 h	0	0	0	0	0	0	20	20	20	—	—	—
No.of mortality during 24 h	0	0	0	6	5	6	—	—	—	—	—	—

2.3. Fitting curves to data

Based on the results of Table 2 and Table 3, fitting curves of CTMax, UILT and LILT were shown in Table 4.

Tab.4 Data equation fitness corresponds to *P. crocea* of the critical thermal maximum (CTMax) and upper (UILT) and lower (LILT) incipient lethal temperature acclimated during 24 h at the temperature of 28 ℃

Response	Equation	Groups of regression data *(n)*	Correlation coefficient *(r)*	Temperature for 50 % of mortality (LT50) / ℃	fiducial probability *(p)*
CTMax	Y = 0.5 x−17.0	3	1.00	35.0	0.99
UILT	Y = 0.5 x−16.6	3	0.94	34.2	0.99
LILT	Y = −0.2 x + 4.0	3	0.99	17.5	0.90

Note: F0.10(1,1)=6.314, F0.01(1,1)=161.4

Y-mortality (0-1), X-temperature (℃)

3 Discussion

The responses to lethal and critical temperatures, the capacity of animals to acclimate to different thermal regimes differ between species[17-19]. Some differences in the CTMax are associated with the latitudinal and geographical distribution limits, as well as the native habitat temperatures of the organisms [20]. Furthermore, fish acclimatization to low temperatures is more tolerant to cold and more sensitive to heat than fish acclimatization to warm temperatures[21, 22]. On the other hand, the organisms acclimated to high temperatures are the most sensitive to cold and the most tolerant to heat[23]. We observed a similar behavior when *P. crocea* was acclimated at 28 ℃.

From Fig.1 it can be seen that the test time lasted 72 h, but the 50 % mortality of the fish in all tests

was shorter than 24 h. This is the reason why the CTMax tests of fish were adopted during 24 h in the tests.

Reynolds and Casterlin[24] identified CTMax as a measure of the upper limit of the resistance zone. However, CTMax for a species is not fixed and may depend on season, gender and individual genetic variability [25]. The experiments were carried out during Aug., 2003, which was one of the hottest years of China. Therefore, the result of the tests in the summer season was more significative.

The previous researches indicated that the heating rates of CTMax of various fish were not uniform, which ranged from 0.04 to 60 ℃ • h^{-1} (Table 5) .

Tab. 5 Heating rate in the CTMax test for various fishes in the previous work

Species	Origin	Acclimatiz-ation Temp / ℃	Heating Rate / ℃ • h^{-1}	CTM / ℃	References
Ambasis commersoni	Vellar estuary, India	28±1	60	40.50	[26]
Clupea pallasi	Coastal waters, Japan	20	5	29±0.1	[27]
Engraulis Japonica	Coastal waters, Japan	28	5	34.9±0.3	[27]
Etroplus suratensis	Vellar estuary, India	28±1	60	42.25	[26]
Lates calcarifer	Vellar estuary, India	28±1	60	44.50	[26]
Liza dussumeri	Vellar estuary, India	28±1	60	44.50	[26]
Macrobrachium tenellum	Mulegé , Mexico	28	60	40±0.4	[7]
Moxostoma erythrurum	Walhonding River, OH, USA	21.1	4.8	35.4	[28]
Moxostoma macrolepidotum	Walhonding River, OH, USA	19.9	3.4	35.1	[28]
Oncorhynchus keta	Coastal waters, Japan	20	5	29.9±0.3	[27]
Oncorhynchus kisutch	Bingham Cr., WA, USA Bockman Cr., WA, USA Snow Cr., WA, USA	11.5 16.6 14.6	20 20 20	28.2 29.1 29.2	[29, 30]
Oncorhynchus mykiss	n. r.; (2-3 months old)	17	0.04-0.08	26.3	[31]
Oncorhynchus mykiss	USFWS Williams Cr. NFH, Arizona, US	20	1.2	29.35±0.58	[32]
Poecilia sphenops	Piedra Azul Dam, Mexico	29	60	41.8	[8]
Pseudocaranx dentex	Coastal water , Japan	29	5	36.3±0.1	[27]
Salmo apache	Arizona, US	15.6	0.04-0.06	21.2-22.3	[33]
Salmo salar	Atlantic salmon age 0+ and 1+ combined	20	0.01 1.0 18	27.74±1.20 32.63±0.38 32.83±0.83	[34]
Salmo salar	n.r.; (2-3 mo.)	17	0.04-0.08	28.7-29.2	[31]
Sardinops melanostictus	Coastal water, Japan	28	5	33.9±0.2	[27]
Scatophagus orgus	Vellar estuary, India	28±1	60	42.50	[26]
Seriola quinqueradiata	Coastal water, Japan	28	5	36.9±0.1	[27]
Siganus javus	Vellar estuary, India	28±1	60	39.50	[26]
Therapon jarbua	Vellar estuary, India	28±1	60	42.00	[26]
Trachurus japonicus	Coastal water, Japan	28	5	35.4±0.2	[27]

Note: n.r.—origin of test fish "not reported"

The upper and lower thermal limits that fish can resist define the tolerable ends of the thermal environment [35, 36]. These temperature limits are subject to change through acclimation. It is important to highlight that the interval of acclimation used depends on the distribution limits of the species or the temperature fluctuations in their habitat. *P. crocea* shows a similar behavior. For instance, while at the same high temperature, such as 34 ℃, the survival time is different in slow heating protocol and rapid transfer protocol, all the tested individuals survived in the former and 16 individuals survived in the latter.

The thermal tolerance area of the fish has a practical value in the selection of available places for cultivation [37]. The knowledge of the thermal tolerance and resistance of the organisms could be used to assess the risks of mortality in culture systems with daily and annual temperature fluctuations[8], and could forecast survival of or damage to cultured *P. crocea* exposed to the cooling water of these electrical power plants.

Acknowledgements

The authors would like to thank Mr. Sun Qinghai for technical assistance and providing experimental facilities, to Mr. Alan Desbonnet for good advices on the paper. This study was supported by the Science and Technology Bureau of Zhejiang Province (No.2003C33064), and the Science and Technology Bureau of Ningbo City (No.2003C10002), and the Key Laboratory of Marine and Estuarine Fisheries of the Ministry of Agriculture.

References

[1] Bamber R N. The influence of rising background temperature on the effects of marine thermal effluents. *J. Therm. Biol.*, 1995, 20, 105-110.

[2] Cowles R B, Bogert C M. A preliminary study of the thermal requirements of desert reptiles. *Bull. Am. Mus. Nat. Hist.*, 1944, 83, 265-296.

[3] Fry F E J. Effects of the environment on animal activity. University of Toronto Studies in Biology Series 55. *Publ. Ontario Fish. Res. Lab.*, 1947, 68, 5-62.

[4] Elliott J M. Some aspects of thermal stress on freshwater teleosts. In: Pickering, A.D. (eds.), *Stress and Fish*, Academic Press, London, 1981, 209-243.

[5] IMO/FAO/UNESCO/WMO/WHO/IAEA/UN/UNEP Joint Group of Experts on the Scientific Aspects of Marine pollution (GESAMP). *Reports and studies- Thermal discharges in the marine environment.* Food and Agriculture organization of the United Nations. 1984, 24, 1-44.

[6] Barrionuevo W R, Fernandes M N. Critical thermal maxima and minima for curimbata, *Prochilodus scrofa* Steindachner, of two different sizes. *Aquaculture Res.*, 1995, 27, 447-450.

[7] Hernández R M, Bückle R L F, Díaz R H F. Critical Thermal maximum of *Macrobrachium tenellum*. *J. Therm. Biol.*, 1996, 21, 139-143.

[8] Hernández R M, Bückle R L F. Temperature tolerance polygon of*Poecilia sphenops* Valenciennes (Pisces: Poeciliidae). *J. Therm. Biol.*, 2002, 27, 1-5.

[9] Brown H W. *Handbook of the Effects of Temperature on Some North American Fishes.* Canton, OH:

American Electric Power Service Corporation, Environmental Engineering Division. 1976.

[10] Kilgour D M, McCauley R W. Reconciling the two methods of measuring upper lethal temperature in fishes. *Environ. Biol. Fish.*, 1986, 17, 281-290.

[11] McCullough D A. A REVIEW AND SYNTHESIS OF EFFECTS OF ALTERATIONS TO THE WATER TEMPERATURE REGIME ON FRESHWATER LIFE STAGES OF SALMONIDS, WITH SPECIAL REFERENCE TO CHINOOK SALMON. United States Environmental Protection Agency, EPA910-R-99-010, 1999, 54-55.

[12] Lowe C H, Vance J V. Acclimation of critical thermal maximum of the reptile *Urosaurus ornatus. Science*, 1955, 122, 7374.

[13] Hutchison V H. 1961. Critical thermal maxima in salamanders. *Physiol. Zool.*, 34, 92125

[14] Cox D K. Effects of the three heating rates on the critical thermal maximum of bluegill. In: Gibbons, J. W., Sharitz R. R. Editors, 1974. *Thermal Ecology AEC Symposium Series* (Conf-73055), Springfield, VA, 1974, 150163.

[15] Baker S C, Heidinger R C. Upper lethal temperature tolerance of fingerling black crappie. *J. Fish Biol.*, 1996, 48, 1 123-1 129.

[16] Wedemeyer G A, McLeay D J. Methods for determining the tolerance of fishes to environmental stressors. In: *A.D. Pickering (ed.). Stress and fish.* Academic Press, London. 1981, 247-275.

[17] Brett J R. Temperature tolerance in young Pacific salmon genus *Oncorhychus. J. Fish. Bd. Can.*, 1952, 9, 265-323.

[18] Otto R E. Temperature tolerance of mosquitofish Gambusia affinis (Baird & Girard). *J. Fish Biol.*, 1973, 5, 575-585.

[19] Rantin F T, Peterson J A. Thermal tolerance of South American cichlid, Geophagus brasiliensis. *Rev. Hydrobiol. Trop.*, 1985, 18, 221-226.

[20] McGeer J C, Baranyi L, Iwama G K. Physiological responses to challenge tests in six stocks of coho salmon (Oncorhynchus kisutch). *Can. J. Fish. Aquat. Sci.*, 1991, 48, 1 761-1 771.

[21] Elliott J A. A comparison of thermal polygons for British freshwater teleosts. *Freshwater Forum*, 1995, 5, 178-184.

[22] Sun Yongmei, Li Dongzhan, Hou Wenli. The study on the temperature-limiting values for young*Oncorhync hus masou* (Bervoore). *Songliao Journal (Natural Science Edition)*(in Chinese), 1999, 2, 48-50.

[23] Cai Zeping, Chen Haoru, Jin Qizeng et al. Influence of thermal power effluent on three species of fishes in Daya Bay. *Tropic Oceanology* (in Chinese), 1999, 18, 11-19.

[24] Reynolds W W, Casterlin M E. Behavioral thermoregulation and the final preferendum paradigma. *Am. Zool.*, 1979, 19, 211-224.

[25] Holland W E, Smith H, Gibbons J W et al. Thermal tolerances of fish from a reservoir receiving effluent from a nuclear reactor. *Physiol. zool.*, 1974, 47, 110-118.

[26] Rajaguru S. Critical thermal maximum of seven estuarine fishes. *J. Therm. Biol.*, 2002, 27, 125-128.

[27] Tsuchida S. The relationship between upper temperature tolerance and final preferendum of Japanese marine fish. *J. therm. Biol.*, 1995, 20, 35-41.

[28] Reash R J, Seegert G L, Goodfellow W L. Experimentally-derived upper thermal tolerances for redhorse suckers:revised 316(A) variancd conditions at two generating facilities in Ohio. *Environmental Science & Policy*, 2000, 3: 191-196.

[29] Konecki J T, Woody C A, Quinn T P. Thermal adaptations of Washington coho salmon (*Oncorhynchus kisutch*) populations: incubation, preference and tolerance. School of Fisheries, Center for Streamside Studies, University of Washington WH-10, Seattle, WA. 1993, 34 p.

[30] Konecki J T, Woody C A, Quinn T P. Critical thermal maxima of coho salmon (*Oncorhynchus kisutch*) fry under field and laboratory acclimation regimes. *Can. J. Zool.*, 1995, 73, 993-996.

[31] Grande M, Andersen S. Critical thermal maxima for young salmonids. *J. Freshwater Ecology,* 1991, 6, 275-279.

[32] Lee R M, Rinne J N. Critical thermal maxima of five trout species in the southwestern United States. *Trans. Am. Fish. Soc.,* 1980, 109, 632-635.

[33] Alcorn S R. Temperature tolerances and upper lethal limits of*Salmo apache. Trans. Am. Fish. Soc.,*1976, 105, 294-295.

[34] Elliott J M, Elliott J A. The effect of the rate of temperature increase on the critical thermal maximum for parr of Atlantic salmon and brown trout. *J. Fish Biol.,* 1995, 47, 917-919.

[35] Brett J R. Some principle in the thermal requirements of fishes. *Quart. Rev. Biol.*, 1956, 31, 75-87.

[36] Rajaguru S, Ramachandran S. Temperature tolerance of some estuarine fishes. *J. Therm. Biol.,* 2001, 26, 41-45.

[37] Lyytä ikinen T, Jobling M. The effects of temperature, temperature shift and temperature fluctuation on daily feed intake, growth and proximate composition of underyearling Lake Inari arctic charr (*Salvelinus alpinus*(L.)). *Nordic J. Freshwater Res.,* 1998, 74, 87-94.

Backward Calculation Based on the Advection and Diffusion of Oil Spills on the Sea Surface

LIU Hao (刘 浩)[1,2], YIN Baoshu (尹宝树)[1], LIN Jianguo (林建国)[3]

1 *Open Laboratory of Circulations and Waves, Institute of Oceanology, CAS, Qingdao* 266071, *Shandong, China*

2 *Graduate School, CAS, Beijing, 100039, China*

3 *College of Environmental Science and Engineering, Dalian Maritime University, Dalian* 116026, *Liaoning, China*

Abstract In the light of the problem of oil pollution brought about by ships, in this paper we present the concept of backward tracing oil spills. In the course of backward calculation of the two-dimensional convection & diffusion equation, on the one hand, the advection term itself has the strong unilateral property, which means information in the upper reaches is transmitted downstream via the advection term; on the other hand, because of the opposite direction of calculation, it is essential for information to be conveyed upstream by means of the advection term. In addition, unlike that in the forward calculation, the diffusion term in the backward calculation is prone to accumulate errors, and thus renders the whole scheme unstable. Therefore, we adopt the central difference to deal with both the convectional term and the diffusion term. By examining two practical examples (1) under the unlimited boundary condition, and (2) under the limited boundary condition, it is proven that this method could achieve fundamentally satisfactory results not only in the open ocean but also in the closed or semi-closed bay.

Keywords Backward calculation, advection-diffusion, numerical dissipation

Advection and diffusion equation is an effective means of investigating the motional state of oil spills. Common study is based on the known initial and boundary conditions to calculate the equation onwards. Unlike previous works, in this paper we focus on backward calculating advection and diffusion equation, namely, starting computation from the moment when the oil spill is found back to the moment when the incident occurs. Through such a simulation, we hope to trace the track of oil spills on the sea surface and, more importantly, obtain the solution pertaining to its initial state, whose physical implication is the initial concentration distribution of oil spills. Therefore, such a study is conducive to tracing the source of oil spills.

1 Numerical Model

1.1 Establishment of model

Received on May 7, 2004

When oil enters sea water, it will experience a series of physical and chemical changes: such as diffusion, evaporation, dissolution, oxidation, sedimentation, biodegradation, and so forth[1-3]. If we take all these factors into consideration, then the numerical model obviously is too complicated to establish. In order to simplify the model, we assume that the mass of oil spills is unchanged in the course of motion; what is more, it also does not affect sea water's properties[4]. In addition, based on the fact that the majority of oil floats on the surface, we decide to take the two dimensional advection and diffusion equation as the control equation, as follows:

$$\frac{\partial c}{\partial t}+\frac{\partial (uc)}{\partial x}+\frac{\partial (vc)}{\partial y}=\frac{\partial}{\partial x}(D_x\frac{\partial c}{\partial x})+\frac{\partial}{\partial y}(D_y\frac{\partial c}{\partial y}) \tag{1}$$

where: c is the concentration of oil spills; u, v, the x, y components of velocity, respectively; D_x, D_y, the diffusion coefficients of oil spills along x, y directions, respectively.

1.2 Choosing numerical scheme

The finite difference method is employed to disperse the above differential equation: forward difference scheme is applied to the time term, and the diffusion term adopts the central difference scheme in our study. Due to the strong directional property pertaining to the advection term, the upwind scheme is commonly used to guarantee the stability of onward calculation. Just as we have specified in the above section, our interest here is mainly concentrated on backward computation, so when dispersing the equation, we not only consider the impact of information transmitted from previous nodes (flow direction), but also notice the influence coming from posterior nodes (calculation direction)[5]. Based on such consideration, we apply the central differential scheme to the advection term. The numerical scheme we used in this study possesses two orders of precision, belonging to conditional stability.

2 Calculation and results

2.1 Case 1 — calculation within a rimmed domain

Study in this section mainly aims at such rimmed domains as closed or semi-closed ports, estuaries as well as bays. When an oil spill occurs near the shore, under the influence of currents, it will shift to the coastline and stay there, failing to move further; therefore, the coastline becomes the boundary condition for backward investigating advection and diffusion of oil spills.

We suppose its initial concentration is known, namely, the initial condition of the control equation is given, and then we could obtain analytic solution at any time, which will be regarded as the concentration at the moment when an oil spill is found; thus the initial condition for backward calculation is set up. By means of the numerical method chosen in the above section, we simulate backward, and the final numerical result is the concentration when the oil spill takes places. Comparing the numerical result and the initial condition we have given, we can examine the validity of our numerical scheme.

The given boundary and initial conditions are as follows:

$$c(0,y,t)=c(L_1,y,t)=0\ ,\quad c(x,0,t)=c(x,L_2,t)=0 \qquad \text{Boundary condition}$$

$$c(x,y,0)=c_0\sin\left(\frac{\pi x}{L_1}\right)\sin\left(\frac{\pi y}{L_2}\right)\exp\left(\frac{ux}{2D_x}+\frac{vy}{2D_y}\right) \qquad \text{Initial condition}$$

where L_1, L_2 are the non-dimensional length scales of computational domain along x, y directions, respectively, and equal to 1 in the following calculation.

The analytic solution of equation (1) is in the following form:

$$c(x,y,t)=c_0\exp\left(\frac{ux}{2D_x}+\frac{vy}{2D_y}-\left[\left(\frac{2D_x\pi}{L_1}\right)^2+u^2\right]t/(4D_x)-\left[\left(\frac{2D_y\pi}{L_2}\right)^2+v^2\right]t/(4D_y)\right)\sin\left(\frac{\pi x}{L_1}\right)\sin\left(\frac{\pi y}{L_2}\right) \quad (2)$$

The whole computational domain is divided into 10×10 square grids with a uniform grid spacing of 0.1 in both x and y directions. Based on the CFL stability condition, the time step is taken as 0.033 (non-dimensional) here; in addition, we suppose the total time of computation is 1, thus in order to obtain the final numerical solution, the calculation needs to run at least 30 time steps. Based on the above assumption, we examine the numerical results under different velocity and diffusion coefficients at the time of t = 0, and the mean error between computed results and supposed ones are in Table 1 where $\alpha_1=u\frac{\Delta t}{\Delta x}$, $\alpha_2=v\frac{\Delta t}{\Delta y}$, $\beta_1=D_x\frac{\Delta t}{\Delta x^2}$, $\beta_2=D_y\frac{\Delta t}{\Delta y^2}$, and *erf* is the mean error.

Tab. 1 Computed results under different conditions

u	v	D_x	D_y	α_1	α_2	β_1	β_2	*erf*
0.01	0.01	0.01	0.001	0.0033	0.0033	0.033	0.0033	1.13×10^{-2}
0.01	0.01	0.001	0.01	0.0033	0.0033	0.0033	0.033	1.15×10^{-2}
0.01	0.05	0.01	0.01	0.0033	0.0165	0.033	0.033	1.74×10^{-2}
0.05	0.01	0.01	0.01	0.0165	0.0033	0.033	0.033	7.62×10^{-2}
0.01	0.05	0.001	0.01	0.0033	0.0165	0.0033	0.033	2.34×10^{-2}
0.05	0.01	0.01	0.001	0.0165	0.0033	0.033	0.0033	2.28×10^{-2}
0.1	0.01	0.05	0.02	0.033	0.0033	0.165	0.066	5.37×10^{-2}
0.01	0.1	0.02	0.05	0.0033	0.033	0.066	0.165	8.26×10^{-2}

The two-dimensional advection diffusion equation belongs to parabolic type, and spatial variables x and y are symmetric; in other words, under the same condition they may have a similar effect on the equation [8]. However, Table 1 shows that when other factors keep constant, only by exchanging the values of u and v, or those of D_x and D_y, or the former and the latter simultaneously, can we obtain different results, or even distinct results in some cases. According to my knowledge, the comparatively less number of grids is not enough to eliminate the inequality coming from the technique by which we apply implicit scheme to two spatial variables alternately. Therefore, it is evident that increasing the number of grids can decrease such difference[9]. On the other hand, addition of grids may not be unlimited, and it is truer for backward calculation. We carry out some numerical experiments: the error as a whole is definitely being improved until the number of grids increases to 13×13, and increasing the number further, we find that the values at individual nodes begin to disperse, and, whats more, in conjunction with the increase of grid density, such a tendency becomes more obvious.

2.2 Case 2 — calculation within a brimless domain

2.2.1 Calculation aiming at a practical problem

The method used in this section of study is similar to that within a rimmed domain, but some differences must be stressed. Because the open marine space is our major object, the impact of boundary on oil spills is negligible here. Such assumption is suitable for the case that the incident occurs far from the shore.

The given initial condition is $c(x, y, o) = c_0 e^{-(k_1 x^2 + k_2 y^2)}$. Where $-\infty < x, y < \infty$, c_0, k_1, k_2 is constant, whats more, $k_1 > 0, k_2 > 0$; and the value here is set as $c_0 = 1, k_1 = 1, k_2 = 1$.

The analytic solution of Eq. (1) based on the above condition is

$$c(x, y, t) = \frac{c_0}{\sqrt{4D_x tk_1 + 1} \cdot \sqrt{4D_y tk_2 + 1}} \exp\left(- \frac{k_1 (x - ut)^2}{4D_x tk_1 + 1} - \frac{k_2 (y - vt)^2}{4D_y tk_2 + 1} \right) \quad (3)$$

We choose a square physical domain with the side length of 5 km, and 34×34 grids with an equivalent grid spacing of 147 m along both x and y directions are divided in it. The total time of calculation is 3 minutes and the time step is 3.6 s, and thus a total of 50 steps are needed to acquire the initial solution. Table 2 shows that the computed results are basically coincident with the given values.

Tab.2 Computed results under different speeds and diffusive coefficients

Velocity / m • s^{-1}		Diffusion coefficient / m^2 • s^{-1}		Mean error *(erf)*	
u	v	D_x	D_y	t = 0 (s)	t = 90 (s)
1.67	1.67	167	167	5.85×10^{-3}	1.74×10^{-3}
3.34	0.835	167	16.7	7.55×10^{-3}	1.62×10^{-3}
1.67	0.167	167	167	5.68×10^{-3}	1.74×10^{-3}
0.835	3.34	83.5	83.5	3.22×10^{-3}	1.29×10^{-3}
0.167	1.67	83.5	16.7	2.02×10^{-3}	1.22×10^{-3}

2.2.2 Treatment of numerical boundary

For the purpose of calculation, we define some artificial boundaries in this section of study. Calculation within this boundary is similar to that in the previous study, but calculation on the boundary needs some special treatment. Here we adopt the method of extrapolation which has one order of accuracy, and the concrete scheme is as follows:

Left boundary where $x = 0$ $\quad c^n_{0,j} = 2c^n_{1,j} - c^n_{2,j}, \quad 0 \le j \le m2$;

Right boundary where $x = m1 \times h2$ $\quad c^n_{m1,j} = 2c^n_{m1-1,j} - c^n_{m1-2,j}, \ 0 \le j \le m2$;

Bottom boundary where $y = 0$ $\quad c^n_{i,0} = 2c^n_{i,1} - c^n_{i,2}, \quad 0 < i < m1$;

Above boundary where $y = m2 \times h2$ $\quad c^n_{i,m2} = 2c^n_{i,m2-1} - c^n_{i,m2-2}, \ 0 < i < m1$

Where $h1$, $h2$ are the grid spacings along the x, y directions, respectively; $m1$, $m2$ are the numbers of grids along x, y directions, respectively.

2.2.3 Simulation on the inverse process of advection and diffusion

Some observations show that in conjunction with lapse of time, the center of oil spills shifts with

currents; What's more, the peak value of concentration decreases and the polluted area becomes larger accordingly. The process of backward calculation is just contrary to the above process. If our calculation is dependable, then in conjunction with the calculation the modeled affected area will become smaller and smaller, and the peak value increases gradually. At last, the centre of oil spills will return to its original position where oil spills occur. Figure 1 shows our simulated result under the condition that $u = 1.67$ m/s, $v = 1.67$ m/s, $D_x = D_y = 167$ m^2/s, and it is reasonably good (see Fig. 1).

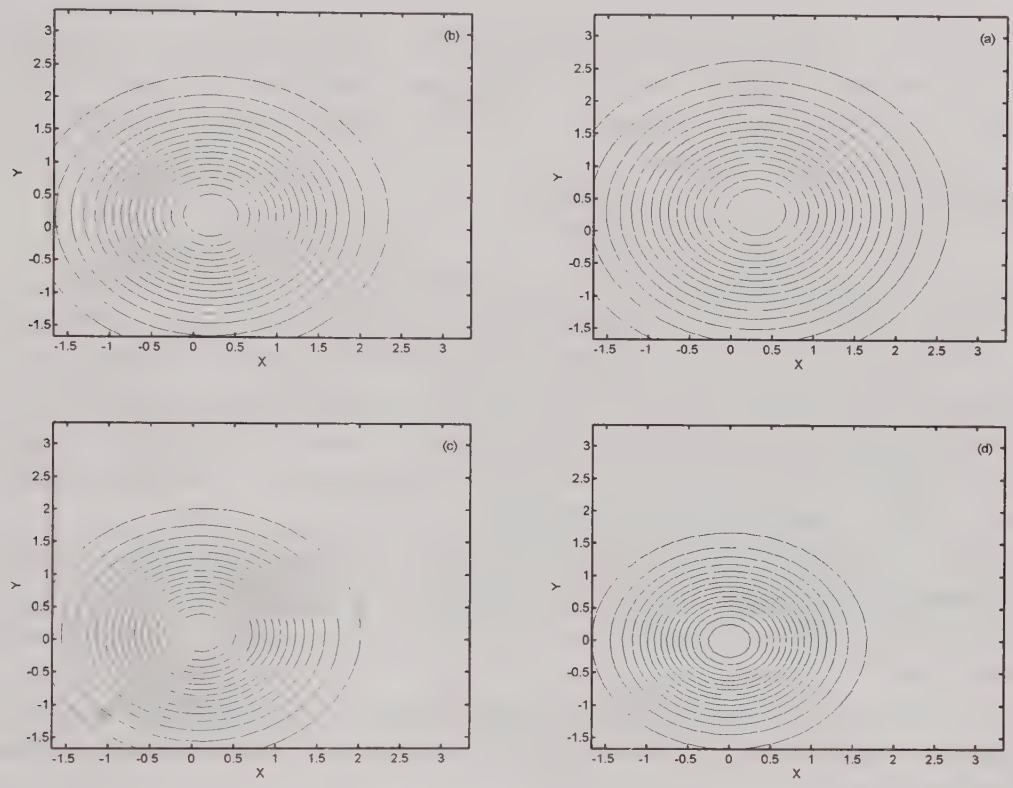

Fig. 1 The isoline distributions of oil spills concentration at the time of (a) $t = 3$ min, (b) $t = 2$ min, (c) $t = 1$ min, (d) $t = 0$.

(Assume the site of spilling oil as the coordinate origin, and the unit along both x and y directions are km.)

3 Conclusion

The numerical method established in this study can be applied to both open and closed as well as semi-closed marine spaces, and the modeled results are satisfying.

We suggest that the increasing grid density could effectively improve results in the course of analyzing numerical error, but it is not so simple in the actual cases. On the one hand, the grid density depends on, to a large extent, the stability of scheme: the sturdier a scheme is, the less restriction it

exerts on the grid density. The scheme used in this study is conditionally steady, so it is impossible to allow the grid spacing to decrease unlimitedly. On the other hand, diffusion terms functionally accumulate error. If we increase the computation precision only by means of thinning the grid density, it definitely will be at the cost of increasing the computation load which undoubtedly enhances the appearance odds of error. Therefore, over-thinning the grid is not worth the candle.

Acknowledgements

This research is funded by NSFC 40076005 and Frontier Innovation Project L390221103 from the Chinese Academy of Sciences, so their help is greatly appreciated; in addition, we also gratefully acknowledge the financial support from the National Tenth Five-Year Key Project H57022113.

Reference

[1] Yin Peihai. *Antipollution technique at vessels and ports.* Dalian Maritime Univ. Press, Dalian, 1991.

[2] Liu Hao. *Numerical simulation of backward tracing oil spills.* Dalian Maritime Univ. Press, Dalian, 2003.

[3] Jiang Yanqiao.*Antipollution technique on ocean ships.* Shanghai Jiaotong Univ. Press, Shanghai, 2000.

[4] Yu Changzhao. *Introduction on environmental fluid dynamics.* Tsinghua Univ. Press, Beijing, 1998, 104-183.

[5] Shen Mengyu, Zhang Zhibin, Niu Xiaoling. Some advances in study of high order accuracy and high resolution finite difference schemes. In: *New advances in computational fluid dynamics-theory, method and application.* Higher Education Press. Beijing, 2001, 62-95.

[6] Beam R M, Warming R F, Yee H C. Stability analysis of boundary conditions and implicit difference approximation for hyperbolic equations. *J Computational Physics*, 1982, 23: 299-329.

[7] Zhang Diming, Cai Congxi, *et al. Computational Fluid Dynamics.* Zhongshan Univ. Press, Guangzhou, 1991, 2-148.

[8] Peyret R, Taylor T D. *Computational methods for fluid flow.* Springer-Verlag, New York, 1982, 157-163.

[9] Chai J C, Lee H S, Patankar S V. An evaluation of differencing practice for the discrete ordinates methods.. *J Thermophys Heat Transfer*, 1994, 28:140-144.

Distribution Characteristics of Heavy Metals and Grain Size of Sediments from Hailing Bay, China

QIU Yaowen (丘耀文)[1, 2], ZHU Liangsheng (朱良生)[1], LI Manqiu (黎满球)[1]

1 *Key Lab of Tropical Marine Environmental Dynamics, South China Sea Institute of Oceanology, Chinese Academy of Sciences, Guangzhou* 510301, Guangdong, China

2 *State Key Lab of Organic Geochemistry, Guangzhou Institute of Geochemistry, Chinese Academy of Sciences, Guangzhou* 510640, *Guangdong, China*

Abstract The geochemical properties of sediment in the nearby seawater areas of Hailing Bay of the western Guangdong province were first time investigated in the dry period of 2001 and the flood period of 2002, respectively. The temporal and spatial characteristics of Cu, Pb, Zn, Cd and Hg concentrations, organic carbon and total sulfides contents, and granulometric distribution in the surface sediment from the Hailing Bay were analyzed. Results demonstrated that there were no remarkable changes in the composition of sediment between the dry period and the flood period; the average concentrations of Cu, Pb, Zn, Cd and Hg were 32.1 ± 17.5, 36.1 ± 10.0, 107.0 ± 37.4, 0.26± 0.15 and 0.109 ± 0.073 mg • kg^{-1}, respectively; the organic carbon and total sulfides contents were 1.33 ± 0.53 % and 140.13 ± 136.42 mg • kg^{-1}, respectively; surface sediments were dominated by clayey silt and sand, and their mean grain size was 4.62 ± 2.36 ϕ and in the range 0.52-7.55 ϕ ; there existed obvious correlation between the concentrations of Cu, Pb, Zn and Hg, and among Cu, Pb, Zn and Hg concentrations, organic carbon contents and grain size of sediments.

Keywords Heavy metals, Grain size, Sediment, Hailing Bay

Introduction

Hailing Bay located in western Guangdong province is an important marine aquaculture base and a famous scenic spot. Moyang River which flows across Yangjiang is the major runoff and polluted source in the sea area of Hailing Bay. Hailing Bank (approximately 5 000 m) which was built to connect Hailing Island and the continent in 1964 has blocked the natural circulation of suspended sand and pollutants in seawater. Water flux through the Yangjiang harbor extensively decreases that results in the rapid development of sand bar in the watercourse. And the sand bar expands from west to east at an average rate of 100 m/a, approximately. There is some danger that the watercourse from the Yangjiang harbor in the nearby of Hailing Bay will be blocked. Marine ecological environment has changed dramatically. Therefore, to develop the comprehensive study on ecological environment is significantly meaningful for the sustainable development of regional economy.

Received on December 12, 2004

Granulometric composition of sediment reflects much information, including mineral components, surface physical-chemical properties, specific surface area and surface free energy of sediment, and has significant effects on the absorption-desorption and transportation of heavy metals. Most of heavy metals entering the water environment through different pathways will be rapidly migrated into sediment by the absorption-deposition of suspended matter. Suspended matter will deposit gradually to the sediment in the process of transportation by water current when its gravitation is larger than its buoyancy[1]. Sediment has been considered as an ultimate source and sink of environmental pollutants (e.g., heavy metals, *etc.*). Environmental factors such as pH, Eh, organic carbon and sulfides in sediment have a key important action in geochemical processes (e.g., transportation and transformation, *etc.*) of heavy metals. To study the relationships between heavy metal concentrations and grain size composition, organic carbon and sulfide contents in sediment has a very important meaning for disclosing the polluted sources and the current polluting status of heavy metals and their ecological risk in the local sea region.

1 Sampling and analysis method

Thirty surface sediment samples were collected first time along the coastal area of Hailing Bay (history investigation only conducted off Hailing Bay[2-3]) in the dry period (December 2001) and the flood period (June 2002). Sampling locations are showed in Figure 1. For the method of sampling and analysis, refer to The Specification for Marine Monitoring (GB17387-1998). Sulfide samples were sealed in brown glass jars and stored in -4 ℃, taken back to laboratory and the sulfide contents were analyzed using methylene blue spectrophotometry. Sediment samples for the analysis of organic carbon and heavy metals were dried naturally, ground and screened in 80 meshes. Organic carbon content was analyzed by potassium dichromate oxidation-reduction. Meanwhile, the concentrations of Pb, Zn and Cd were analyzed by flame atomic absorption spectrometry (BSFS-2100), and the concentration of Hg by

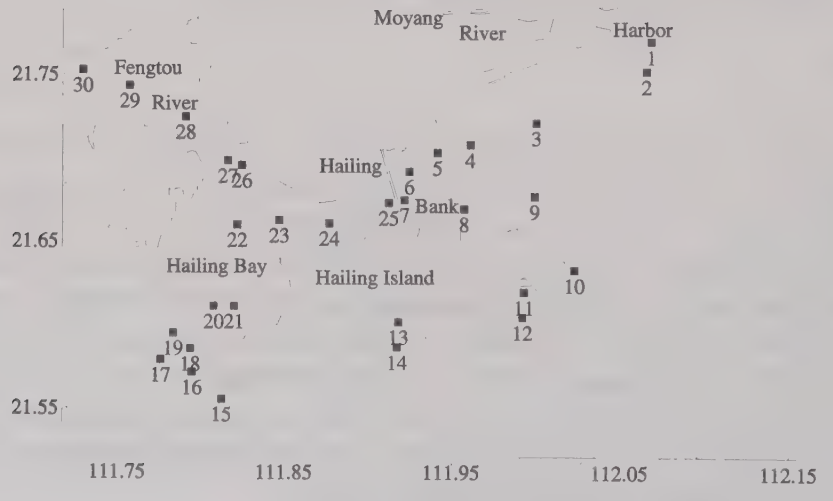

Fig. 1 Sampling locations at the Hailing Bay

cold atomic fluorescence spectrometry (XGY1012). The analysis and nomenclature for grain size of sediment were referred to the China National Standard (GB/T13909-92). Analytical flows of grain size were as follows: sampling, drying, weighing, adding Sodium hexametaphosphate and water, and then soaking, filtering through the water sieve with a diameter of 0.063 mm. The sample on the sieve (> 0.063 mm) was analyzed by sieve analysis after drying; and the sample under the sieve (< 0.063 mm) was analyzed with granulometry (SKC-2000, Japan). Concentrations of organic carbon, sulfide and heavy metals had not been analyzed for those samples with high percent of sand.

2 Results and discussion

2.1 Sediment composition

Grain size of sediment is a specific parameter. Mean grain size and median diameter may reflect the general characteristics of granulometric composition of sediment, while the values of skewness and kurtosis reflect uniformity of the distribution of sediment composition. The distribution of sediment composition depends on the equilibrium between gravity of sediment and water forces. There is smaller tidal current speed both in the supratidal zone and on the two sides of estuary, and there is much smaller tidal current speed during the still tide. Therefore, fine-grained sand is easy to deposit. From estuary to shallow sea, suspended sand tends to be finer and the content of clay in sediment is high due to its migrating distances.

As there was no remarkable variation of the composition of sediment both in the dry period and in the flood period, the research results were only reported for the dry period (December, 2001). Primary surface sediment types were clayey sand and sand (Table 1). Generally, surface sediment types were mainly clayey silt along Moyang estuary and the eastern Hailing Bank, sand in Hailing estuary, and also clayey silt from the Hailing Bay to the western Hailing Bank, respectively. Relatively high contents of sand in the sediment of the whole nearby water areas of Hailing Bay were observed. Sediment type was primarily silty clay off southeastern Hailing Island[3]. The mean grain size varied from 0.52 ϕ to 7.55 ϕ, with an average of 4.62 $\pm$ 2.36 ϕ. Most of skewness value was positive and varied from -0.41 ϕ to 0.81 ϕ with an average of 0.33 ϕ. Kurtosis value was in the range 0.53 - 1.85 ϕ with an average of 1.09 ϕ and was a little higher in the location 8.

2.2 The distribution characteristics of heavy metals, organic carbon and sulfides

In the water areas of the western Guangdong province, pollutants carried by the Pearl River water running into the South China Sea, flowing west along coast by means of coastal density current in the southwestern Guangdong province, may influence the areas far away even outside the Zhanjiang harbor (including the nearby water areas of Hailing Bay)[5]. Therefore, the concentrations of heavy metals in the sediment of this region will also be influenced by the water system of Pearl River. In the nearby water areas of Hailing Bay, the concentrations of Cu, Pb and Cd in the sediment varied very little between the dry period and the flood period, though Zn and Hg contents in the sediment during the dry period were higher than those during the flood period (Table 2). The reason why the concentrations of Zn and Hg in the sediment during the dry period were relatively high was that, on the one hand, the runoff (Moyang River and Fengtou River) flowing into this seawater area was small and its variation

did not change much between the dry period and the flood period and so its effects were also slight; on the other hand, seawater off Hailing Island polluted by the water system of Pearl River was affected much more, compared to the seawater in the nearby water areas of Hailing Bay.

Tab. 1 Grain size composition of surface sediments in the Hailing Bay during the dry period

Location	Mean Grain Size	Skewness	Kurtosis	Name
		ϕ		
1	7.10	0.49	1.19	Clayey Silt
2	6.63	0.35	0.98	Clayey Silt
3	6.65	0.24	1.08	Clayey Silt
4	5.00	0.81	1.46	Silty Sand
5	5.94	0.42	1.24	Sandy Silt
6	6.44	0.45	1.79	Silt
7	7.15	0.68	0.86	Clayey Silt
8	2.85	0.72	5.77	Medium Sand
9	5.66	0.09	0.93	Sandy Silt
10	7.33	0.75	0.61	Clayey Silt
11	7.41	0.67	0.53	Clayey Silt
12	7.31	0.76	0.53	Clayey Silt
13	1.26	0.26	0.90	Fine-Coarse Sand
14	7.31	0.78	0.54	Clayey Silt
15	2.15	-0.4	1.22	Medium-Fine Sand
16	0.98	-0.2	0.82	Fine-Medium Sand
17	2.89	-0.3	1.10	Fine Sand
18	4.82	0.46	1.33	Silty Sand
19	2.88	0.17	1.85	Fine Sand
20	2.65	0.36	1.53	Fine Sand
21	1.61	-0.1	1.40	Medium-Fine Sand
22	2.54	0.28	1.03	Sand
23	4.33	0.25	1.50	Silty Sand
24	4.31	0.35	1.02	Silty Sand
25	7.06	0.65	0.75	Clayey Silt
26	4.15	0.58	1.83	Very Fine Sand
27	5.39	-0.1	0.93	Clayey Silt
28	7.55	0.44	0.55	Clayey Silt
29	0.73	-0.1	1.08	Coarse-Medium Sand
30	0.52	-0.1	1.08	Medium-Coarse Sand

The distribution of the concentrations of Cu, Pb, Zn, Cd and Hg in the sediment from the Hailing Bay both in the dry period and the flood period was showed in Figure 2. There was no remarkable change for heavy metal contents in various locations. The concentrations of heavy metals were a little

Tab. 2 The concentrations of heavy metals, organic carbon and sulfide in the surface sediment from the Hailing Bay / mg • kg^{-1}

Time	Concentration	Cu	Pb	Zn	Cd	Hg	Sulfides	Organic Carbon*
Dry period (2001)	Mean	33.2	35.5	123.9	0.25	0.167	183.65	1.12
	Minimum	6.6	19.0	66.0	0.00	0.050	7.40	0.60
	Maximum	59.3	49.7	186.5	0.59	0.292	466.70	1.80
Flood period (2002)	Mean	31.1	36.6	92.6	0.27	0.059	103.14	1.51
	Minimum	4.1	16.8	35.9	0.10	0.012	14.60	0.34
	Maximum	64.0	56.1	136.1	0.40	0.099	361.71	2.45

Note: * Unit of Organic carbon is %

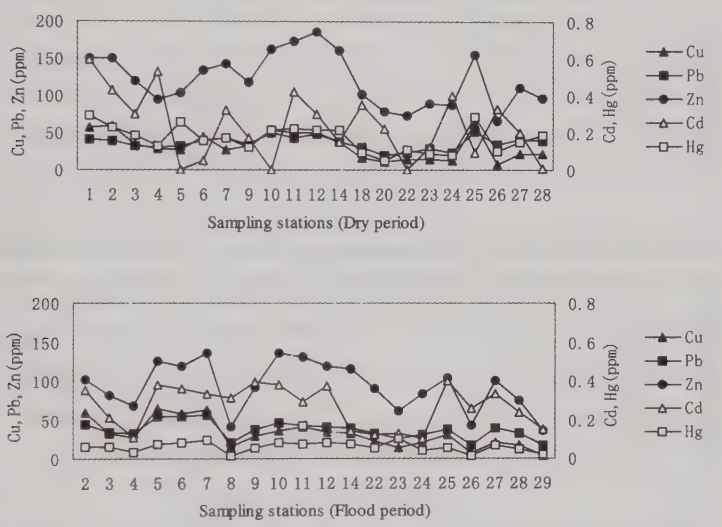

Fig. 2 Variation of heavy metal concentrations in the surface sediments from the Hailing Bay in relation to sampling stations in the dry and flood periods, respectively

higher in the dry period than those in the flood period. Heavy metal concentrations in Fengtou River and outside of Moyang estuary were slightly high, partly resulted from land pollutants, and were consistent with the fact that the corresponding sediment type was mostly clayey silt. Heavy metal contents in the Hailing Bay and in the water areas east of Hailing Island were relatively low. This was because of high current speed and high wave and sandy sediment absorbing relatively small contents of heavy metals in this region. In addition, Zn content was relatively high in the water areas east of Hailing Island. The reason is unknown and shall be further investigated in future. The average concentrations of Cu, Pb, Zn, Cd and Hg and their ranges were showed in Table 2. The total average concentrations of Cu, Pb, Zn, Cd and Hg were 32.1 ± 17.5, 36.1 ± 10.0, 107.0 ± 37.4, 0.26 ± 0.15, 0.109 ± 0.073 mg • kg^{-1}, respectively. According to the China National Quality Standard (first class) for marine sediment

(GB18668-2002), the percents which exceeded the standard for Cu, Zn, Cd and Hg in the dry period were 38.1 %, 28.6 %, 9.5 %, 38.1 %, respectively, and Pb did not. Meanwhile, only Cu exceeded the standard (25.0 %) in the flood period.

The average concentrations of organic carbon and sulfide were 1.33 ± 0.53 % and 140.13 ± 136.42 mg • kg^{-1} in the surface sediments from the nearby water areas of Hailing Bay (Table 2). Organic carbon and sulfide contents in the sediments from the water areas of the eastern Hailing Bank to the water areas of the southeastern Hailing Island and the upper reaches of Fengtou River were relatively high. There was a good relationship between organic carbon contents in sediment and phytoplankton density in coast. Organic carbon contents in the sediment from the nearby water areas of Hailing Bay (Table 2) were close to those in the sediment of China's eastern rivers (1.16 %) and were lower than those in the sediment of Pearl River (2.62 %)[1]. They were also close to the historical investigation data in other water areas of Guangdong province[2]. Vegetation compositions were abundant along the Hailing Bay located in the northern border of tropic zone, gestated by tropic monsoon and oceanic climate. Primary productivity in this region was in medium level. The average phytoplankton biomass was 5.70×10^6 Ind • dm^{-3} in spring and 1.15×10^6 Ind • dm^{-3} in autumn in the seawater areas of Yangjiang [3]. This was consistent with the result that organic carbon contents were higher in the flood period than those in the dry period. The average of sulfide contents was elevated than the historical investigation data in other water areas of Guangdong province[2]. Some of sediment samples had a sulfide stink when samples were being collected. The variation of sulfide contents in the sediment was larger. This was related to the poor water exchange and the deficient dissolved oxygen in the water body and the reduction condition existing for long time in the sediment of this water area.

2.3 The influence of sediment chemical composition on heavy metal distribution

The formation of marine sediment was primarily controlled by water forces (e.g., wave, tide), physical-chemical processes (e.g., sources, flocculation, deposition and oxydation-reduction reactions) and biological processes (e.g., faeces, bioturbation). Grain size of sediment was an important means for studying deposition environment of water dynamics. The spatial variation of the distribution of sediment grain size reflected the comprehensive results by many kinds of forces migrating in the same deposition environment [6-7]. Whether or not chemical changes occurred in the elements and compounds in the process of deposition, the carrier media, which accompanied the elements and compounds, would be dispersing / accumulating particles. The closer the intrinsic correlation of elements and compounds is, the more similar their distribution trends are. Heavy metals in marine environment can easily form metal organic complexation and metal sulfides and can be removed from the water body by surface absorption, cation exchange reaction and chelate reaction[8-9]. Correlative statistical analyses among heavy metals, grain size (Mz), organic carbon (OM) and sulfides (ΣS) in surface sediment from the nearby water areas of Hailing Bay both in the dry period and the flood period were carried out, respectively, using the Parson method (SPSS12 statistical software). The results (Table 3) demonstrated that their correlativity was similar both in the dry period and the flood period. The concentrations of Cu, Pb, Zn and Hg were clearly correlated in two cruises, indicating that their sources and spatial distribution were similar. There was no relativity between Cd content and other heavy metal contents in the dry period, but Cd content was correlated to Cu, Pb and Zn contents in the flood period.

Concentrations of Cu, Pb, Zn and Hg were obviously correlated to the average of grain size of sediment both in the dry period and the flood period, respectively, which was consistent with the results of documents [1, 10], *i.e.*, the smaller the grain size of sediments were, the higher the concentrations of heavy metals were. Concentrations of Cu, Pb, Zn and Hg were markedly correlated to organic carbon contents in the sediment both in the dry period and the flood period, respectively. Concentrations of Pb and Zn in the dry period and only concentration of Zn in the flood period were correlated to sulfide contents, respectively. Organic carbon contents in the sediment were obviously correlated to the average of the grain size of sediment from the Hailing Bay both in the dry period and the flood period. The result confirmed the conclusion that the migration and accumulation of organic carbon in shallow sediment was accompanied by fine-grained particles and was similar to the results in Yellow Sea[11, 12].

Tab. Calculation results of correlative matrix (n = 21)

Factors	Time	Mz	OM	ΣS	Cu	Pb	Zn	Cd	Hg	Time
Mz		1	0.796**	0.405	0.745**	0.866**	0.922**	0.312	0.719**	
OM		0.689**	1	0.388	0.717**	0.884**	0.875**	0.443	0.683**	
ΣS		0.514*	0.459*	1	0.127	0.276	0.469*	0.409	0.226	
Cu	Dry period (2001)	0.765**	0.524*	0.268	1	0.929**	0.789**	0.539*	0.582**	Flood period (2002)
Pb		0.837**	0.693**	0.551**	0.768**	1	0.927**	0.556*	0.719**	
Zn		0.834**	0.501*	0.522*	0.888**	0.808**	1	0.511*	0.769**	
Cd		0.04	-0.292	-0.046	0.131	-0.063	0.13	1	0.253	
Hg		0.809**	0.568**	0.219	0.835**	0.745**	0.742**	0.006	1	

Note: **p=0.01, *p=0.05

4 Conclusions

(1) The average concentrations of Cu, Pb, Zn, Cd and Hg in the surface sediment from the nearby seawater areas of Hailing Bay in the dry period of 2001 were 33.2 ± 17.3, 35.5 ± 8.1, 123.9 ± 37.1, 0.25 ± 0.18, 0.167 ± 0.068 mg • kg^{-1}; and in the flood period of 2002 were 31.1 ± 18.0, 36.6 ± 11.5, 92.6 ± 31.8, 0.27 ± 0.11, 0.059 ± 0.025 mg • kg^{-1}, respectively. Heavy metals pollution in the Hailing Bay was relatively slight.

(2) The average organic carbon contents in the sediment were 1.12 ± 0.38 % in the dry period and 1.51 ± 0.58 % in the flood period. The average sulfide contents in the sediment were 183.65 ± 157.04 mg • kg^{-1} in the dry period and 103.14 ± 106.59 mg • kg^{-1} in the flood period. Organic carbon contents were close to the historical data in the other water areas of Guangdong province, but sulfide contents were relatively high. The types of surface sediment were dominated by clayey silt and sand, with a mean grain size of 4.62 ± 2.36 ϕ.

(3) There was remarkable correlativity among Cu, Pb, Zn, Hg concentrations and between Cu, Pb, Zn, Hg concentrations, organic carbon contents and the mean grain size of sediments. Further study should be done to analyze the concentration of heavy metals and their chemical forms in different media

(seawater, suspended particle matter, sediment core and organisms) in order to better elucidate the polluted sources and ecological risk of heavy metals in this region.

Acknowledgements

This paper was supported by the National Key Development Programme for Basic Sciences of China under the contract No. 2001CB409706 and the Key Project of Yangjiang Government.

References

[1] Chen J S, Wang F Y, Song J J, et al. Relation of geochemical and surface properties to heavy metal concentrations of sediments from eastern Chinese Rivers. *Environ. Chem.*, 1996, 15(1): 8-14.

[2] Comprehensive investigating group for coastal zone and beach resources in Guangdong province. *Report on Comprehensive investigation for coastal zone and beach resources in Guangdong province.* China Ocean Press, Beijing, 1987, 267-333.

[3] Lin Z H, Li G Q. *Environmental quality of Islands in Guangdong province.* Guangdong science and technology press, Guangzhou, 1995, 91-177.

[4] Bao Y E, Fu W X. The control of sediment to heavy metals accumulation in Liaodong Bay. *Acta Oceanologica Sinica*, 1994, 16(3): 139-142.

[5] Ke D S. Contents and distribution of heavy metals in the offshore area along Gaungdong province. *Acta Scientiae Circumstantiae*, 1991, 11(1): 9-16.

[6] Gao S, Collins M. Analysis of grain size trends for defining sediment transport pathways in marine environments. *J Coastal Research*, 1994, 10(1): 70-78.

[7] Pedreros R, Howa H L, Michel D. Application of grain size trend analysis for the determination of sediment transport pathways in intertidal areas. *Marine geology*, 1996, 135: 35-49.

[8] Router J H and Rerdue E M. Importance of heavy metal - organic matter interactions in natural waters. *Geochim Cosmochim Acta*, 1977,41,325-334.

[9] Duursma E K and Dawson R. *Marine Organic Chemistry.* China Ocean Press, Beijing, 1992, 223-286.

[10] Lin S, Hsieh I, Huan K M, et al. Influence of the Yangtze River and grain size on the spatial variations of heavy metals and organic carbon in the East China Sea continental shelf sediments. *Chemical Geology*, 2002, 182: 377394.

[11] Gao S. Fin-grained sediment fluxes and cycling on continental shelve. *World S & T Research and Development*, 2000, 22(5): 73-77.

[12] Sun Y B, Gao S, Lu H Y. Influence of different pretreatment procedures on the particle size distribution of surficial sediments in the Northern Yellow sea. *Oceanol. Liminol. Sinica*, 2001, 32(6): 665-671.

Screening of Lectins in Crab and Shrimp from Fujian Coast of China

DAI Congjie (戴聪杰)[1, 2]

1 *College of Oceanography and Environmental Science, Xiamen University, Xiamen* 361005, *Fujian ,China*

2 *Department of Biology, Quanzhou Normal College, Quanzhou* 362000, *Fujian, China*

Abstract Twelve species of crustacean from Fujian coast were examined for lectins with different animal erythrocytes. Serum extracts fromall of 12 species showed agglutinating activity against at least two types of the erythrocytes used, which revealed the existence of lectins in these species. There were five species (*Penaeus japonicus, Lophosquilla costata, Charybdis feriatus, Portunus pelagicus, Scylla serrata*) whose serums could agglutinate all the erythrocytes tested. The lowest serum protein concentration required to produce erythrocytes agglutination varied remarkably, ranging from 0.7 μ g/mL to 8 080 μ g/mL. The strongest activity was shown in the agglutination of rabbit erythrocyte by serum of *Penaeus vanaminas*. Inhibition assays performed with seven mono- and bisaccharides showed that agglutination of quail erythrocytes by serums of three species (*Portunus pelagicus, Scylla serrata* and *Sesarma* sp.) were not inhibited by any sugars, while others were inhibited by at least three types of sugars. The assay of temperature influence on agglutinating activity showed that only *Penaeus japonicus* retained activity when the serum was heated to 90 ℃, and other serums lost their activity at 40 ℃, 50 ℃, 60 ℃, 70 ℃, 80 ℃ for 10 minutes, respectively.

Keywords serums, lectins, erythrocyte agglutination, crab and shrimp

Introduction

Lectins (or agglutinins) are carbohydrate-binding proteins having specific binding for certain types of mono- or polysaccharides, and they have been regarded as having a putative role in non-self recognition in vertebrate and invertebrate immunity[1-6]. In view of their special chemical and biological properties, they have applications in several research fields such as biochemisty, immunology, cell biology and cancer research. Lectins exist in almost all living organisms. They were first identified before the turn of this century as plant proteins capable of agglutinating red blood cells, but their ubiquity is now well established. Agglutinin molecules may occur at the surface of viruses, bacteria, yeast, protozoan and throughout all animal and plant kingdoms [7]. Their specificity is always determined by the type of carbohydrate to which they bind.

Concerning crustacean lectins, a number of reports regarding the purification and characteriz- ation of these molecules are now available[5]. However, very little is known about lectins from Chinese

Received on August 18, 2004

crustaceans. Due to the growing interest in the application of lectins and in getting useful data on isolation and purification of lectins from Chinese crustaceans, in the present study, we used animal erythrocytes to test the agglutinins in 12 species of Fujian coast crabs and shrimps, and also conducted agglutination inhibition assays with seven sugars and examined the effect of temperature on agglutinating activity.

1 Material and Methods

1.1 Crustacean specimens and preparation of test solution

Adult native crabs and shrimps in Table 1 were collected from the coast of Fujian Province, China, in March 2002. After collection, they were immediately transferred to laboratory. They were kept in large tanks under constant aeration and controlled temperature (26 ℃ - 28 ℃) and salinity (33 ℃ - 35 ℃). Only apparently healthy animals were used.

Crabs hemolymph was collected by shearing its feet, and shrimps hemolymph was collected by the insertion of a 26G gauge needle attached to a syringe into the shrimps' ventral sinus at the base of the first abdominal segment. Before bleeding, the shrimps' abdominal areas and crabs feet were cleaned with alcohol 70 %. Shrimps and crabs were bled only once.

For serum preparation, the extracted hemolymph (pools of 5-10 animals respectively) was allowed to coagulate for 16-24 h at 4 ℃. The clot was repeatedly centrifuged (2000×g) for 10 min at 4 ℃ and the supernatant was used as source of serums. The serum protein concentration was determined using Coomassie Brilliant Blue G250 and bovine serum albumin as a standard [8].

1.2 Assay for erythrocytes agglutination, sugar inhibition and the effect of temperature on the activity

Agglutination assays were performed with erythrocytes from sheep, rabbit, quail, chicken, snake, frog and fish, respectively. These animal erythrocytes were collected in a sterile Alsevers solution (100 mmol/L glucose, 20 mmol/L NaCl and 30 mmol/L sodium citrate, pH 7.2) at 4 ℃ and kept for a maximum of 1 week. Prior to their use in conventional hemagglutination assays, these red blood cells (RBC) were washed three times by centrifugation (800×g for 10 min) withTris-buffered saline (TBS): 50 mmol/L Tris-HCl, 0.15 mol/L NaCl, 3 mmol/L $CaCl_2$, pH 7.4, and then suspended at 2 % (V/V) in the same buffer. Agglutination tests using serial dilution procedure were done in 96-well microtitration plates. Equal volumes of erythrocytes suspension were added to each well containing test solution. The plates were gently shaken and kept at room temperature for 2 hour. The resulting agglutinations were observed macroscopically and their activity was expressed as the minimum active concentration. All assays were carried out in duplicate. Agglutination inhibitions by sugars were assayed only with quail erythrocytes, using the same assay method as described above but before adding a 2 % erythrocyte suspension, a solution (0.2 mol/L) of the following sugars were added: Lactose, D-Mannose, D-Fructose, D-Galactose, D-Arabinose, D-Glucose and Sucrose. The effect of temperature on the agglutinating activity was tested by first heating (for 10 min, at intervals of 10 ℃, from 40℃ to 90 ℃) a 1 mL test solution of each serum kept in a small air-tight bottle; and then testing each of the cooled solutions for agglutinating activity using quail erythrocytes in the same way.

2 Results

Agglutination assay results are summarized in Table 1. Of the 12 species tested, serum extracts from all of 12 species showed agglutinating activity against at least two types of the erythrocytes used, which revealed the existence of lectins in these species. Serum extracts from *Penaeus japonicus*, *Lophosquilla costata*, *Charybdis feriatus*, *Portunus pelagicus*, *Scylla serrata* could agglutinate all the erythrocytes tested, while serum extracts from *Portunus sanguinolentus* and *Sesarma* sp. could agglutinate only two types of erthrocytes. The minimum concentration of serum protein which was required to produce agglutinating activity varied remarkably, ranging from 0.7 μg/mL to 8 080 μg/mL. The strongest activity was shown in the agglutination of rabbit erythrocyte by serum of *Penaeus vanaminas*, and the weakest activity was shown in the agglutination of sheep and snake erythrocytes by serum of *Penaeus vanaminas*.

Tab.1 Agglutinating activity of serums from crustaceans using animal erythrocytes

Crustacean	Sheep	Rabbit	Quail	Chicken	Snake	Frog	Fish
Penaeus japonicus	1 070	535	66.9	535	267.5	267.5	267.5
Penaeus vanaminas	-	0.7	2 960	740	-	-	-
Macrobrachium rosenbergii	8 080	-	505	4 040	8 080	1 010	-
Macrobrachium japonicus	-	2 175	1 087.5	2 175	-	2 175	8 700
Lophosquilla costata	2 990	2 990	373.8	1 86.9	2 990	373.8	93.4
Charybdis feriatus	2 320	1 160	580	290	2 320	2320	72.5
riocheir japonicus	-	-	72.3	578.8	1 157.5	289.4	-
Portunus sanguinolentus	-	-	1 320	-	-	-	660
Portunus trituberculatus	-	67.2	4 300	-	-	-	4 300
Portunus pelagicus	1405	175.6	22	702.5	1 405	1 405	2 810
Scylla serrata	1 617.5	25.3	25.3	1 617.5	1 617.5	808.8	1 617.5
Sesarma sp.	-	-	15.6	-	-	1 000	-

Note: The data contain the minimum concentration (μg/mL) which produced agglutination. "-" = no agglutination.

Of the erythrocytes used, each animal erythrocyte was agglutinated by at least 6 species of crustacean. The quail erythrocytes were agglutinated by serums of all of crustacean species (12 species), followed by chicken and frog erythrocytes (9 species). On the other hand, comparison to other erythrocytes showed the most sensitivity of agglutination to crustacean serums.

Table 2 showed the results of agglutinating inhibition assays. The inhibitions by all srgars tested only occurred in the agglutination produced by the serum of *Portunus sanguinolentus*, while the agglutination by the serums of *Portunus pelagicus*, *Scylla serrata* and *Sesarma* sp. were not inhibited by any sugars and that of *Penaeus japonicus* was inhibited only by sucrose. Other inhibitions caused by at least three sugars were observed in agglutinations produced by serums of *Penaeus vanaminas*, *Macrobrachium rosenbergii*, *Macrobrachium japonicus*, *Lophosquilla costata*, *Charybdis feriatus*, *riocheir japonicus*, *Portunus trituberculatus*, respectively.

Tab.2 Agglutinating inhibition with quail erythrocytes by using seven sugars

Crustacean	Lac	D-man	D-fru	D-gal	D-glc	D-ara	Sur
Penaeus japonicus	-	-	-	-	-	-	+
Penaeus vanaminas	+	+	+	+	-	+	-
Macrobrachium rosenbergii	-	-	+	+	-	+	-
Macrobrachium japonicus	+	+	-	-	-	+	-
Lophosquilla costata	-	-	+	+	-	-	+
Charybdis feriatus	+	+	+	+	-	+	+
riocheir japonicus	+	+	+	+	-	-	+
Portunus sanguinolentus	+	+	+	+	+	+	+
Portunus trituberculatus	+	+	+	+	-	+	+
Portunus pelagicus	-	-	-	-	-	-	-
Scylla serrata	-	-	-	-	-	-	-
Sesarma sp.	-	-	-	-	-	-	-

Note: "+": Inhibition; "-": No inhibition; The minimum concentration of sugar which can produce inhibition is 100 mmol /L; Lac: lactose; D-man: D-mannose; D-fru: D-fructose; D-gal: D-galactose; D-glc: D-glucose; D-ara: D-arabinose; Sur: sucrose.

Except that *Penaeus japonicus* serum retained agglutinating activity, other crustacean serums agglutinating activity against quail erythrocytes were lost when their test solutions were heated at 90 ℃ for 10 minutes. Serums of *Penaeus vanaminas*, *Lophosquilla costata* and *Portunus sanguinolentus* lost the agglutination activity when they were heated to 40 ℃ for 10 minutes. Being heated to 50 ℃ for 10 minutes, in the serums of *Charybdis feriatus*, *Macrobrachium rosenbergii*, *riocheir japonicus* and *Portunus trituberculatus* agglutination activity could lose. Loss of agglutinating activity could also occur if serums from *Macrobrachium japonicus* and *Sesarma* sp., *Portunus pelagicus*, *Scylla serrata* were heated at temperatures of 60 ℃, 70 ℃, 80 ℃ for 10 minutes, respectively (Table 3).

Tab.3 Influence of temperature on the agglutinating activity of crustacean serums against quail erythrocytes

Crustacean	4 ℃	40 ℃	50 ℃	60 ℃	70 ℃	80 ℃	90 ℃
Penaeus japonicus	+	+	+	+	+	+	+
Penaeus vanaminas	+	-	-	-	-	-	-
Macrobrachium rosenbergii	+	+	-	-	-	-	-
Macrobrachium japonicus	+	+	+	-	-	-	-
Lophosquilla costata	+	-	-	-	-	-	-
Charybdis feriatus	+	+	-	-	-	-	-
riocheir japonicus	+	+	-	-	-	-	-
Portunus sanguinolentus	+	-	-	-	-	-	-
Portunus trituberculatus	+	+	-	-	-	-	-
Portunus pelagicus	+	+	+	+	-	-	-
Scylla serrata	+	+	+	+	+	-	-
Sesarma sp.	+	+	+	-	-	-	-

Note: "+": Agglutination; "-": No agglutination.

3 Discussion

Crabs and shrimps from only a few areas of the world have been examined for lectins and the number of active species was found to be very limited in comparison with the insects. In the present study, we screened lectins in crabs and shrimps from Fujian coast of China, and the serum extracts from all of 12 species have the capacity to agglutinate a variety of vertebrate RBC. The strongest agglutination titer was towards quail and rabbit erythrocytes and the weakest towards fish RBC.

Some of crustacean lectins lack specificity for monosaccharides, but most of crustacean lectins agglutinating activity was inhibited by one or more types of sugars. This results is supported by Hall & Rowlands (1974a)[9]. In the early 70s, Hall & Rowlands already emphasized the fact that multiple lectins with different sugar specificity could constitute an important evidence of lectin heterogeneity and, thus, support the hypothesis of the role of lectins as non-self- recognition molecules in crustacean defence. This suggests that the carbohydrate recognition domain in invertebrate lectins is well preserved through evolution, since lectins from several invertebrate phyla possess similar specificity for carbohydrate determinants[6, 10].

The results of the heat treatment of test solutions revealed that agglutinating activities of serum extracts from most of species were lost at the temperature of 40 ℃ - 70 ℃,but only one of the species was tolerant of high temperature of 90 ℃.We infer that the heat-durable property may be related to the chemical compositions of lectins existing in crustaceans, especially to polysaccharide content. The heat durability of species having high polysaccharide content is probably greater than those having low polysaccharide content, but further study would be necessary to verify this.

References

[1] Arason G J. Lectins as defense molecules in vertebrates and invertebrates. *Fish Shellf Immunol*, 1996, 6: 277-89.

[2] Matsushita M. The lectin pathway of the complement system. *Microbiol Immunol*, 1996, 40: 887-93.

[3] Vasta G R, Quesenberry M, Ahmed H, et al. C-type lectins and galectins mediate innate and adaptative immune functions: their roles in the complement activation pathway.*Dev Comp Immunol*, 1999, 23: 401-20.

[4] Wilson R, Chen C, Ratcliffe N A. Innate immunity in insects: the role of multiple, endogenous serum lectins in the recognition of foreign invaders in the cockroach, Blaberus discoidalis.*J Immunol*, 1999, 162: 1 590-6.

[5] Marques M R F, Barracco M A. Lectins, as non-self recognition factors, in crustaceans. *Aquaculture*, 2000, 191: 23-44.

[6] Olafsen J A. Lectins: models of natural and induced molecules in invertebrates.*Advances in Comparative and Environmental Physiology*, 1996. 24: 49-76.

[7] Sharon N, Lis H. Lectins as cell recognition molecules. *Science*, 1989, 246: 227-234.

[8] Alexander R R, Griffiths J M & Wilkinson M L. *Basic Biochemical Methods*. John wiley & Sons, New York, U S, 1985, 18-19.

[9] Hall J L, Rowlands D T. Heterogeneity of lobster agglutinins : II. Specificity of agglutinin-erythrocyte binding. *Biochemistry*, 1974a, 13: 828-832.

[10] Vasta G R, Ahmed H, Fink N E, et al. Animal lectins as self:non-self recognition molecules. Biochemical and genetic approaches to understanding their biological roles and evolution. *Ann. N.Y. Acad. Sci.*, 1994, 15 (712): 55-73.

Research on Measurable Nonlinear Relationship Between Phytoplankton Biomass and Environmental Factors in Bohai Bay

WANG Hongli (王洪礼), LI Shengpeng (李胜朋), FENG Jianfeng (冯剑丰)
Department of Mechanics, Tianjin University, Tianjin 300072, *China*

Abstract Based on the data of phytoplankton and environmental factors in the Bohai Bay, the dependence between the concentration of phytoplankton and environmental factors is analysed by linear correlation coefficient, rank correlation coefficient and Hoeffding test of independence .The result shows that wind-speed, air-pressure, surface temperature, field pH, salinity, DO, silicate and NO_3^- have a great impact on the concentration of phytoplankton.

Keywords Harmful algae bloom, Rank correlation coefficient, Test of independence

Introduction

In the past several years, the dependence between concentration of phytoplankton and environmental factors has been widely researched in many papers such as Zeng H S et al. (1993), Gu Y et al. (2002) and Wang H L et al. (2002) (2004)[1-4], which either came into qualitative conclusions without measurable relation by empiricism or only took linear correlation into consideration regardless of other correlations. In fact, the correlation between phytoplankton biomass and any environmental factors can be linear, or monotonic, even complexly functional. So in this paper we use the linear correlation efficient to describe linear dependence, rank correlation efficient to make monotonic dependence out and statistic of Hoeffding test of independence to exemplify more complexly functional dependence based on the data of concentration of phytoplankton and environmental factors in the Bohai Bay (May, 2003 to September, 2003), and the detailed information about rank correlation efficient and Hoeffding test of independence can be found in Hollander M, Wolfe D A (1973)[5].

1 Materials and methods

The sampling stations locate in the area presented in Fig. 1 where harmful algae blooms occur very frequently. Such survey region covers 117° 37′ - 117° 50′ E, 38° 49′ - 38° 54′ N, and the measured parameters include sunlight conditions (sc), wind speed (ws), field pH (pH), sea surface temperature (t), salinity (sd), ammonium (NH_4^+), nitrate (NO_3^-), orthophosphate (PO_4^{3-}), dissolved oxygen (DO), nitrite (NO_2^-), chemical oxygen demand (COD), silicate (SiO_4^{3-}), air pressure (p), chlorophyll *a* (chl*a*) and concentration of the phytoplankton (L). Moreover, sampling, preservation and analytical protocols were conducted by standard methods, phytoplankton biomass is taken in the light of

Received on October 23, 2004

the Specification for Oceanographic Survey and hydrometeorological factors and water quantity factors are measured according to the Provisional Specification for Oceanographic Pollutant Survey.

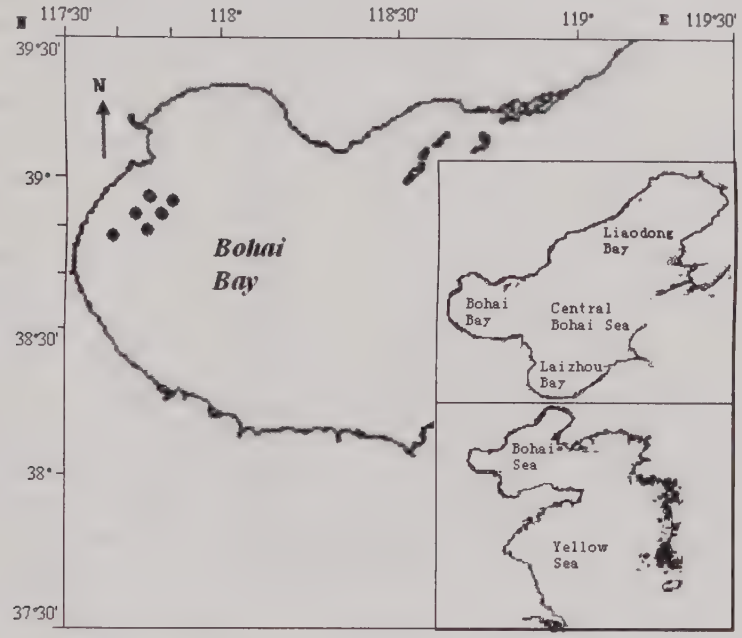

Fig.1 Study area with the sampling locations

2 Data analysis

Correlation coefficient is usually regarded as linear correlation efficient which can only show the linear dependence between two variables. In order to calculate other dependence, we introduce two rank correlation coefficients: Kendall τ and Spearman ρ, which mainly exemplify monotonic dependence. Generally, if all these coefficients are close to zero, we can draw the conclusion that the corresponding variables are independent, and then, a question appears, how to measure the closeness to zero accurately. For example, if linear correlation coefficient or rank correlation coefficient is 0.07, could we state that the two corresponding variables are independent? Certainly, it seems appropriate to consider the test of independence whose null hypothesis is that the two variables are independent, whose alternative hypothesis is that the two variables are dependent and whose testing statistic is these correlation coefficients. Under the 0.05 significant level, we reject null hypothesis if P-value is less than 0.05, that is to say, the two variables are dependent. Among lots of tests of independence, Hoeffding test of independence is widely used because it is stable to many kinds of complex dependence. In short, we take all these four tests of independence between phytoplankton biomass and one environmental factor respectively whose results and corresponding correlation coefficients are shown in Table 1.

Tab.1 Correlation coefficient and P-value for test of independence between phytoplankton biomass and environmental factors

L	Linear correlation coefficient	P-value	Kendall ρ	P—value	Spearman τ	P—value	Hoeffding' statistic	P—value
Sc	-0.066	0.517	0.074	0.275	0.09	0.372	-0.009	1
Ws	0.053	0.602	0.182	0.008	0.254	0.011	0.02	0.007
P	0.193	0.055	0.336	0	0.47	0	0.076	0
T	-0.258	0.01	-0.171	0.012	-0.238	0.018	0.029	0.002
pH	-0.42	0	-0.27	0	-0.385	0	0.039	0
Sd	0.152	0.134	0.186	0.007	0.268	0.008	0.028	0.002
COD	-0.073	0.472	-0.048	0.48	-0.056	0.582	-0.003	0.524
DO	0.189	0.06	0.148	0.03	0.222	0.027	0.016	0.014
PO_4^{3-}	-0.001	0.996	0.039	0.575	0.071	0.494	0.002	0.255
SiO_4^{3-}	-0.201	0.046	-0.167	0.014	-0.263	0.009	0.02	0.006
NO_3^-	-0.259	0.01	-0.139	0.042	-0.207	0.04	0.012	0.027
Chla	-0.102	0.314	-0.074	0.277	-0.116	0.252	0.006	0.099
NO_2^-	0.009	0.93	0.022	0.75	0.038	0.709	0.005	0.113
NH_4^+	0.425	0	0.001	0.983	-0.004	0.967	0.003	0.193

3 Results

3.1 Nonlinear correlation factors

It can been seen from Table 1 that the two rank correlation coefficients are consistent with Hoeffding test of independence, which shows that wind speed, air pressure, salinity and dissolved oxygen are dependent on phytoplankton biomass, but the linear correlation coefficient test supposes that the above four factors are independent of phytoplankton biomass. Obviously the dependence between phytoplankton biomass and each of the above four environmental factors is the monotonic rather than linear function usually assumed. Furthermore, the two rank correlation coefficients and the statistic of Hoeffding test about the four environmental factor above are greater than zero, which shows that the dependence between them and phytoplankton biomass is positive, that is to say, the corresponding concentration of phytoplankton rises as these factors increase. We also can take the test whose null hypothesis is that the two variable are independent, alternative one is that the two variables are positively (negatively) dependent and the statistic are still these correlation coefficients in order to explain the positively (negatively) dependent more accurately. But Hoeffding test can only test dependence rather than identifying a positive one or not, oppositely, the other three tests are able to test positive (negative) dependence whose results are the same as the above. The closer to the absolute value of correlation efficient is, the more dependent the variables are. Therefore, among the positive monotonic dependences between the four factors above and phytoplankton biomass, the largest one is air pressure, while salinity and wind speed are almost the same, dissolved oxygen is the least positively monotonously dependent on phytoplankton biomass among these four factors.

3.2 Linear correlation factors

The linear correlation coefficients between environmental factors such as sea surface temperature, field pH, silicate, nitrate and phytoplankton biomass are so big that P-values of the corresponding test of independence are more than 0.05. Consequently, we are sure that there is some linear dependence between such factors and phytoplankton biomass. We can also see the degree of dependence from the magnitude of absolute value of linear correlation coefficients and positiveness from the sign of the coefficient. Because the linear correlation coefficients and rank correlation coefficients between such four factors and phytoplankton biomass are less than zero, the linear dependence between them and phytoplankton biomass is negative, and the order of linear dependence from strong to weak is field pH, nitrate, sea surface temperature and silicate. Moreover, nitrate is almost as dependent on phytoplankton biomass as the sea surface temperature.

3.3 Independent factors

A special factor in Table 1 is ammonium which is linearly dependent on phytoplankton biomass, for its linear correlation coefficient between it and phytoplankton biomass is 0.425 and P-value of the corresponding test of independence is almost zero, thus P-values of the other three tests of independence must be close to zero because linear dependence is monotonic in theory. But the result is contradictory, the two rank correlation coefficients and the statistic of Hoeffding test of independence are small and P-values of corresponding tests are more than 0.05. In order to explain this phenomenon, we depict the scatter plot for standard phytoplankton biomass (minus mean and divided by standard deviation) against standard ammonium data, see Figure 2.

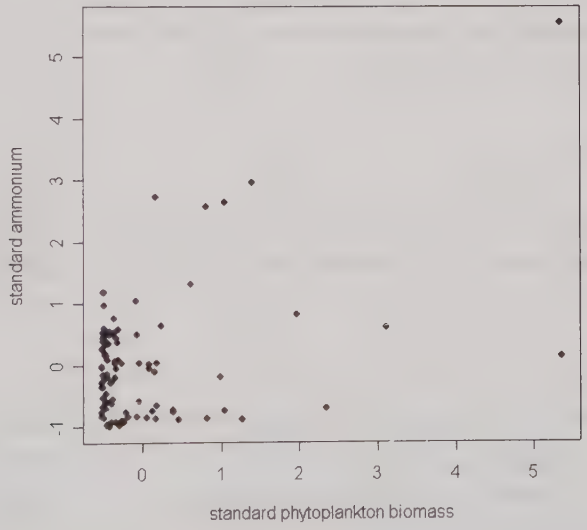

Fig. 2 Scatter plot for standard phytoplankton biomass and standard ammonium

It is clear from Figure 2 that there are two linear trends between the phytoplankton biomass and the factor ammonium, one of which is approximately horizontal, while the other is vertical. But we believe that there is no functional relationship between phytoplankton biomass and ammonium. As a result, rank

correlation and Hoeffding test of independence dont reject the null hypothesis. For the linear trend, the linear correlation coefficient is also relatively large, which displays the disadvantage of linear correlation coefficient. We prefer the result of other tests of independence and accept that ammonium has no relationship with phytoplankton biomass. The rest environmental factors, such as sunlight condition, chemical oxygen demand (COD), orthophosphate, chlorophyll*a* and nitrite, all can be considered to have little influence on the concentration of phytoplankton. Accordingly, we can set up a model later for blooming of phytoplankton regardless of these factors, which eliminates dimensions of model and greatly reduces the cost.

4 Discussion

We can draw the conclusion as follows from the analysis of data in the area where harmful algae blooms occur very frequently in the Bohai Bay:

(1) The environmental factors which influence phytoplankton biomass are air pressure, salinity, wind speed and dissolved oxygen (DO) in the Bohai Bay, and the dependence between each one of them and phytoplankton biomass can be positively monotonic. Moreover, the degree of dependence from strong to weak is air pressure, salinity, wind speed and dissolved oxygen (DO).

(2) Environmental factors, such as sea surface temperature, field pH, silicate and nitrate, have negatively linear dependence on phytoplankton biomass, and the degree of linear dependence from strong to weak is field pH, nitrate, sea surface temperature and silicate. Besides, nitrate and sea surface temperature have almost the same linear influence on phytoplankton biomass.

(3) The rest measured factors like sunlight condition, chemical oxygen demand (COD), orthophosphate, chlorophyll◊, nitrite and ammonium all can be considered to have little influence on the concentration of phytoplankton.

Acknowledgements

This work has been funded by the National Natural Science Foundation of China (grant NO. 10472077). We thank Professor Shi Daoji for guidance during statistical analysis of data.

References

[1] Zeng H S, Lin Y S and Yao R M. Research of Relationship between Cause of Harmful Algae and Number of Bacteria in West Sea around Xiamen. *Acta. Oceanologica. Sinica*, 1993, 15(6): 105-110.

[2] Gu Y, Xiang Y T. Relationship of Red Tide and Eutrophication in Xiangshan Harbor Area. *Marine Environmental Science*, 2002, 21(3): 67-69.

[3] Wang H L, Feng J F. Nonlinear Dynamics Research of the Algae Model in Bohai Sea. *Ocean Technology*, 2002, 21(3): 18-21.

[4] Wang H L, Feng J F, Sun J. Effect of Predation of Zooplankton on the Nonlinear Dynamics of Habs Population Model. *Marine Environmental Science*, 2004, 23(1):19-21.

[5] Hollander M, Wolfe D A. *Nonparametric statistical inference.* New York, 1973.

Heavy Metal Biosorption Sites Studies of *Laminaria japonica*

QIAN Aihong (钱爱红), WANG Xian (王 宪), DENG Yongzhi (邓永智), CHEN Lidan (陈丽丹)
College of Oceanography and Environment, Xiamen University, Xiamen 361005, *Fujian, China*

Abstract The role played by the functional groups of*Laminaria japonica* treated by methanol and formaldehyde in biosorption of the heavy metals was investigated. Infrared spectroscopy analysis and biosorption experiments show that both carboxyl and amino groups join in the sorption; chemical treatment decreased the biosorption efficiency of the heavy metals.

Keywords Biosorption, metal ion, infrared spectroscopy

Introduction

Nonliving biomass materials have been found to rapidly bind metals in high capacities[1-3]. Metal ion uptake by these biomaterials can interact with carboxylate, hydroxy, amine and xanthate groups in the cell walls. It is important to identity the functional groups responsible for metal binding to increase efficiency and selectivity. The information obtained from these determinations would be important in any future attempts at chemically or biosynthetically altering the material to enhance the binding capacity or to selectively bind specific metals. Furthermore, the identification of functional groups may redound to determining the biosorption mechanisms and can also introduce functional groups to increase selectivity. The infrared spectroscopy is a powerful measure of estimating the presence and change of functional groups.

The chemical modification techniques are of value in characterizing the functional groups responsible for metal binding. Kapoor et al.[1] study the role played by carboxyl, amimo and phosphate in the cell wall of A.niger in biosorption of lead, cadmium and copper by chemical treatments. These findings suggest that carboxylate and amine groups are important in metal ion biosorption on A.niger biomass. Phosphate groups and the lipids fraction of the biomass do not play a significant role. It can increase efficiency to introduce a functional group. For example, Kim et al.[5] introduced sulphur groups onto the cell surface of Undaria pinnatifida to increase the biosorption capacity for lead ions. Lawrence et al.[6] indicated that the esterification of carboxylate functionalities in the cell walls of Datura innoxia rerults in a decrease in metal uptake. These findings suggest that the carboxylate groups are important in metal ion adsorption to this biomaterial. Infrared spectra analysis is used to investigate the cadmium biosorption by nonliving *Sagassum*[7]. The results showed that carbonyl plays an important role in biosorption. Tang et al.[8] studied the pattern and type of lead biosorption by waste mucelium of *penicillium chrysogenum*. The results showed that chin and glucan as main components of cell wall all join in the sorption, and acetylamine group (-$NHCOCH_3$) and hydroxyl group (-OH) are combined cooperatively into the lead binding in which, the lead ion reacts preferably with the acetylamino group.

Received on November 11, 2004

The macroalga *Laminaria japonica* is easily gained in our country. The biosorption efficiency of metal ions on *Laminaria japonica* is higher than microalgae and fungus. The metal binding performance of this alga has been described[1, 9], but the infrared spectral analysis is still rarely seen. This article shows that *Laminaria japonica* has potential for achieving greater performance than conventional wastewater treatment processes.

1 Materials and methods

1.1 biosorbent

The biosorbent samples are obtained from the Yellow Sea in Qingdao. The algae are pre-treated by calcium chloride for 24 h. The calcium treated biosorbent is washed several times with deionized water. The biosorbent is then heated in an oven at 60 ℃ - 80℃ and sieved for later use.

1.2 Chemicals

Copper sulfate, cadmium chloride, calcium chloride, concentrated hydrochloric acid, sodium hudroxide, methanol, formaldehyde, and formic acid. All the reagents used are of analytical reagent grade and the deionized water is used for all experiments.

1.3 Chemical treatment

The calcium treated biosorbent is chemically treated with formaldehyde and methanol to understand the role of functional groups in biosorption of heavy metal ions. The chemical treatments are as follows:

Follow the procedure of Wang[9]. Twenty-five grams of algae are contacted with 500 mL of formaldehyde (HCHO) and 1000 mL of formic acid (HCOOH).The reaction mixture is shaken on a rotary shaker for 6h at 150 rpm. The resulted algae are then filtered and followed by sequential distilled water, 0.2 mol/L sodium carbonate, and final distilled water washes. Algae are dried at 80℃ for 10 h and finally 2 h at 110 ℃. The algae of 80 - 120 mesh are sieved for later use.

0.5 g of algae is suspended in 10 mL anhydrous methanol, and 0.2 mL concentrated hydrochloric acid is added to the suspension. The reaction is shaken on a rotary shaker for 6 h at 125 rpm.The suspension is then filtered and followed by sequential distilled water, 0.2 mol/L sodium carbonate, and final distilled water washes. Algae are dried at 80℃ for 10h and finally 2h at 110 ℃. The algae of 80 - 120 mesh are sieved for later use.

1.4 Method

1.4.1 Adsorption experiment

0.5 g dried algal powder is added into flasks, in which we have already added 200 mL initial metal solution (10 - 100 mg/L, pH=5.0). The flasks are shaken for 1 h, and each solution is extracted by centrifugation for 2 mL clear. The clear and initial metal salt solutions are analyzed for metal ions concentration with the aid of a Hitachi Z8000 atomic absorption spectrophotometer (AAS).

1.4.2 Infrared Analysis

All infrared spectra are obtained with a Fourier transform infrared spectrometer. For IR studies, 5 mg of *Laminaria japonica* is encapsulated in 150 mg of KBr. The disks are obtained by pressing the ground material with the aid of a bench press.

2 Results and discussion

The IR spectra of different chemically modified algae are used to evaluate the effects of chemical modification on the functional groups of algae. The shape of trough is about the same. It is showed that the chemically modified algae don't destroy the structure of algae.

The IR spectrum of *Laminaria japonica* is showed in Fig. 1.The adsorption at 3 389 cm^{-1} is strong broad and seems to be indicative of both NH_2 and O-H. The adsorption observed at 2 924 cm^{-1} results from the dissymmetric stretching vibrations of C-H group. The adsorption at 1 633 cm^{-1} is amine bending mode. The adsorption at 1 160 cm^{-1} is due to the stretching vibrations of C-O. The trough observed at 1 033 cm^{-1} results from the stretching vibrations of C-OH in the glucide. Fig. 2 shows the IR spectrum of *Laminaria japonica* treated with methanol and hydrochloric acid. The IR spectra show a trough at the wavenumber 1 735cm^{-1} as observed. The adsorption at 1 735 cm^{-1}, the stretching vibrations of C=O, is observed, which could be because the treatment causes the esterification of the carboxylic acids present on cells. Fig. 3 shows the IR spectrum of *Laminaria japonica* treated with formic acid and formaldehyde. This chemical treatment could result in the methylation of amino groups[10]. The reaction takes place as follows:

$$RCH_2NH_2 \xrightarrow{HCHO,\ HCOOH} RCH_2N(CH_3) + CO_2 + H_2O$$

The absorbency at 1 633 cm^{-1} is stronger than that in Fig. 1. The result shows that methylation takes place. The adsorption at 1 731cm^{-1} resulted from formic acid is found, which shows formic acid remains on the biomass even after washing[4].

The adsorption efficiencies of algae treated with different methods are showed in Fig. 4. From Fig. 4, we can find that the adsorption efficiency of the formaldehyde and methanol treated algae decrease. From IR spectrum and Fig.4, we can conclude that the carboxyl and amino affect the adsorption efficiency.

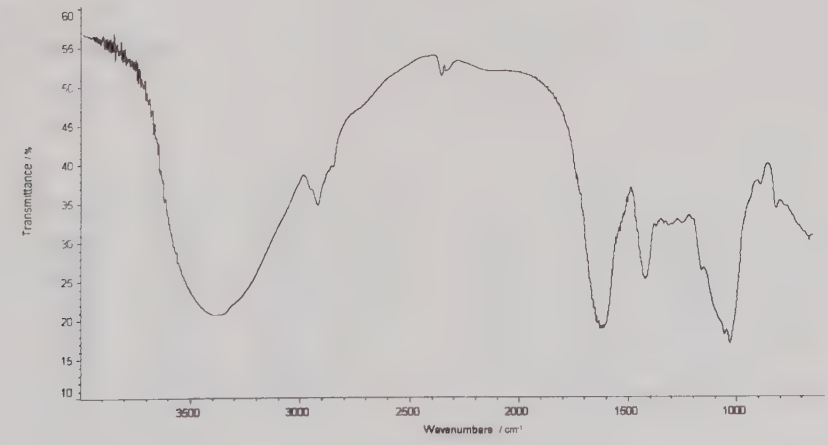

Fig. 1 Infrared spectrum of the calcium treated *Laminaria japonica*

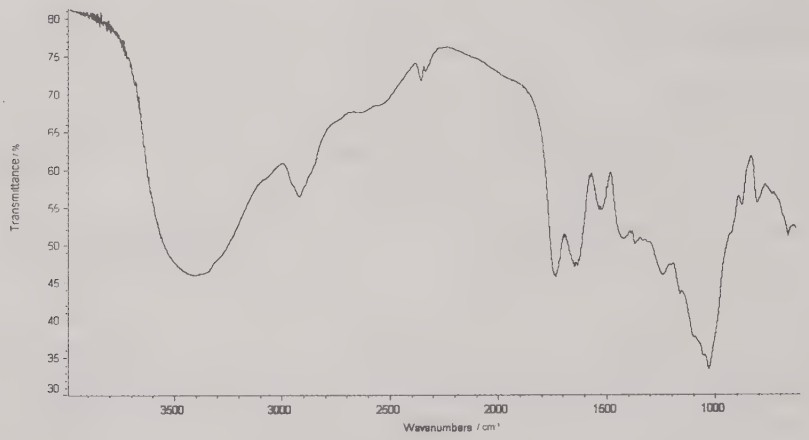

Fig. 2 Infrared spectrum of the methanol and hydrochloric acid treated *Laminaria japonica*

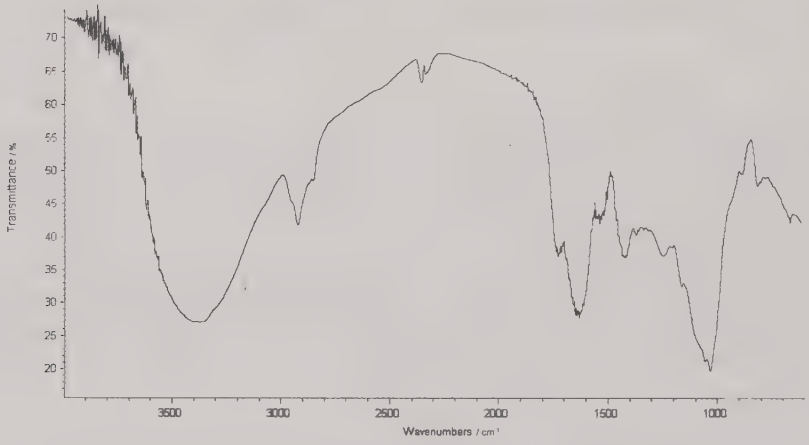

Fig. 3 Infrared spectrum of the formaldehyde and formic acid treated *Laminaria japonica*

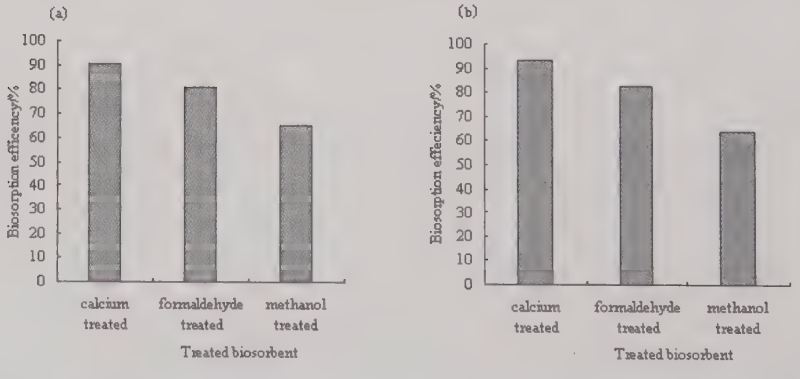

Fig. 4 The biosorption efficiency of *Laminaria japonica* to cadmium (a) and copper (b) after being treated with different methods

3 Conclusion

Laminaria japonica is treated with formaldehyde and methanol in this article. The IR spectrum is used to evaluate the effects of chemical modification on the functional groups of algae and the adsorption efficiency. The results are as follows:

(1) The shape of trough is about the same. It is showed that the chemically modified algae dont destroy the structure of algae.

(2) The carboxyl and amino are all join in the sorption in the process of the biosorption of cadmium and copper.

References

[1] Lin Ronggen, Huang Penglin, Zhou Junliang. Study on the adsorption and desorption of copper and cadium in water on two species of brown algae. *Marine Environmental Science*, 1999, 18(4):8-13.

[2] Yang Fen. The study on biosorption of copper (II) by immobilized algae. *Journal of Qujing Normal College*, 2000, 19(6):46-48.

[3] Yin Pinghe, Zhao Ling, Yu Qiuming, et al. Biosorption of lead, copper and cadmium by marine macro algae. *Marine Environmental Science*, 2000, 19(3):11-15.

[4] Kapoor A and Viraraghavan T. Heavy Metal Biosorption Sites In *Aspergillus Niger. Bioresource Technology*, 1997, 61:221-227.

[5] Kim Y H, Park J Y, Yoo Y J, et al. Removal of lead using xanthated marine brown alga, Undaria pinnarifida. *Process Biochemistry*, 1999, 34: 647-652.

[6] Lawrence R D, Lin S, Gary D R. Chemical modification and metal binding studies of *Datura innoxia. Environ Sci Thechnol*, 1996, 30:110-114.

[7] Guibal E, Roulph C, Cloirec P L. Infrared spectroscopic study of uranyl biosorption by fungal biomass and materials of biological origin. *Environ Sci Thechnol*, 1995, 29(10): 2496-2503.

[8] Tang yueqin, Niu hui, Lin jun, et al. Mechanism of Lead (′) Biosorption by Waste Mycelium of Penicillium Chrysogenum Identification of the Matters and The Functional Groups Participated of the Matters and the Functional Groups Participated in Lead Biosorption. *Journal of Sichuan University* (Engineering science edition), 2000, 33(3): 50-54.

[9] Wang J L. Biosorption of copper (II) by chemically modified biomass of*Saccharomyces cerevisiae. Process Biochemistry*, 2002, 37: 847-850.

[10] Yang hong, Ning qianji. The absorption of La3+,Ce3+ on the particles of kelp with chemical handling. *Experiment and Technology*, 2002, 26(5): 21-22.

Research of Influence of Aniline on the Growth of Ocean Algae

QIU Haiyuan (邱海源), WANG Xian (王 宪)
College of Oceanography and Environmental Science, Xiamen Univ., Xiamen 361005, *Fujian, China*

Abstract This article discusses the interaction of aniline and ocean algae based on the standard appraisal method of chemical medicine for algae toxicity. It is showed by experimental results that aniline has pretty toxic effects on algae. Suspended substances in water can offset some effects of aniline. It also discusses the dynamic constant of first order degradation reaction rate of algae on aniline from the point of view of chemical dynamics.

Keywords algae, *Plaeodectylum tricornutum*, aniline, growth

Aniline belongs to substituted aromatic hydrocarbons, which are widely used and toxic. However, there are not many reports on their toxic effects on algae. Algae are the main initiators of aquatic ecosystem [1]. 90 % of photosynthesis is carried out by them, which is very important to keep the normal running of aquatic ecosystem and the balance of ecosystem of the whole earth. In addition, algae are very sensitive to environmental changes, which can be used for inspection of aquatic pollutants[2].

Generally, organic pollutants are a kind of restrained factor for algae in water environment, whose concentration abides by Shelford's law of tolerance[3] when above the limit of tolerance. Within the limit of tolerance, they make the number of kinds of algae decrease and the quality decline. Firstly, algae gather together under the influence of organic substances, resulting in algae moving along with the food chain of biology or a series of biochemical reactions together with all kinds of enzymes in the bodies of algae, making organic substances degradated or transformed[4-6]. This article proceeds with the aniline effects on ocean algae, discusses theoretically the interaction of aniline and algae based on the toxic effects of aniline on different ocean algae and their tolerance ability with the existing of suspended substances in actual water, and provide basic materials for inspection of ocean algae and water quality.

1 Materials and methods

1.1 Main devices

Spectrophotometer: Model 721; Model 800 Centrifuge; Stainless Standard Sieve Ⅰ (300 mesh, Aperture 0.05 mm); Oscillator; Self-Made Manual Light Source Culture Box: 2·500W Iodine Tungsten Light Source; Model SYY1-1 Salinity Meter; Model Ph-3B PH Meter; Electrothermal Steam Sterilizer (YXQ602 Model).

1.2 Main agent

Aniline (A. R.) Third Firm of General Agent Factory of Shanghai; 1 % sodium nitroferricyanide;

Received on September 16, 2004

NaOH-KCl buffer solution; 0.02 mol/L EDTA solution; 0.01 mol/L NaClO solution; 90 % acetone (A. R.); F/2 inoculum[2].

1.3 Experimental algae seeds

Experimented ocean algae are provided by the Algae Laboratory of the Institute[7]: *Platymonas* sp; *Plaeodectylum tricornutum, Bull.*

1.4 Pretreatment of samples

Algae domestication: cultivate the two kinds of algae (*Platymonas* sp; *Plaeodectylum tricornutum*); Move the seeds once each 4 d, making the seeds purified and growing correspondingly. Record biomass every day (taking chla as unit) and draw a corresponding growing curve. Suspended substances: pick bottom mud of Haixia Ocean, dry, mill, and sieve the mud for use. Sterilized ocean water: Filtrate mixed solution of ocean water and distilled water by sands, sterilize for 40min under 125 ℃.

1.5 Experiment conditions

Temperature of Self-Made Manual Light Source Culture Box: (24 ± 2) ℃; Light source: white fluorescent lamp; Light intensity: 3 900 - 4 100 lx; Contrast ratio: 12 ∶ 12 h.

1.6 Test methods

Measurement of chlorophyll: filtrate 100 mL sample liquid with a 0.45 μ m filtration membrane, through mill tube, add 90 % acetone to the filtration membrane and mill it to broken pieces, and keep the final filtrate volume not over 10ml for testing[8].

Aniline test: Get 5ml filtrate to carry out the test based on the chloros photometric method[9].

2 Results and discussion

2.1 Toxic effects of different aniline on algae

Please see the toxic effects of aniline on algae in Fig. 1. It can be seen that: for *platymonas* sp,

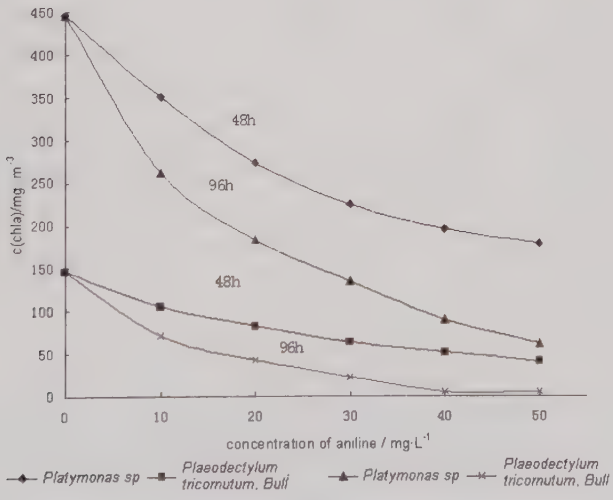

Fig.1 Toxic effects of aniline on algae

48 h Ec_{50} = 30 mg/L, 96 h Ec_{50} = 12.5 mg/L, Lc_{50} = 1.3 mg/L; for *plaeodectylum tricornutum*, 48 h Ec_{50} = 25 mg/L, 96 h Ec_{50} = 9 mg/L, Lc_{50} = 0.9 mg/L. The results show that the growth of *platymonas* sp and *plaeodectylum tricornutum* is severely restrained by aniline. With the gradual increase of aniline concentration in inoculum, the relative growth is decreased correspondingly. At the same time, the toxic effect of aniline on *platymonas* sp is greater than that on *plaeodectylum tricornutum.*

2.2 Toxic effects of aniline on algae with existing of suspended substances

2.2.1 Toxic effects of aniline on algae

The toxic effects of aniline on the above-mentioned two algae are compared with the existing of suspended grains. Please see Figs. 2 and 3 for the results.

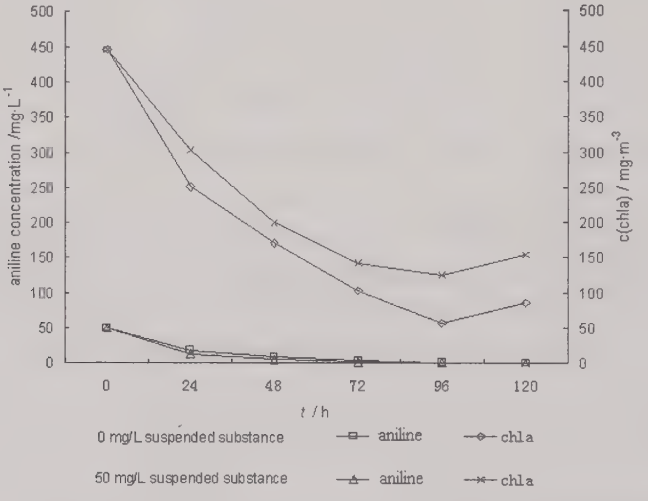

Fig.2 Effects of aniline on *Platymonas* sp

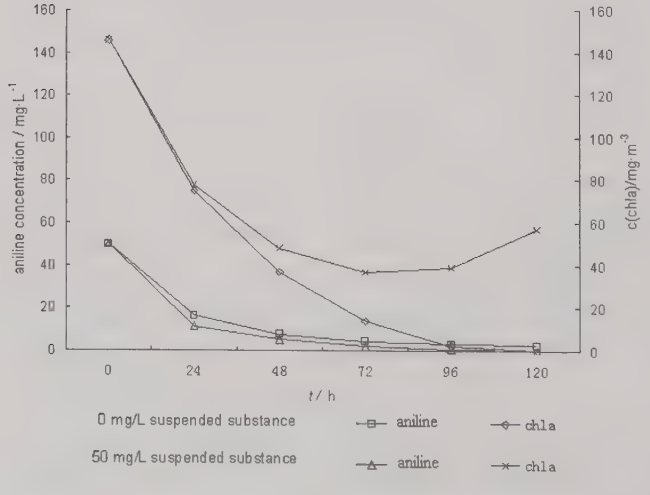

Fig.3 Effects of aniline on *Plaeodectylum tricornutum*

It can be seen from the results that the toxic effects of aniline on the two algae are reduced obviously with the existing of suspended substances. This shows that suspended substances have some adsorption function for aniline, which influences the toxic effects of aniline on algae directly or indirectly. It also shows, in the natural water environment, the relation of influence of toxic substances on ocean primary productivity and concentration of toxic substances is not linear. The toxic effects are related not only to the concentration of toxic substances, but also closely to the ocean environment, especially the existing of suspended substances. The result is consistent basically with the relative reports [8].

2.2.2 Dynamic effects of aniline on algae

Please see Tab. 1 for the experimental effects of aniline on algae. It can be seen from the results that the decrease process of aniline abides by the law of dynamics of first order reaction, and corresponds to the process of aniline degradation in water. Biodegradation constant of aniline could be estimated based on the first order reaction equation $C = C_0 e^{-kt}$ and the experimental results. In the reactors with the existing of suspended substances, effects of aniline on *platymonas* sp and *plaeodectylum tricornutum* are basically consistent with each other under the absorption function on aniline and functions on bio-carriers of suspended substances.

Tab.1 Analysis of effects of aniline on algae

Algae	Degradation substance	Suspended substances/ mg • L^{-1}	k	c_0	r
Platymonas sp	Aniline	0	0.885	50	0.975 (n=5)
Platymonas sp	Aniline	50	1.062	50	0.938 (n=4)
Plaeodectylum tricornutum	Aniline	0	0.950	50	1.000 (n=3)
Plaeodectylum tricornutum	Aniline	50	1.062	50	0.933 (n=4)

2.3 Effects of algae on the concentration of aniline in pond water

Field simulation experimental analysis is carried out for pond water in the base of Xiamen Railway Industry Corp. to find out about the effects of concentration of aniline on the biomass in pond water. Please see the results in Fig. 4. It can be seen from Fig. 4 that the content of chlorophyll of algae in marine water is smaller than that in pond water with the increase of concentration of aniline. It reflects that the existing of suspended grains in marine water could restrain the toxicity of aniline obviously. It also shows that marine water has some gathering and degrading effects on aniline. Toxicity of contaminate substances is closely related to water environments.

3 Results

(1) Aniline has obvious toxic effects on the above-mentioned two kinds of algae. Toxic effect of aniline on *plaeodectylum tricornutum* is slightly greater than that on *platymonas* sp.

(2) The degradation rate of aniline abides by the equation of first order dynamic reaction with the existing of suspended grains. Simultaneously, toxicity of aniline is influenced by absorption function.

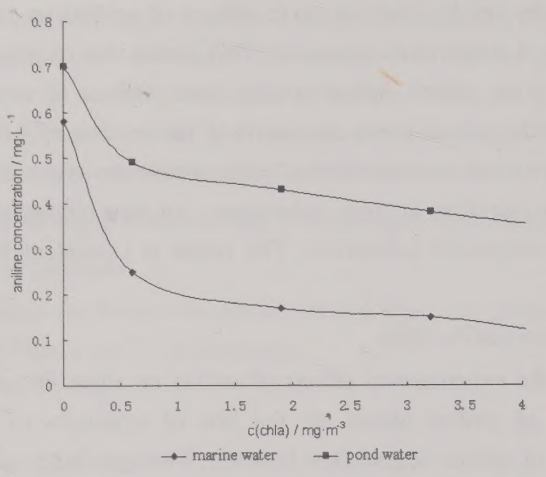

Fig.4 Effects of aniline on marine algae

(3) Natural water, *i.e.*, water with the existence of suspended grains, restrains the toxicity of aniline obviously. It also shows that marine water has some gathering and degrading effects on aniline. Degradation effects of aniline on *plaeodectylum tricornutum* and *platymonas* sp are close.

Acknowledgements

This paper was supported by the National Natural Science Foundation of Fujian (B0310001).

References

[1] Baden S A. (Translated by Wu Yuduan, Chen Cimei, Chen Yuwang, et al). *Ocean Pollution and Ocean Biology Resources.* Ocean Press, Beijing. 1991.

[2] Xia Beicheng. *Biodegradation of Environmental Pollutants.* Chemical Industry Press, Beijing, 2002.

[3] Odum E P. (Translated by Sun Ruyong). *Basic of Ecology.* The People's Education Press, Beijing, 103-105.

[4] Chattopadhyay D N and Konar S K. Chronic effects of a nonionic detergent on aquatic ecosystem. *Environ. Ecol.*, 1986, 4(1): 105-108.

[5] Tan Yuyun, Zhang Yongyuan and Sun Meijuan. Research on Transformation and End-results of straight chain alkyl sodium benzenesulfonate in simulated water ecology system. *Acta Scientiae Circumstantiae*, 1990, 10(3): 325-331.

[6] Yamana A N, Okada M, and Sudo R. The growth inhibition of planktonic algae due to surfactants used in washing agents. *Water Research*, 1984, 18(9): 1 101-1 105

[7] Sunda W G and RRL Guillard. The relationship between cupric ion activity and toxicity of copper to phytoplankton. *J Mar Res*, 1976, 34(4): 511-529.

[8] Li Wenquan, Wang Xian. Effects of Light Intensity and Environmental Factors on Ocean Primary Productivity. *Journal of Xiamen University (Natural Science)*, 1989, 28(4): 423-426.

[9] Yuan Cunguang, Liu Guangdong, Feng Chengwu. Measurement Aniline In Sewage Based On Chloros Photometric Method. *Environmental Chemistry*, 1994, 13(06): 11-12.

Marine Science Bulletin

Marine Science Bulletin publishes papers on marine science and technology including physical oceanography, chemical oceanography, marine biology, marine geology, environmental oceanography, estuarine & coastal sciences, marine technology, digital ocean, coastal zone management, ocean engineering, marine economics, etc., and aims to promote international academic exchange.

Editor-in-Chief: Lin Shaohua（林绍花）
Deputy Editor-in-Chief: He Guangshun（何广顺） Yang Ying （杨　鹰）
Executive Editor: Lin Baofa（林宝法） He Xuewu （何学武） Zhang Deshan（张德山）
Zhang Xiaoxian（张潇娴） Wang Zhankun（王占坤）
Computer typist: Cheng Xiuchun （程秀春）

Marine Science Bulletin **(Vol . 7 No. 1 May 2005)**

Responsible Institution:
State Oceanic Administration of China
Edited and Published Semi-annually by:
National Marine Data and Information Service
Address: 93 Liuwei Road, Hedong District, Tianjin 300171, China
E-mail: msb@mail.nmdis.gov.cn

ISSN1000-9620
CN12-1271/N